Musical Instrument Modelling Using Digital Waveguides

submitted by

Marc-Laurent Aird

for the degree of Ph.D

of the

University of Bath

2002

COPYRIGHT

Attention is drawn to the fact that copyright of this thesis rests with its author. This copy of the thesis has been supplied on the condition that anyone who consults it is understood to recognise that its copyright rests with its author and that no quotation from the thesis and no information derived from it may be published without the prior written consent of the author.

This thesis may be made available for consultation within the University Library and may be photocopied or lent to other libraries for the purposes of consultation.

Signature of Author .....

Marc-Laurent Aird

Summary

The technique of Digital Waveguide Modelling for musical instruments and room acoustics modelling is now quite firmly established. In this thesis we provide an investigation in to the practical use and extension of the technique in musical instrument models, with an emphasis towards models of drums.

The standard waveguide technique is described and analysed mathematically for basic models in one, two and three dimensions. Results of simulations are provided and compared against expected theoretical output. Methods to improve the quality of the simulations by considering the boundary termination and correcting the numerical dispersion error are discussed.

A model for a drum is presented which utilises a technique to interface 2D and 3D mesh structures. An analysis of the model is provided which compares the output to phenomena found from measurements of real instruments.

Extensions to the simple waveguide are proposed which include the modelling of stiff media in both 1D and 2D. These models include bars, stiff strings, plates and stiff membranes and in each case model output is analysed in depth by comparing to expected theoretical output. We also discuss approaches to include material specific frequency dependent damping.

The main contributions of this thesis have been in the analysis of the waveguide technique in 3D, the method of correcting dispersion error, the analysis and extension of the 1D and 2D stiff models and the development and extension of the interfacing technique used in the drum model. The original focus of the work was for drum modelling, but the analogies and implications to other musical instruments, and indeed in the area of room acoustics, are quite clear.

Acknowledgments

As many people probably know, the path to a PhD is a pretty turbulent one and I've not been without my ups and downs. To get there you definitely need a lot of support and to thank everyone who's done something to help me would be impossible, so apologies to anyone I might miss out.

First of all I would like to thank my parents for their unconditional support throughout my education and all aspects of my life. It's not just the money you know. You've always got behind everything I've done and without your support I'd have fallen by the wayside many years ago. I suppose my mother thought that eventually I might actually get off my proverbial and get a job. I'd also like to thank my brother Andrew for distracting me with football talk so I wouldn't get too stressed sitting behind my computer all day. Next up I'd like to say big thank you to my girlfriend Katherine for putting up with me and for being my best friend. A big shout also goes to her family, Mervyn, Sue (best roast dinners ever) and (not so little) Matt.

On the work front, I'd like to thank my supervisor John ffitch for taking me on and for his encouragement. Thanks also go to Joel Laird for helping me understand a lot of things about my work, and to Lauri Savioja and Stefan Bilbao for the useful e-mail advice. I've shared an office/lab with a lot of people over the last 3 years, so thanks to you all for sharing my stresses, but in particular thanks to Matt Piggott (for listening), Sarah Mitchell (for coffees) and to Dave Power (for single-handedly teaching me C). Thanks to Mark Gittoes for setting up the Maths Post-grad 7-a-side team too. Lastly I'd like to add some thanks to Jf Williams and Bill Morton for their help with my corrections.

To get through a PhD you need a lot of things other than work to distract you from actually doing any work. For me I've spent a lot excellent times playing in the band (`www.banacek.org`). So for that I'd like to say a huge thank you Iain (Bass) and his missus Maria, Andrew (Guitar - hope you come home soon) and (again) Joel (Guitar). One day we'll make it big. There's also all the folk I've lived with through the years such as Marie, Jon (pikey), Natee, Jeremy, Alfio, Jon, Matt, Katia and Kenny (Mark). Cheers also to all the skiing bunch (Trev, Janet, Miff, Gordon etc.) for taking me away once a year and also to the 'wonderful' Claverton Academicals Football Club. Lastly, thanks to Louisa Tamplin and Andrew Holmes for still being my friends after all these years and being there for me when I needed to get away from Bath.

I'm sure there must be more people out there too. Suffice to say however, that I've had a wonderful time here in Bath and met a lot of people who I will always remember.

Contents

Summary i

Acknowledgments ii

Table Of Contents iv

List Of Figures viii

List Of Tables xi

1 Introduction 1

1.1 The Modelling Process 1
1.2 Breakdown of the Thesis 3
1.3 The Wave Equation 4
1.3.1 The Travelling Wave Solution 4
1.3.2 Harmonic Solutions 6
1.3.3 String Impedance 8
1.4 The Digital Waveguide String 8

2 2D Waveguide Meshes 11

2.1 Lossless Scattering Junctions 11
2.2 Scattering Junctions in the 1D Digital Waveguide 13
2.3 Simple Mesh Structures 14
2.4 Calculating and Comparing Dispersion Error 18
2.5 Building Membrane Models 21
2.5.1 Using Rimguides to Model the Circular Boundary 21
2.5.2 Membrane Simulations 24
2.6 Correcting Dispersion Error Using a Filtered Mesh 26
2.6.1 Calculating Dispersion in the Filtered Mesh 26
2.6.2 Simulation 28

2.7 Conclusion and Discussion 30

3 3D Waveguide Meshes 32

3.1 The Rectilinear 3D Mesh 32

3.2 The 3D Dodecahedral Mesh 34

3.3 Using 3D meshes to model Acoustic Spaces 38

3.3.1 Boundary Conditions 38

3.3.2 Sensitivity of Resonant Modes to Changes in Room Size 41

3.3.3 Simulation of a Rectangular Space 43

3.3.4 Simulation of a Cylindrical Space 46

3.4 Conclusion and Discussion 49

4 Building a Drum Model 51

4.1 Setting up the Simple Drum Model 51

4.1.1 Interfacing 2D and 3D Meshes at an Impedance Discontinuity . . 51

4.1.2 Computed Membrane Impedance 54

4.2 Simulation Results 55

4.2.1 Correctly Modelling the Cylindrical Air Cavity 55

4.2.2 Results from the Complete Drum model 57

4.2.3 Modelling the Air Load 59

4.3 Conclusion and Discussion 60

5 1D Models Including Material Properties 62

5.1 Interleaved Digital Waveguides 63

5.2 A Digital Waveguide Model for the Euler-Bernoulli Beam 66

5.2.1 Evaluating Dispersion in the Bar Model 71

5.2.2 Boundary Conditions 73

5.2.3 Simulation 75

5.3 A Waveguide Stiff String Model 76

5.3.1 A FDS for the Stiff String Equation 78

5.3.2 Equivalence of the Stiff String Model to the FDS 81

5.3.3 Simulation Results 82

5.4 Conclusion and Discussion 84

6 2D Models Including Material Parameters 85

6.1 Modelling Stiff Plates 85

6.1.1 Finite Difference Schemes for the Stiff Plate Equation 86

6.1.2 The 2D Waveguide Plate Model 88

6.1.3 Simulation Example 92
6.2 Stiff Membranes 94
6.2.1 FDS for the Stiff Membrane 94
6.2.2 Equivalent Waveguide Model 95
6.3 Conclusion and Discussion 96

7 Representing Internal Damping 98
7.1 The string on an elastic sub-base 98
7.2 The string on a viscous sub-base 101

8 Conclusions and Future Research 107
8.1 Suggestions for Future Research 107
8.1.1 Extensions to the Drum Model 107
8.1.2 Including other phenomena 108
8.2 Conclusions and Discussion 110
8.2.1 Thesis Summary 110
8.2.2 Contributions of the Author 112
8.2.3 Conclusions 114

A The Physics Of Musical Instruments 119
A.1 The Ideal Wave Equation in 1D, 2D and 3D 119
A.1.1 Derivation and solution of the 1D Wave Equation 119
A.1.2 Solving the 2D Wave Equation for a Circular Membrane 120
A.1.3 The Wave Equation in 3D 122
A.2 Bending Stiffness in Bars and Stiff Strings 126
A.2.1 Deriving the Euler-Bernoulli beam equation 126
A.2.2 Bars with Fixed, Free, and Simply Supported Ends 128
A.2.3 Stiff Strings 131
A.3 The String on a Viscoelastic Foundation 134
A.3.1 The String on an Elastic Foundation 134
A.3.2 The string on a Viscous Foundation 136
A.4 Vibrations in Plates and Stiff Membranes 137
A.4.1 Circular Plates 138
A.4.2 Rectangular Plates 140
A.4.3 Bending Stiffness in a Membrane 142

B Finite Difference Schemes 143
B.1 Deriving Finite Difference Approximations 143

B.2 Difference Schemes for the Wave Equation 145
B.3 Von Neumann Analysis 146
B.4 Interpolated Schemes 147
B.4.1 Interpolated Schemes in 2D 147
B.4.2 Interpolated Schemes in 3D 151

C Digital Signal Processing 155
C.1 Transforms 155
C.2 Digital Filters 156
C.2.1 Allpass Filters 157
C.2.2 Fractional Delay Approximation 158

D Additional Proofs 160
D.1 Equivalence Between Waveguide Stiff String Model and a FDS 160
D.2 Equivalence Between Waveguide Stiff Membrane Model and a FDS . . . 164

References 167

List of Figures

1-1 *Superposition of travelling waves.* 5
1-2 *Mode shapes in an ideal string.* 7
1-3 *The ideal lossless waveguide.* 9
1-4 *Simplified picture of the ideal waveguide including terminating reflection.* 10
1-5 *Harmonic Output of an Ideal String.* 10

2-1 *Waveguide Scattering Junction* 12
2-2 *The 1-D Digital Waveguide, T represents one unit of delay.* 14
2-3 *Mesh geometries for the square and triangular digital waveguide meshes.* 15
2-4 *Coordinate axes for the triangular mesh.* 17
2-5 *Dispersion error plot for the Square and Triangular meshes.* 20
2-6 *Max and Min Dispersion Error in Square and Triangular Meshes.* . . . 21
2-7 *Modelling a circular membrane with a triangular waveguide mesh and rimguides.* 22
2-8 *Frequency Plot For Membrane Without Fractional Length Rimguides.* . . 24
2-9 *Frequency Plot For Membrane With Fractional Length Rimguides.* . . . 25
2-10 *Errors in the positions of the resonant modes for membrane with and without rimguides.* 25
2-11 *(a) Angularly dependent dispersion error in the filtered mesh with* $a = -0.45$. *(b) Max and Min Dispersion Error in Filtered Mesh with* $a = -0.45$. 28
2-12 *Frequency Spectrum of Standard Mesh for* $f_s = 66150Hz$. 29
2-13 *Frequency Spectrum of Filtered Mesh for* $f_s = 66150Hz$. 30
2-14 *(a)-Errors for Standard Mesh with* $f_s = 66150Hz$. *(b)-Errors for Filtered Mesh with* $f_s = 66150Hz$. 30
2-15 *Frequency Spectrum of Filtered Mesh for* $f_s = 88200Hz$. 31

3-1 *Dispersion plots for the standard rectilinear mesh. (a)* $w_x = 0$, *(b)* $w_z = 0$, *(c)* $w_x = w_z$, *(d)* $w_x = w_y = w_z$, *(e)* $w_y = w_z = \frac{1}{\sqrt{3}} w_x$ 35

3-2 *Junction in the Dodecahedral Mesh* 36
3-3 *A Rhombic Dodecahedron* 36
3-4 *Dispersion plots for the dodecahedral/cuboctahedral mesh. (a)* $w_x = 0$, *(b)* $w_z = 0$, *(c)* $w_x = w_z$, *(d)* $w_x = w_y = w_z$, *(e)* $w_y = w_z = \frac{1}{\sqrt{3}} w_x$ . . . 39
3-5 *Boundary Conditions for Square Mesh* 41
3-6 *Frequency Spectrum For Square Mesh.* 45
3-7 *Frequency Spectra For Dodecahedral Mesh Simulations of Cubic Enclosures.* 46
3-8 *Boundary implementations at the circular boundary of a cylindrical enclosure using a square mesh.* 48

4-1 *Membrane Mesh Scattering Junction* 52
4-2 *Membrane Mesh with Underlying Air Mesh.* 53
4-3 *The Air to Skin Interface.* 53
4-4 *The Skin to Air Interface.* 54
4-5 *Membranes Struck at Centre and Off Centre.* 58
4-6 *(a) Drum model output measured from top skin. (b) Drum model output measured from Bottom skin.* 58

5-1 *Interleaved Waveguide.* 64
5-2 *Digital Waveguide Network for the Euler-Bernoulli Bar* 68
5-3 *Junction structure and input parameters* 69
5-4 *Comparison of Modelled and True Wave Speeds for the Bar Model.* . . . 72
5-5 *Relative Phase Plots for the Bar Model.* 73
5-6 *Boundary Conditions for clamped and free ends.* 75
5-7 *Evolution of transverse velocity waves along Euler-Bernoulli Bar.* 77
5-8 *Frequency Spectrum observed from bar model output.* 78
5-9 *Digital Waveguide Network for the Stiff String* 79
5-10 *Relative Phase Plots for the Stiff String Model.* 81

6-1 *Relative Phase Plots for Square and Triangular Mesh Stiff Plate Models* 89
6-2 *Square Mesh Waveguide Plate Model.* 90
6-3 *Coupling in waveguide plate model.* 92
6-4 *Relative Phase Plots for Square and Triangular Mesh Stiff Membrane Models* 96

7-1 *Frequency versus wavenumber for waveguide on a bed of springs.* 101
7-2 *Output from Viscous Waveguide with* $g = 5$. 104
7-3 *Wave Speed on Viscous Waveguide.* 104
7-4 *Waveguide model for Viscoelastic String.* 105

8-1 *The Voigt Unit.* 109
8-2 *The Maxwell Unit.* 110

A-1 *Segment of a string held under tension F* 120
A-2 *First 12 modes of the ideal circular membrane.* 121
A-3 *Forces acting on an ideal bar* 126
A-4 *Plot of Frequency against Wavenumber and some Dispersion Curves for String on an elastic foundation.* $a = 10^6$, $b = 10^5$, $c = 0$. 136
A-5 *A string on a Viscoelastic Foundation.* 137

B-1 *Deriving a first order difference.* 144
B-2 *Calculating Bilinear Interpolation Coefficients.* 149
B-3 *(a) Dispersion Plot for Interpolated Waveguide Mesh. (b) Max and Min Dispersions for Interpolated Waveguide Mesh* 150
B-4 *Scattering junction in the 3-d interpolated waveguide mesh.* 153
B-5 *Dispersion error for various cross sections through interpolated waveguide mesh. (a)* $w_x = 0$, *(b)* $w_x = w_z$, *(c)* $w_x = w_y = w_z$, *(d)* $w_y = w_z = \frac{1}{\sqrt{3}} w_x$. 154

C-1 *Magnitude Response and Phase Delay of 1st Order Lagrange Interpolator.* 159
C-2 *Phase Delay of 1st Order Thiran Allpass Filter.* 159

List of Tables

2.1 *Comparing measured and real mode frequencies for meshes with and without rimguides.* 24
2.2 *Comparing computing requirements between the standard and allpass filtered waveguide meshes.* 28
2.3 *Performance Comparison Between Standard and Filtered Meshes.* 29

3.1 *Coordinates of neighbouring mesh points for node at* $(0, 0, 0)$ 36
3.2 *Resonant Modes for different sized square enclosures.* 42
3.3 *Resonant Modes for different sized cylindrical enclosures.* 42
3.4 *Performance Evaluation for Square Mesh.* 43
3.5 *Performance Evaluation for Square Mesh Using Rimguides.* 44
3.6 *Performance Evaluation for Dodecaheral Mesh Simulation of Rectangular Enclosure.* 46
3.7 *Performance Evaluation for Cylinder Using a Square Mesh* 47
3.8 *Performance Evaluation for Cylinder Using a Square Mesh With Rimguides.* 48
3.9 *Performance Evaluation for Cylinder Using a Dodecahedral Mesh.* . . . 49

4.1 *Comparison Of Model Parameters in the Drum Model.* 52
4.2 *Comparison of measured and expected modes in drums air cavity.* 56
4.3 *Output from the Drum Model* 59
4.4 *Measured output from Real Drums* 60

5.1 *Comparing theoretical and modelled resonant modes for the bar model.* . 76
5.2 *Comparison of modelled and theoretical mode frequencies for a High E-string* 83
5.3 *Comparison of modelled and theoretical mode frequencies for a Low E-string* 84

6.1 *Comparing theoretical and modelled resonant modes (in* Hz*) for the plate model.* 93

7.1 *Comparing modelled and theoretical fundamental frequencies for a string on an elastic foundation.* 100
7.2 *Modelled modes for Viscous Waveguide with* $g = 5$. 105

Chapter 1

Introduction

1.1 The Modelling Process

Music has long since been established as an interdisciplinary area of research and practice in both the arts and science. There is a well established link between music theory and mathematics [23], and science has also been applied to the design and analysis of musical instruments [15].

Music is almost as old as the human race itself, and consequently many musical instruments have evolved over time to their current form. Considerations of why an instrument should be shaped the way it is, or sound the way it does, is a knowledge that has been passed down over many thousands of years from craftsmen to their apprentices. As art flourished through the renaissance period beginning in 15th century so did a return to science. Mathematical theories and descriptions of the physical world developed extensively. The techniques found could be used to describe physical phenomena and soon found their way into descriptions of musical instruments. Providing a mathematical model of parts of the motion within a musical instrument helps us understand the reasons why an instrument makes the sound it does, and furthermore we may consider how changes in shape or material affect the quality of the sound.

Sound is simply caused by varying pressure in the air. We hear sound because it propagates through the air in the form of waves, which our ear translates into electrical signals which are sent to the brain. Musical instruments generate sounds by causing vibrations which cause local changes in air pressure, sending out sound pressure waves. There are three stages to the generation of sound in musical instruments. First, we must excite the instrument. This is usually done by plucking or striking a string or membrane, or perhaps by blowing. The excitation causes the physical parts of the instrument to vibrate. The resulting changes in air pressure can be augmented and

enhanced by some resonant chamber, and controlled by changing the shape or size of the resonator or resonant chamber. Any complete physical model must represent each of these stages. This thesis will predominantly be concerned with representations of the vibrating parts, and coupling with resonant cavities.

To represent vibratory motion through the constituent parts of the instrument, we derive a set of equations called Partial Differential Equations (PDE). These equations may be solved in order to describe, say, the displacement, of the resonator with respect to position and time. However, changes in the shape of the resonator means we will often be required to re-solve the equations under a new set of *boundary conditions*, and furthermore in musical instruments there will typically be many resonators coupled together (often in different dimensions, such as the skins, air cavity and shell in a drum), and consequently finding a single constituent set of equations will be quite hard. Thus we consider using a numerical model for the instrument. The numerical model approximates the physical equations over a finite set of points arranged spatially in a *mesh*. Once the numerical method has been defined over this mesh, changes in the shape are quite easily implemented, without the need to re-solve the physical equation.

By constructing a physical model and its numerical equivalents we open up new possibilities in instrument design, synthesis, and analysis. For example we may theorise new or abstract shapes. We may build instruments using non-standard materials such as glass or ice say, which would be difficult or impossible in reality. Furthermore, using numerical mesh techniques we may envisage such expressive controls as time-varying shapes. In an analysis sense, we may isolate particular phenomena in an instrument by removing certain parts of the instrument in the model, something which is sometimes hard to do and imprecise with real instruments. It is often difficult to measure the behaviour of real instruments in a laboratory in order to isolate and analyse certain phenomena to investigate their contribution to the sound. A numerical model gives us a virtual world within which we may experiment freely and where we may bend the rules of the physical world to find out more about the physical systems.

When considering musical instrument models there is also a perceptual issue [31, 39]. The desired accuracy of any numerical model and the suitability of its underlying PDE must be set in the context of what a human being can actually hear. Humans hear sounds only at frequencies below $20000Hz$ and often frequencies in an even lower band are the most important in recognising the sound. This limit often dictates the choice of the mathematical equations and the numerical schemes used to model a particular instrument, when sometimes a simpler dynamical system or model can suffice for musical sound purposes.

There are many numerical techniques which could be used for musical instrument

modelling, Finite Difference Schemes (FDS) and Finite Element Methods (FEM), being two such cases. In this thesis we shall be investigating the Digital Waveguide modelling technique first introduced to represent ideal wave propagation in 1D, and later extended to mesh models in 2D and 3D [46, 52, 56]. We shall see in due course that the digital waveguide represents an alternative formulation of FDS, and some consideration as to its place within numerical modelling in terms of FDSs and FEMs will be given in the conclusions. We begin with a summary of the thesis.

1.2 Breakdown of the Thesis

This thesis attempts to provide descriptions, performance analyses and discussions on the use of digital waveguides in modelling musical instruments. The field ties together many disciplines across the fields of Acoustics, Signal Processing and Numerical Analysis. Consequently, care was taken when structuring the work so that many of the complicated derivations and analyses of different physical systems are included in the Appendix. The Appendix also contains background reading in Numerical Analysis and Digital Signal Processing.

The main structure of the thesis is designed to introduce the concept of a digital waveguide and to use it to model some simple systems. Consequently this brings up some problems and issues which we discuss later in the work. Chapter 1 introduces the concept of the digital waveguide by describing it as a tool for modelling an ideal string. This also introduces the basic procedures taken when modelling each of the systems considered. First we derive a mathematical equation for the motion of the system. Then we consider solutions to this equation, and follow that with a discrete numerical method which represents this solution. In chapter 2 we introduce the concept of the waveguide scattering junction and associated waveguide networks. We re-classify the 1D waveguide in these terms, and go on to discuss waveguides in 2D. In both these instances we introduce the important equivalence between waveguide networks and Finite Difference Schemes (FDS). We go on to show the modelling performance of the 2D waveguide mesh, and discuss approaches to improve this performance by using signal processing techniques.

Chapter 3 extends the theory further into 3D, discussing the performance of different mesh structures when applied to typical modelling problems in musical instrument synthesis and room acoustics. Then in chapter 4 we bring together the work of the first three chapters to build a model for a tom-tom drum. In order to complete the model we combine the models of chapters 2 and 3 and describe an interfacing technique used to connect the 2D meshes representing the drum skins to a 3D mesh representing

the interior air cavity. This interfacing method was developed by the author together with Joel Laird. By this point we have shown that the existing models can be used to form musical instrument models. However, the model is quite simplistic, for example we model only ideal wave propagation across the membrane, and the rest of the thesis deals with extending the waveguide technique to include other physical phenomena such as internal stiffness and damping.

In chapter 5 we discuss extending the 1D waveguide technique to include models for bars and stiff strings. This approach is extended into 2D in chapter 6 to deal with plates and membranes. In each of these cases we describe, analyse and implement the models, while leaving the physical derivation and analyses of the systems to Appendix A.

Finally in chapter 7 we include some introductory remarks on how to incorporate damping. We propose a method by which this could be performed and include initial results for the simplest cases. Chapter 8 serves to summarise and conclude the main results of the thesis and discuss some of the vast numbers of directions that the author feels work in this field could proceed.

1.3 The Wave Equation

The 1D wave equation describes the movement of transverse waves on an ideal string and is derived in Appendix A.1.1 as

$$\frac{\partial^2 u}{\partial t^2} = \frac{F}{\rho}\frac{\partial^2 u}{\partial x^2} = c^2 \frac{\partial^2 u}{\partial x^2}, \tag{1.1}$$

where $u(x,t)$ represents the transverse displacement of the string at time t and at position x, while F is the tension under which the string is held and ρ its linear mass density. To a large extent this equation, its solutions and its extensions form the basis of most of this thesis. In this section we shall discuss solutions to this equation, introducing some standard techniques and approaches that will be assumed throughout the work.

1.3.1 The Travelling Wave Solution

The classical solution to this equation was formulated by D'Alembert in 1747. This stated that the solution to the wave equation above is comprised of a superposition of two waves travelling in opposite directions so that

$$u(x,t) = f(ct - x) + g(ct + x),$$

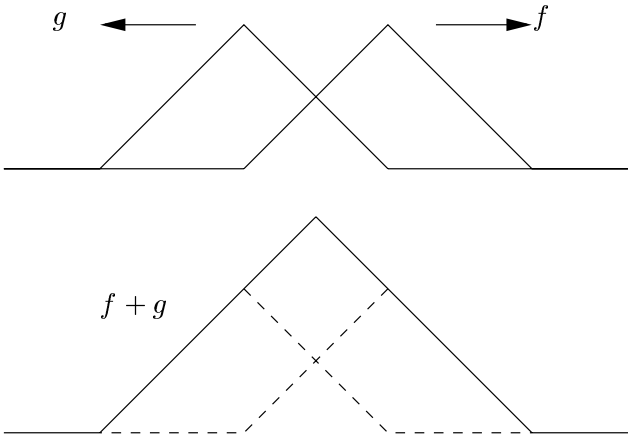

Figure 1-1: *Superposition of travelling waves.*

where $f(ct - x)$ represents a wave travelling to the right (in the positive x direction) with speed c, while $g(ct + x)$ represents a wave travelling to the left with the same speed c. Figure 1-1 describes the superposition of two waves travelling in opposite directions to give a single wave. For a string with a fixed end at say $x = 0$, we require the displacement to be $u(0, 0) = 0$. In this case the general travelling wave solution becomes

$$u = 0 = f(ct) + g(ct),$$

and hence

$$f(ct) = -g(ct),$$

from which we may conclude that a rigid termination incurs an inverting reflection in the travelling waves. This travelling wave interpretation of the solution to the wave equation will be the starting point for our discussions of digital waveguides.

The travelling wave description represents a general solution to the wave equation in terms of arbitrary functions f and g. We may also consider the existence of simple harmonic travelling waves of the form $u = Ae^{i(wt \pm kx)}$. Substitution in equation (1.1) yields the following relationship between *wavenumber* k, frequency w and speed c,

$$k = \frac{w}{c}.$$

This kind of relationship can tell us much about the behaviour in a given system. In this instance we will be able to affirm that waves of all frequencies will travel at the same speed on an ideal string. The wavenumber k is also sometimes called the *harmonic*

index.

1.3.2 Harmonic Solutions

To obtain a precise solution to equation (1.1) we apply the method of separation of variables. We write the solution as $u(x,t) = X(x)T(t)$ which gives

$$c^2 \frac{X''}{X} = \frac{\ddot{T}}{T},$$

where $X' = \frac{dX}{dx}$ and $\dot{T} = \frac{dT}{dt}$. Since each side of this equation depends on a single variable only, the expression must be constant, and we set this constant to be $-w^2$ so that

$$\begin{aligned} X'' + \frac{w^2}{c^2} X &= 0 \\ \ddot{T} + w^2 T &= 0. \end{aligned}$$

The second of these equations has solution $T(t) = A\sin(wt) + B\cos(wt)$. The first equation has solution $X(x) = C\sin(\frac{w}{c}x) + D\cos(\frac{w}{c}x)$. For a finite string of length L, held rigid, the boundary conditions assert that $y(0,t) = y(L,t) = 0$. Applying this gives $D = 0$ and

$$\sin(\frac{w}{c}L) = 0.$$

Thus we obtain the *natural frequencies* (or *eigenfrequencies*) of the system given by

$$w_n = \frac{n\pi c}{L},$$

where $n \in \mathbb{N}$. These represent discrete frequencies at which the string is capable of undergoing simple harmonic motion. We may also represent these frequencies in Hertz (Hz) by writing $f_n = w_n/2\pi$. This sequence of frequencies is referred to as a *harmonic* sequence since each frequency f_n is an integer multiple of the *fundamental* frequency $f_1 = c/2L$.

Now, for each n we have a vibrational pattern of the string given by

$$X_n(x) = C_n \sin(\frac{n\pi}{L}x)$$

and the functions X_n are called the *normal modes* of vibration (or *eigenfunctions*). Now combining the time and spatial dependencies for a given n gives solutions of the

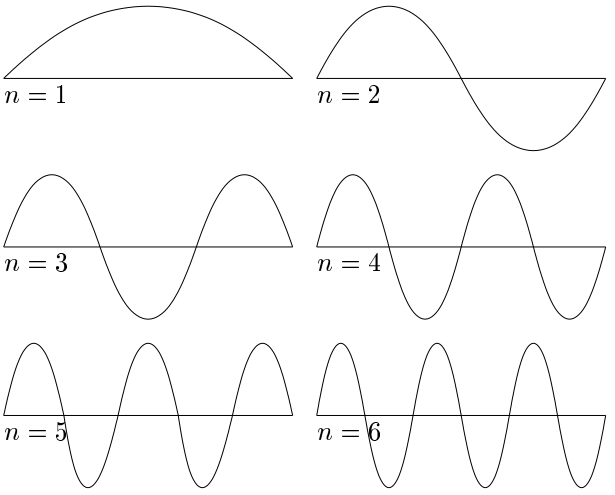

Figure 1-2: *Mode shapes in an ideal string.*

form

$$u_n(x,t) = [A_n \sin(w_n t) + B_n \cos(w_n t)] \sin(\frac{n\pi}{L}x),$$

and a general solution formed by superposing these

$$u(x,t) = \sum_{n=1}^{\infty} [A_n \sin(w_n t) + B_n \cos(w_n t)] \sin(\frac{n\pi}{L}x).$$

The concept of natural frequencies and normal modes of vibration is one which will be explored for many systems in this thesis, since it gives a theoretical prediction as to the behaviour of a system with which we may compare any model. Shown in Figure 1-2 are some mode shapes of an ideal string. The points of zero displacement are called the *nodes* of vibrations, while the maxima occur at *antinodes*. When a string is excited by plucking, the resultant motion will be a combination of several modes of vibration. For example, when plucking at the centre, the resultant vibration will consist of the fundamental, followed by each of the odd-numbered harmonics, while if the string were plucked at one fifths length, then every fifth harmonic will disappear. It is generally considered that the richest sounds are obtained when plucking around one fifths of the way along the string. When the string is plucked at the centre we lose too many harmonics, while plucking too close to the end tends to excite the higher harmonics more, giving a slightly 'twangy' sound. Thus we have seen how a mathematical description of the string has allowed us to re-affirm our practical knowledge.

1.3.3 String Impedance

The concept of wave impedance is important when defining the digital waveguide since it is a property which relates the velocity and force of a travelling wave. We derive the characteristic impedance for a string by separately considering the left and right going travelling waves. Writing the right-going wave as $f(x,t) = e^{i(wt-kx)}$ then the force $p(x,t)$ and velocity $v(x,t)$ may be computed as

$$\begin{aligned} p(x,t) &= -Ff'(x,t) = Fikf(x,t) \\ v(x,t) &= \dot{f}(x,t) = iwf(x,t), \end{aligned}$$

where F is string tension and $p = -Ff'$ from the derivation of the 1D wave equation. Then the impedance Z can be computed from the ratio of force and velocity as

$$Z = \frac{p(x,t)}{v(x,t)} = F\frac{k}{w} = \frac{F}{c} = \sqrt{F\rho}.$$

Similarly by writing the left-going wave as $g(x,t) = e^{i(wt+kx)}$ we have

$$\begin{aligned} p(x,t) &= -Fg'(x,t) = -Fikg(x,t) \\ v(x,t) &= \dot{g}(x,t) = iwg(x,t), \end{aligned}$$

giving

$$Z = \frac{p(x,t)}{v(x,t)} = -F\frac{k}{w} = -\sqrt{F\rho}.$$

Consequently waves travelling in opposite directions have impedances of opposite sign, and this characteristic impedance can also be calculated in terms of the density and wave speed of the medium as $R = \rho c$.

1.4 The Digital Waveguide String

The Digital Waveguide was first introduced in [46] and was derived by discretising the D'Alembert solution to the wave equation described previously. By sampling the travelling waves every T seconds, corresponding to a sample rate $f_s = 1/T$, our resultant spatial sampling interval will be the distance travelled in one time step. That is $\Delta = cT$ metres. Consequently, we may consider a discretised transverse displacement U such

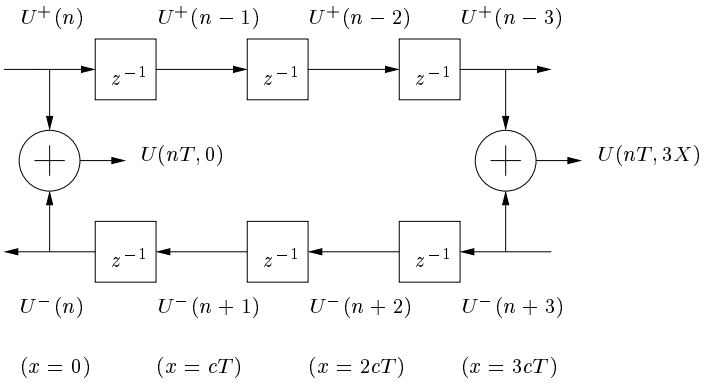

Figure 1-3: *The ideal lossless waveguide.*

that

$$\begin{aligned} U_m(n) = u(nT, m\Delta) &= f(nT - \frac{m\Delta}{c}) + g(nT + \frac{m\Delta}{c}) \\ &= f[(n-m)T] + g[(n+m)T] \\ &= U^+(n-m) + U^-(n+m), \end{aligned}$$

where $U^+(n) = f(nT)$ and $U^-(n) = g(nT)$ are the discretised travelling waves. We may think of $U^+(n-m)$ as the output from an m-sample delay line whose input is $U^+(n)$, and similarly $U^-(n-m)$ as the input to an m-sample delay line with output $U^-(n)$. A section of a lossless digital waveguide is shown in Figure 1-3. Note that the digital waveguide is exact at each discrete position, and the simulation will yield accurate solutions to the wave equation provided the initial travelling wave shapes are band-limited to less than half the sampling frequency (the Nyquist rate). Note that we shall be able to re-examine the 1D waveguide in the next chapter as a finite difference scheme, where we may discuss its precision using standard techniques from numerical analysis.

Rigid terminations may be implemented by simply taking the output from the ends of each delay line, inverting and placing at the corresponding input of the other line. Formally, referring to Figure 1-4 we would have,

$$\begin{aligned} U^+(n) &= -U^-(n) \\ U^-(n + \frac{N}{2}) &= -U^+(n + \frac{N}{2}), \end{aligned}$$

where $N = 2L/\Delta$ is the time in samples taken to complete one *string loop*. By describing the digital waveguide in terms of delay lines, we point towards the use of other digital signal processing applications such as digital filters. When representing musical

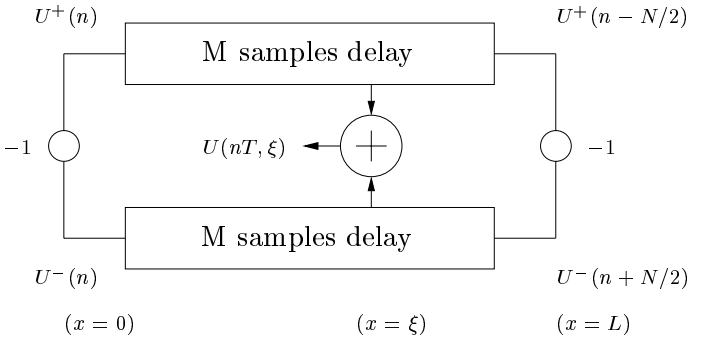

Figure 1-4: *Simplified picture of the ideal waveguide including terminating reflection.*

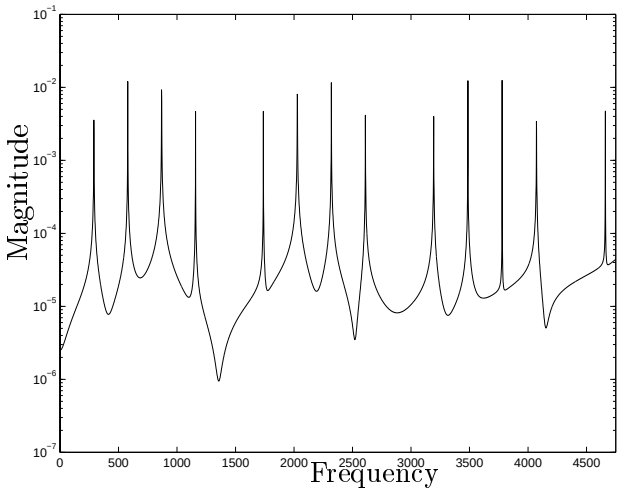

Figure 1-5: *Harmonic Output of an Ideal String.*

instruments using digital waveguides many additional phenomena can be synthesised by using filters. Such filters can be used to calibrate the model, to introduce frequency dependent effects observed in real instruments, to couple together other waveguide strings or to introduce interaction between a string and an exciter [27, 54]. The output from a 1D digital waveguide string is shown in Figure 1-5. Note the harmonic nature of the signal. Also, the string was hit a fifth of the way along and consequently every fifth harmonic is missing as expected.

Chapter 2

2D Waveguide Meshes

In this chapter we review many of the basic principles behind digital waveguide modelling by applying the technique to modelling 2D wave propagation.We describe the construction of waveguide meshes by arranging so-called *scattering junctions* in a particular geometry, and re-introduce the 1D waveguide in these terms. These ideas were first introduced in [52]. At this point we describe the important connection between digital waveguides and Finite Difference Schemes (FDS) for the underlying physical equations. By doing this we are able to examine discrepancies in the modelling process due to *dispersion error* which can be angularly dependent in the case of a waveguide mesh. We apply the mesh method to a model for a circular membrane and discuss approaches to modelling the boundary. Finally we discuss an approach to correcting dispersion error, and apply the method again to a model for a circular membrane.

2.1 Lossless Scattering Junctions

Consider the interconnection of N waveguides, representing N strings with respective impedances $Z_0, Z_1, \ldots, Z_N$ as shown in Figure 2-1. Now at the junction, all waveguides must have the same velocity, that is

$$v_1 = v_2 = ... = v_N = v_J, \tag{2.1}$$

where $v_1, v_2, \ldots, v_N$ represent the discrete vertical velocities of each waveguide at the junction and v_J, the total junction velocity. We also have the condition that all forces must balance at the junction so that

$$f_1 + f_2 + ... + f_N = 0, \tag{2.2}$$

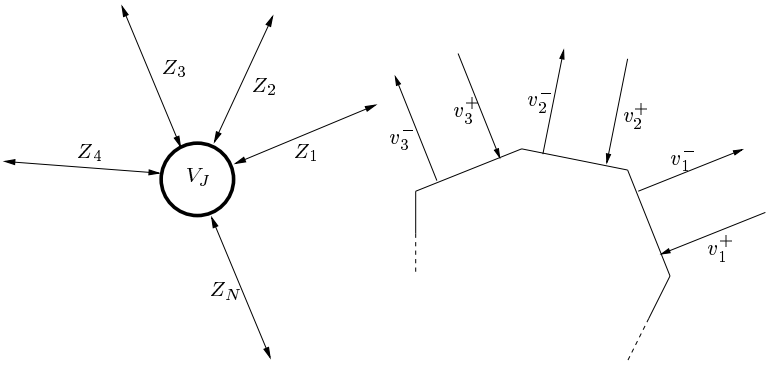

Figure 2-1: *Waveguide Scattering Junction*

with $f_1, f_2, ..., f_N$ representing the forces of each waveguide.

We resolve the force and velocity waves carried by each waveguide into left and right going waves which are related, from section 1.3.3, by

$$f_i = f_i^+ + f_i^-, \qquad v_i = v_i^+ + v_i^-, \tag{2.3}$$

$$f_i^+ = Z_i v_i^+, \qquad f_i^- = -Z_i v_i^-. \tag{2.4}$$

These relationships follow directly from the definition of impedance described in chapter 1.3.3. Hence from equations (2.1)-(2.4) we have

$$\begin{aligned} \sum_{i=1}^{N} f_i^+ + f_i^- &= 0 \\ \Rightarrow \sum_{i=1}^{N} Z_i(v_i^+ - v_i^-) &= 0 \\ \Rightarrow \sum_{i=1}^{N} Z_i v_i^+ &= \sum_{i=1}^{N} Z_i v_i^-, \end{aligned} \tag{2.5}$$

and consequently

$$v_1^+ + v_1^- = v_2^+ + v_2^- = \cdots = v_N^+ + v_N^- = V_J \tag{2.6}$$

$$\begin{aligned} \Rightarrow V_J \sum_{i=1}^{N} Z_i &= \sum_{i=1}^{N} Z_i v_i^+ + \sum_{i=1}^{N} Z_i v_i^- \\ \Rightarrow V_J \sum_{i=1}^{N} Z_i &= 2 \sum_{i=1}^{N} Z_i v_i^+ \\ \Rightarrow V_J &= 2 \frac{\sum_{i=1}^{N} Z_i v_i^+}{\sum_{i=1}^{N} Z_i}. \end{aligned} \tag{2.7}$$

Thus we have derived the standard *junction velocity equation* for a junction of N waveguides from the N travelling wave inputs $v_1^+, \ldots, v_N^+$. We may also calculate the reflected (or scattered) travelling wave velocity leaving the junction using equation (2.6) giving

$$v_i^- = v_J - v_i^+. \tag{2.8}$$

Furthermore, if all the strings have the same impedance Z, as will be the case in our mesh structures, then equation (2.7) is reduced to

$$v_J = \frac{2}{N}\sum_{i=1}^{N} v_i^+ \tag{2.9}$$

Finally we note an alternative junction velocity equation comprising a sum of outgoing velocity waves which is easily derived from the original equation.

$$v_J = 2\frac{\sum_{i=1}^{N} Z_i v_i^-}{\sum_{i=1}^{N} Z_i}. \tag{2.10}$$

We note also that there exists a dual form of this derivation for junction force. In this case we require that the force be the same at each junction, while the velocities sum to zero,

$$f_1 = f_2 = ... = f_N = f_J, \tag{2.11}$$

$$v_1 + v_2 + ... + v_N = 0. \tag{2.12}$$

A similar derivation to above yields a similar expression for the junction force

$$F_J = 2\frac{\sum_{i=1}^{N} Y_i f_i^+}{\sum_{i=1}^{N} Y_i}, \tag{2.13}$$

where $Y_i = \frac{1}{Z_i}$ is the admittance of each waveguide. This concept of a waveguide possessing two alternative wave variables will be explored in more depth in chapter 5.

2.2 Scattering Junctions in the 1D Digital Waveguide

We may now re-classify the 1D digital waveguide described in the previous chapter as a chain of two-port scattering junctions as shown in Figure 2-2. In this instance the velocity U_j at each junction j and at time step n may be written from equation (2.9)

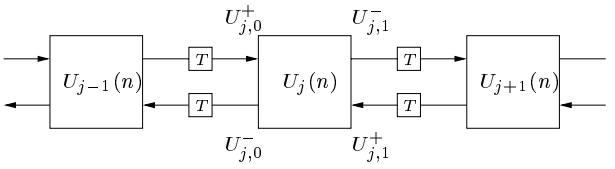

Figure 2-2: *The 1-D Digital Waveguide, T represents one unit of delay.*

as

$$U_j(n) = U^+_{j,0}(n) + U^+_{j,1}(n),$$

where $U^+_{j,0}$ represents the signal entering the left hand side of junction, while $U^+_{j,1}$ is the signal entering at the right. Now by writing the incoming travelling wave signals to junction j in terms of outgoing travelling waves at neighbouring junctions at the previous time step, and using equation (2.8), we may write

$$\begin{aligned} U_j(n) &= U^-_{j-1,1}(n-1) + U^-_{j+1,0}(n-1) \\ &= U_{j-1}(n-1) + U_{j+1}(n-1) - U^+_{j-1,1}(n-1) - U^+_{j+1,0}(n-1) \\ &= U_{j-1}(n-1) + U_{j+1}(n-1) - U^-_{j,0}(n-2) - U^-_{j,1}(n-2) \\ &= U_{j-1}(n-1) + U_{j+1}(n-1) - U_j(n-2). \end{aligned}$$

Subtracting $2U_j(n-1)$ from either side of this equation gives

$$U_j(n) - 2U_j(n-1) + U_j(n-2) = U_{j-1}(n-1) - 2U_j(n-1) + U_{j+1}(n-1),$$

which we recognise as a centered finite difference scheme (see Appendix B.2) for the 1D wave equation (1.1) with $\lambda = T/\Delta = 1/c$. And we note that this relationship between the time and spatial step sizes is identical to that formed in the derivation of the 1D waveguide in the previous chapter. This equivalence of the waveguide to a finite difference scheme will be essential in subsequent chapters where we wish to analyse the accuracy of our waveguide models.

2.3 Simple Mesh Structures

Digital waveguide meshes are constructed by connecting unit length waveguides via scattering junctions in a particular geometry. We introduce two such geometries as shown in Figure 2-3. The square mesh requires 4-port junctions, which can be implemented quite cheaply using only four additions and a binary shift for the division. The triangular mesh however, requires 6-port scattering junctions and is not so cheaply

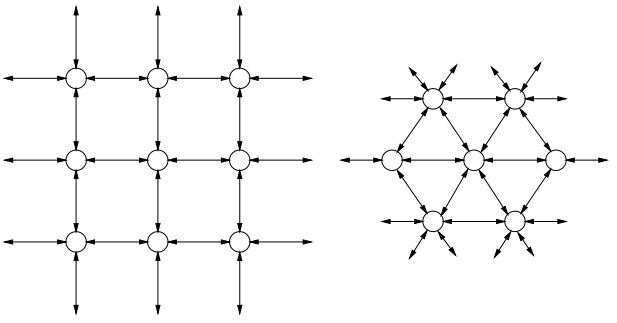

Figure 2-3: *Mesh geometries for the square and triangular digital waveguide meshes.*

implemented, although we shall see later that it is the more desirable mesh structure. Both structures can be shown to be equivalent to a FDS for the 2D wave equation defined in Appendix A.1.2 as

$$\frac{\partial^2 u}{\partial t^2}(t,x,y) = c^2 \left(\frac{\partial^2 u}{\partial x^2}(t,x,y) + \frac{\partial^2 u}{\partial y^2}(t,x,y) \right), \tag{2.14}$$

where $u(t,x,y)$ represents vertical displacement, $c = \sqrt{F/\rho}$, F is tension per unit length of the membrane and ρ its superficial density. By drawing this equivalence we are able to apply stability and performance tests from numerical analysis to the waveguide meshes. In fact, it is possible to derive digital waveguide meshes and networks which represent a large class of PDEs possibly providing good physical descriptions of complicated systems, but this is outwith the scope of this thesis and the curious reader is pointed towards [8]. Certainly with the simple waveguide mesh, however, we have a physically intuitive form of the wave equation, which is perhaps much more readily understandable to the lay-man than the underlying FDS.

To prove the equivalence of the two methods we begin by taking the Z-transform (Appendix C.1) of the two forms of the junction velocity equation (2.9) and (2.10), giving

$$V_J(z) = \frac{2}{N} \sum_{i=1}^{N} V_i^+(z) \tag{2.15}$$

$$V_J(z) = \frac{2}{N} \sum_{i=1}^{N} V_i^-(z), \tag{2.16}$$

where $V_J(z)$ represents the Z-transform of the discretised transverse junction velocity $v_J(n)$. The notation used in the following derivation has been chosen in order to develop a general equivalent difference scheme which can then be applied to meshes of

either a square or triangular geometry. We use the Z-transform to keep the waveguide mesh within the signal processing framework, since we investigate a filtered mesh later. However, it should be clear that the following calculations are almost identical in the temporal domain. Furthermore, the notation used here will in fact be replaced by standard finite difference scheme notation in subsequent chapters.

Now, by letting $V_{J,i}(z)$ be the velocity signal of the ith junction adjacent to junction J we may rewrite equation (2.16) in a form involving wave signals incoming to each adjacent junction from junction J at the next time step,

$$V_J(z) = \frac{2}{N}\sum_{i=1}^{N} zV_{J,i}^{+}(z), \tag{2.17}$$

where $V_{J,i}^{+}(z)$ represents the incoming wave signal to the ith adjacent junction coming from junction J, and the extra z represents the forward time step. Similarly we may rewrite equation (2.15) again involving the signals at the adjacent junctions, but this time at the previous time step, and where $v_{J,i}^{-}(z)$ represents the outgoing wave signal from the ith adjacent junction in the direction of junction J,

$$\begin{aligned} V_J(z) &= \frac{2}{N}\sum_{i=1}^{N} z^{-1}V_{J,i}^{-}(z) \\ &= \frac{2}{N}\sum_{i=1}^{N} z^{-1}\left[V_{J,i}(z) - V_{J,i}^{+}(z)\right], \end{aligned} \tag{2.18}$$

where the coefficient z^{-1} represents a reverse time step, as described in Appendix C.1, and $V_{J,i}(z)$ is the velocity of the ith adjacent junction. Now multiplying (2.17) by z^{-2} and adding to equation (2.18) yields

$$(1+z^{-2})V_J(z) = \frac{2}{N}\sum_{i=1}^{N} z^{-1}V_{J,i}(z),$$

and then multiplying through by z, followed by the inverse Z-transform gives us the result

$$v_J(n+1) + v_J(n-1) = \frac{2}{N}\sum_{i=1}^{N} v_{J,i}(n).$$

Now, subtracting $2v_J(n)$ from both sides we obtain the following difference equation

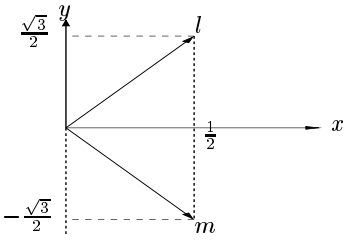

Figure 2-4: *Coordinate axes for the triangular mesh.*

consisting of a second order time difference on the left hand side,

$$v_J(n+1) - 2v_J(n) + v_J(n-1) = \frac{2}{N}\sum_{i=1}^{N}\left[v_{J,i}(n) - v_J(n)\right]. \tag{2.19}$$

This difference equation will take different forms depending on the mesh geometry chosen. For a *square* mesh, where $N = 4$ and junction J has coordinates l, m equation (2.19) becomes

$$\begin{aligned} v_{l,m}(n+1) - 2v_{l,m}(n) + v_{l,m}(n-1) &= \frac{1}{2}\left[v_{l+1,m}(n) - 2v_{l,m}(n) + v_{l-1,m}(n)\right] \\ &+ \frac{1}{2}\left[v_{l,m+1}(n) - 2v_{l,m}(n) + v_{l,m-1}(n)\right], \end{aligned}$$

which is clearly a centered finite difference scheme approximation to the the 2D wave equation (2.14), as given in Appendix B.2, with simulation parameters related by $\lambda c = \frac{Tc}{\Delta} = \frac{1}{\sqrt{2}}$. The stability and losslessness of the waveguide mesh was inferred by the passive nature of the waveguide junctions, but it may now be compared to stability of the FDS, which will be discussed in the subsequent section.

To evaluate the equivalence of the *triangular* waveguide mesh with a FDS, we must reset the 2D wave equation in the new coordinate system as shown in Figure 2-4. The new coordinate system has two new axes in the directions l and m. Partial derivatives in these new directions are calculated from

$$\begin{aligned} \frac{\partial w}{\partial l} &= \frac{1}{2}\frac{\partial w}{\partial x} + \frac{\sqrt{3}}{2}\frac{\partial w}{\partial y} \\ \frac{\partial w}{\partial m} &= \frac{1}{2}\frac{\partial w}{\partial x} - \frac{\sqrt{3}}{2}\frac{\partial w}{\partial y}. \end{aligned}$$

By summing and subtracting these terms we can derive expressions for the partial

derivatives in the x and y directions in terms of partial derivatives

$$\begin{aligned}\frac{\partial w}{\partial x} &= \frac{\partial w}{\partial l} + \frac{\partial w}{\partial m} \\ \frac{\partial w}{\partial y} &= \frac{1}{\sqrt{3}}\left(\frac{\partial w}{\partial l} + \frac{\partial w}{\partial m}\right).\end{aligned}$$

By applying each of these partial derivatives twice we obtain

$$\begin{aligned}\frac{\partial^2 w}{\partial x^2} &= \frac{\partial^2 w}{\partial l^2} + 2\frac{\partial^2 w}{\partial l \partial m} + \frac{\partial^2 w}{\partial m^2} \\ \frac{\partial^2 w}{\partial y^2} &= \frac{1}{3}\left(\frac{\partial^2 w}{\partial l^2} - 2\frac{\partial^2 w}{\partial l \partial m} + \frac{\partial^2 w}{\partial m^2}\right).\end{aligned}$$

Hence the 2D wave equation may be reformulated for these new triangular coordinates as

$$\frac{\partial^2 w}{\partial t^2} = c^2 \frac{2}{3}\left(\frac{\partial^2 w}{\partial l^2} + \frac{\partial^2 w}{\partial m^2} + \frac{\partial^2 w}{\partial x^2}\right). \tag{2.20}$$

Returning to the difference equation (2.19), using a triangular mesh results in the following FDS

$$\begin{aligned}v_{l,m}(n+1) - 2v_{l,m}(n) + v_{l,m}(n-1) &= \frac{1}{3}\left[v_{l+\frac{1}{2},m+\frac{\sqrt{3}}{2}}(n) - 2v_{l,m}(n) + v_{l-\frac{1}{2},m-\frac{\sqrt{3}}{2}}(n)\right] \\ &+ \frac{1}{3}\left[v_{l-\frac{1}{2},m+\frac{\sqrt{3}}{2}}(n) - 2v_{l,m}(n) + v_{l+\frac{1}{2},m-\frac{\sqrt{3}}{2}}(n)\right] \\ &+ \frac{1}{3}\left[v_{l+1,m}(n) - 2v_{l,m}(n) + v_{l-1,m}(n)\right].\end{aligned}$$

Again this is clearly a stable finite difference scheme approximation to the 2D wave equation (2.20) in the new coordinate system with again $\lambda c = \frac{Tc}{\Delta} = \frac{1}{\sqrt{2}}$.

2.4 Calculating and Comparing Dispersion Error

By drawing an equivalence between the waveguide mesh and FDS we are able to consider methods from numerical analysis in order to help determine the accuracy of the two mesh structures. Von Neumann analysis is an easy way to determine stability and wave propagation characteristics by evaluating the *spectral amplification factor*. We leave the complete theory of this form of analysis to Appendix B.3 and include only a brief summary here. The spectral amplification factor tells us how a scheme behaves in the frequency domain for each time step in the simulation. The amplification factor is a complex function and tells us the magnitude and phase response of the scheme for

each time advance. This method is equally applicable in one, two or three dimensions. We shall see its use in one dimension later on, but now we consider applying this type of analysis to the square and triangular waveguide meshes.

Following the notation of the previous sections, we take the Fourier transform of equation (2.19) to obtain the following quadratic equation for the spectral amplification factor $G(\mathbf{w})$, where $\mathbf{w}$ is the two dimensional angular frequency vector $\mathbf{w} = (w_x, w_y)^t$,

$$1 + bG + G^2 = 0,$$

where

$$b = -\frac{2}{N}\sum_{i=1}^{N} e^{iP^t_{j,i}(\mathbf{w})}. \tag{2.21}$$

In the above expression for b, the function P describes the linear phase shift experienced by the Fourier transform of the velocity when moved to each of the neighbouring grid positions in the FDS. For example, the point $(l+1, m)$ induces the phase term $P^t_{l+1,m}(\mathbf{w}) = w_x$ while the point $(l, m-1)$ gives $P^t_{l,m-1}(\mathbf{w}) = -w_y$. Hence for the square mesh, the quantity b becomes

$$\begin{aligned} b &= -\frac{1}{2}\left(e^{iw_x} + e^{-iw_x} + e^{iw_y} + e^{-iw_x}\right) \\ &= -\cos(w_x) - \cos(w_y), \end{aligned} \tag{2.22}$$

while for the triangular mesh

$$\begin{aligned} b &= -\frac{1}{3}\left[e^{i\frac{1}{2}(w_x+\sqrt{3}w_y)} + e^{-i\frac{1}{2}(w_x+\sqrt{3}w_y)} + e^{i\frac{1}{2}(w_x-\sqrt{3}w_y)} + e^{-i\frac{1}{2}(w_x-\sqrt{3}w_y)} + e^{iw_x} + e^{-iw_x}\right] \\ &= -\frac{2}{3}\left[\cos(w_x) + \cos\frac{1}{2}(w_x+\sqrt{3}w_y) + \cos\frac{1}{2}(w_x-\sqrt{3}w_y)\right]. \end{aligned} \tag{2.23}$$

Noting that in both cases above $b^2 - 4 < 0$ for all values of w, then the quadratic in G has complex roots given by

$$G(\mathbf{w}) = \frac{-b}{2} \pm i\frac{\sqrt{4-b^2}}{2}.$$

We observe immediately that the spectral amplification factor has unit magnitude, a characteristic of the losslessness and passivity of the scattering junctions from which

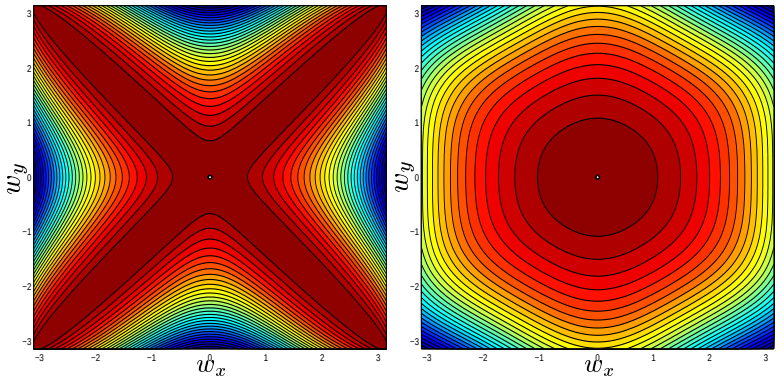

Figure 2-5: *Dispersion error plot for the Square and Triangular meshes.*

the meshes are formed. By calculating the phase of the spectral amplification factor

$$\theta(\mathbf{w}) = \tan^{-1}\left(\frac{\sqrt{4-b^2}}{-b}\right),$$

we may calculate the angular frequency dependent speed of wave propagation of a two dimensional plane wave over the mesh, in spatial samples per time step as

$$K(\mathbf{w}) = \frac{\theta(\mathbf{w})}{|\mathbf{w}|}.$$

We may now compare and discuss the dispersion characteristics of both the square and triangular meshes. Ideally all waves on an membrane travel at the same speed regardless of their angular frequency, that speed being $c = \sqrt{\frac{F}{\rho}}$. The left-hand contour plot of Figure 2-5 shows the dispersion of the square mesh. Here and throughout the thesis we consider dispersion for frequency $w = \frac{2\pi f}{f_s}$, where f_s is the sample rate and f is the frequency in Hz. We may conclude that waves will travel perfectly along the diagonal, but that in the axial direction there is a *dispersion error*. That is, waves travel slower with increasing frequency. This angular dependence on the propagation is undesirable. By using a triangular mesh we may eliminate the direction dependence of the dispersion error as shown by the right-hand contour plot in Figure 2-5. Furthermore Figure 2-6 shows cross-sections of the dispersion error plots showing maximum and minimum dispersions, and clearly there is great disparity in the dispersion error of the square mesh. We shall see that the shape of the dispersion error corresponds with a contraction of the resonant modes in a simulation of an ideal membrane later, with the mis-tuning of the resonances increasing with increasing frequency. In fact, we shall see in a later section that direction independent dispersion error is a desirable property of a mesh,

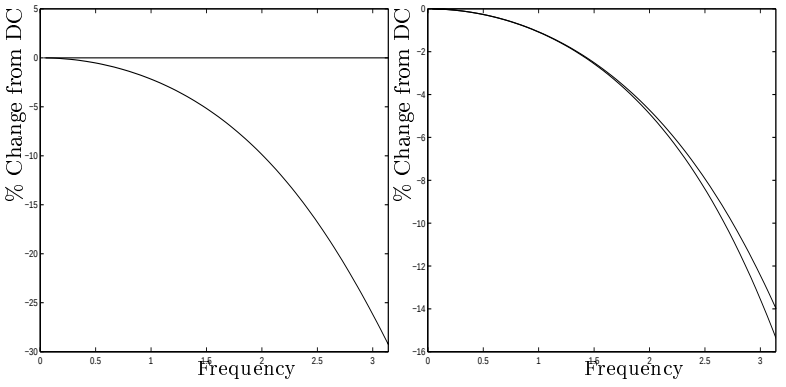

Figure 2-6: *Max and Min Dispersion Error in Square and Triangular Meshes.*

as it makes it easier to develop methods with which to correct the error. Furthermore it has been observed in [19] using signal theory that the triangular mesh offers a larger bandwidth than the square mesh.

Another mesh which offers near direction independence of the dispersion error is the interpolated scheme initially formulated in [42]. We include its derivation and some comments in Appendix B.4.1.

2.5 Building Membrane Models

We consider building a model of a circular membrane using a triangular digital waveguide mesh. The model shows a level of accuracy where errors are consistent with the dispersion error. We note that the triangular mesh does not model the circular boundary and consider the inclusion of so-called *rimguides*, first introduced by [25], as a method which more accurately models the circular boundary. Membrane models have also been considered in [16] where a simple 'staircase' boundary was implemented and we show that the method of rimguides improves this more simple approximation.

2.5.1 Using Rimguides to Model the Circular Boundary

To determine the size of our triangular digital waveguide mesh we will need to satisfy the following rule; that the time taken for a wave to traverse the diameter of the true membrane must match the time taken over the mesh. This will yield an ideal mesh diameter size, within which we will attempt to fit our mesh. In order to model the reflection best at the boundary of the membrane, we will assume that the membrane edge is fixed (as is the case with a drum skin). Then from the outermost mesh points (those closest to the boundary) we shall attach radial waveguides which will carry the

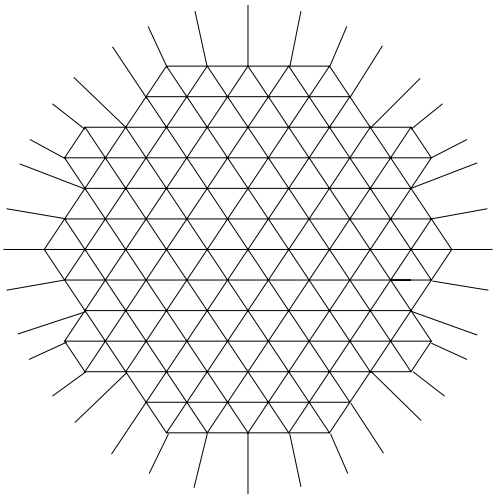

Figure 2-7: *Modelling a circular membrane with a triangular waveguide mesh and rimguides.*

signal to the boundary and back, together with a sign inversion to model the inverting reflection incurred at the fixed boundary. These self-loops have been termed *rimguides*. Of course due to the irregular nature of the boundary of the triangular mesh, these rimguides will not in general be an integer number of samples long, so we will consider implementing them using fractional delay filters. Using an allpass filter (Appendix C.2) to model the fractional delay imposes an ideal delay between 1.5 and 2.5 units. Thus we construct the mesh within an ideal mesh diameter d_b which is 1.5 units of delay below the true diameter. Recall that the rimguide produces half its delay out to the boundary and half its delay back to the mesh. An illustration of a triangular mesh with rimguides attached is shown in Figure 2-7.

Now the allpass filter models the required delay well for low frequencies, and for low frequencies we will assume that all waves travel across the mesh at the nominal wave speed, which is the DC wave speed $K(0) = \frac{1}{\sqrt{2}}$. Thus the time taken to traverse the mesh will be

$$t = \frac{1}{f_s}\left(\frac{d_b}{K(0)} + 1.5\right),$$

where d_b is the (as yet uncalculated) mesh diameter in spatial samples, and f_s is the sample rate. Note how we have included the minimum delay afforded by the rimguides.

Now given a membrane of radius r metres, and a wave speed c from equation (2.14), the time in seconds to traverse the membrane is calculated as $t = \frac{2r}{c}$. Setting the two

times to be equal gives

$$\begin{aligned} \frac{2r}{c} &= \frac{1}{f_s}\left(\frac{d_b}{K(0)} + 1.5\right) \\ \Rightarrow d_b &= K(0)\left(\frac{2rf_s}{c} - 1.5\right). \end{aligned}$$

Alternatively, if the size of a spatial sample within the mesh is $\Delta = \frac{\sqrt{2}c}{f_s} = \frac{1}{K(0)}\frac{c}{f_s}$ and the distance in waveguides travelled across the mesh in 1.5 time steps is $1.5K(0)$, then this boundary diameter can be expressed directly as

$$\begin{aligned} d_b &= \frac{2r}{\Delta} - 1.5K(0) \\ &= K(0)\left(\frac{2rf_s}{c} - 1.5\right). \end{aligned}$$

The mesh is then constructed to fit within this boundary. Now nodes closest to the boundary will have a diameter $d_m \leq d_b$. The total delay which the rimguide must implement will be

$$\tau_m = \frac{2rf_s}{c} - \frac{d_m}{K(0)},$$

and we note that this delay will necessarily be greater than 1.5.

An allpass filter will produce a delay for low frequencies which is very close to $D = 1 + \frac{1-a}{1+a}$, thus we will require to have

$$\begin{aligned} \left(1 + \frac{1-a}{1+a}\right) &= \tau_m \\ \Rightarrow \frac{1}{1+a} &= \frac{\tau_m}{2} \\ \Rightarrow a &= \frac{2-\tau_m}{\tau_m}. \end{aligned}$$

By ensuring that the delay be in the range $\tau_m \in [1.5, 2.5]$ the filter coefficient will be bounded so that $a \in [-\frac{2}{5}, \frac{1}{3}]$. Note also that it may be possible that the required delay be greater than $\tau_m = 2.5$ units of delay, and that in this case we implement a pure integer delay plus a fractional part within the correct bounds. That is we consider the delay as $\tau_m = N + d$, where N is an integer, and $d \in [1.5, 2.5]$.

Finally we note that a given boundary node, to which the rimguide will be attached will be less than a six port junction. To avoid an impedance discontinuity, and hence maintain junction passivity, the rimguide takes the impedance of the missing waveg-

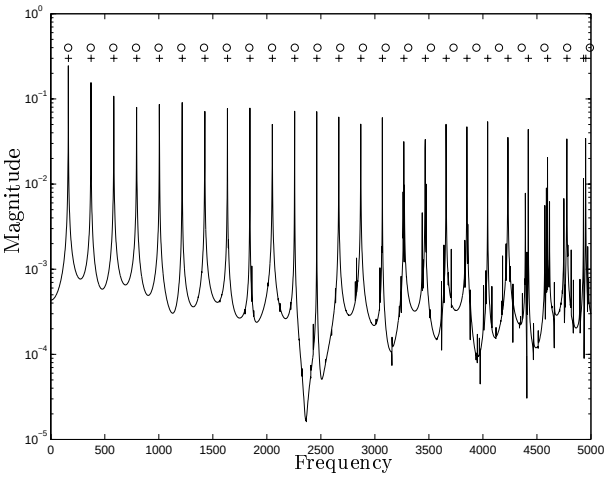

Figure 2-8: *Frequency Plot For Membrane Without Fractional Length Rimguides.*

Mode	True Frequency	Without Rimguide	With Rimguide
$f_{0,1}$	160.8	163	161
$f_{0,2}$	369.1	373	369
$f_{0,3}$	578.7	584	578
$f_{0,4}$	788.5	796	786
$f_{0,5}$	998.4	1006	995

Table 2.1: *Comparing measured and real mode frequencies for meshes with and without rimguides.*

uides. So for an M port junction, where $M < 6$, the rimguide will have $6 - M$ times the impedance of the other waveguides. We show later in the 3D case that this approach is justified when we consider the equivalent FDS at the boundary.

2.5.2 Membrane Simulations

We consider using a triangular waveguide mesh to model an ideal membrane of radius $r = 20cm$, with density $\rho = 0.262kg/m^2$ and held at a uniform tension of $F = 1850N/m$. By setting the sample rate to $f_s = 22050Hz$ we have a mesh boundary diameter $d_b = 73.5124$ waveguides, and we consider striking the membrane at its centre with an impulse so as to excite only the central modes of vibration. These values are quite reasonable simulation values [15, 30]. Shown in Figure 2-8 is the frequency spectrum for the mesh simulation with unit length rimguides. This gives a so-called 'staircase' boundary approximation implementing inverting reflections. Each measured resonant mode is represented by '+', while expected modal positions are marked by 'o'. We observe reasonable accuracy and an error which increases with frequency. Note

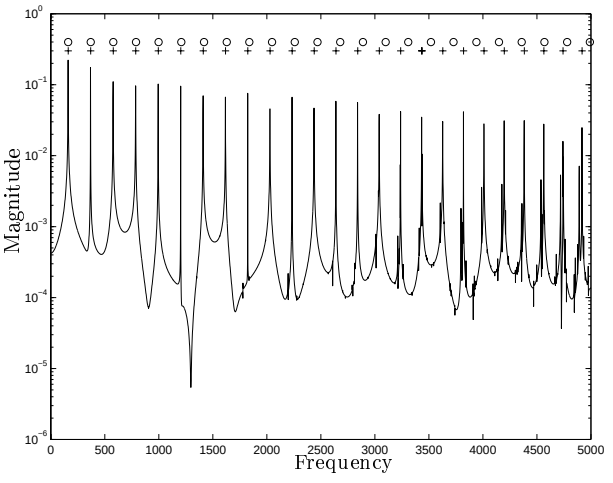

Figure 2-9: *Frequency Plot For Membrane With Fractional Length Rimguides.*

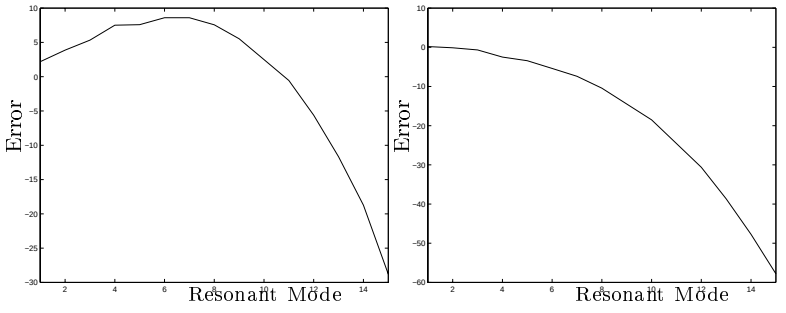

Figure 2-10: *Errors in the positions of the resonant modes for membrane with and without rimguides.*

however, that over the first few modes the model produces frequencies which are slightly higher than the theoretical modes, but that further up the scale frequencies are systematically lower than the desired resonances. A plot of the error over the first 15 modes is shown in the left hand plot of Figure 2-10. We now consider an implementation of the mesh together with fractional length rimguides whose frequency spectrum is shown in Figure 2-9. Table 2.1 shows that with the rimguides the model has the correct fundamental frequency, and that the first 5 modal frequencies are more accurate. In the right hand plot of Figure 2-10 we see that the error incurred in the mesh with rimguides is entirely consistent with an error caused by dispersion, while without the rimguides, extra inaccuracies are introduced due to the irregular boundary. In fact, with the fractional length rimguides in place, the *only* error is due to dispersion. We conclude that with a process to reduce the dispersion error, then together with the use of fractional length rimguides we would be able to model ideal wave propagation in

a membrane quite accurately using a triangular waveguide mesh. We now discuss a method by which we may reduce dispersion error in the triangular waveguide mesh.

2.6 Correcting Dispersion Error Using a Filtered Mesh

In this section we review an approach to correct the dispersion error. The method is an on-line process, where allpass filters are used in cascade with the units of delay between the nodes on the mesh [17]. These allpasses can be used to warp the frequencies during the course of propagation through the mesh, essentially speeding up the higher frequencies. This is due to the nature of the phase response of the allpass filter (see Appendix C.2.1). Thus we consider straightening the dispersion error observed in Figure 2-6.

2.6.1 Calculating Dispersion in the Filtered Mesh

Let us begin with a mathematical analysis of the new warped mesh. Warping is achieved by replacing each unit of delay in the waveguide mesh with a filter comprising a single unit of delay together with a first order allpass filter, so that the transfer function is

$$H(z) = \frac{z^{-1}(a + z^{-1})}{1 + az^{-1}},$$

where a is the allpass filter coefficient. It should be pointed out at this stage that this filter will implement a DC delay $D = 1 + \frac{1-a}{1+a}$. Thus it is clear that the sampling resolution for the filtered mesh will be required to be much higher than with the standard mesh. We recast the junction velocity equations (2.17) and (2.18) to give the following expressions

$$\begin{aligned} V_j(z) &= \frac{2}{N}\sum_{i=1}^{N}\frac{1}{H(z)}V_{j,i}^{+}(z) \\ V_j(z) &= \frac{2}{N}\sum_{i=1}^{N}H(z)\left[V_{j,i}(z) - V_{j,i}^{+}(z)\right]. \end{aligned}$$

Consequently we have

$$\left(\frac{1}{H(z)} + H(z)\right)V_j(z) = \frac{2}{N}\sum_{i=1}^{N}V_{j,i}(z).$$

Now by computing $\frac{1}{H(z)} + H(z)$ and by writing $b = -\frac{2}{N}\sum_{i=1}^{N} e^{iP_{j,i}^{t}(\mathbf{w})}$ as before, we may derive the following quartic expression for the spectral amplification factor,

$$1 + a(2+b)G + [a^2(2+b) + b]G^2 + a(2+b)G^3 + G^4 = 0, \tag{2.24}$$

where we have the same expression for b as with the unfiltered triangular mesh (2.23). Now we solve this quartic expression to give the spectral amplification factor as

$$G(\mathbf{w}) = \frac{-A}{2} \pm i\frac{\sqrt{4 - A^2}}{2},$$

where

$$A = \frac{a(2+b) - \sqrt{a^2(b^2-4) - 4(b-2)}}{2}.$$

We note the existence of two other solutions to the quartic expression (2.24) which contribute parasitic modes [47] which have no bearing on the output of the simulation. Once again to calculate the frequency and angularly dependent wave speed of the mesh we must consider the normalised phase of the spectral amplification factor. Shown in Figure 2-11 is a contour plot of the dispersion observed for an allpass filtered mesh with allpass coefficient set to $a = -0.45$. It clearly shows a broad flat area around the origin corresponding to a near flat dispersion. Looking in more detail, we may consider cross-sections of the dispersion plot also shown in Figure 2-11 and we compare to the cross sectional plot for the unfiltered mesh in Figure 2-6. From this we may deduce that over a wide range of frequencies about DC, waves on the filtered mesh travel at practically the same speed. This would appear promising in our quest to model an ideal membrane by reducing the dispersion error inherent in the original mesh formulation, but it should be noted that there are some trade-offs. Firstly, we note that the DC wave speed in the filtered mesh is considerably lower than that of the original mesh since there is a larger delay between nodes. For the filtered mesh we have $K(0) \approx 0.195$, while in the original mesh we had $K(0) = \frac{1}{\sqrt{2}} \approx 0.707107$. Consequently due to the slower average wave speed, we would require a much larger sampling resolution (around 3 and a half times as large) for simulations using the filtered mesh. Secondly, by observing the greyscale plot in Figure 2-11 a little more closely, we observe a slightly hexagonal nature, meaning that the dispersion is now not quite so angularly independent. Figure 2-11 shows the extremes of the dispersion error in the filtered case, showing quite clearly a larger angular dependence in the filtered mesh.

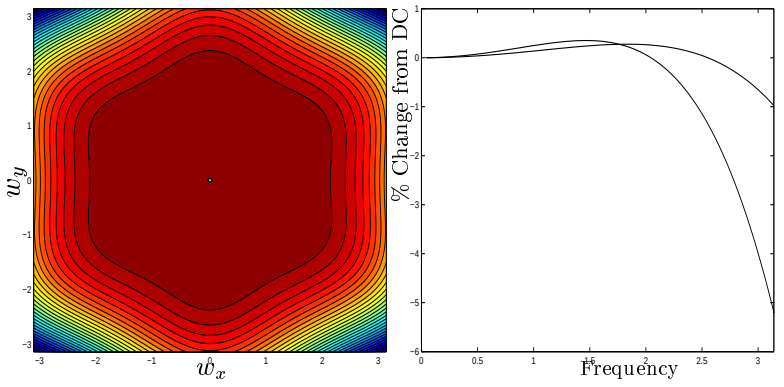

Figure 2-11: *(a) Angularly dependent dispersion error in the filtered mesh with* $a = -0.45$. *(b) Max and Min Dispersion Error in Filtered Mesh with* $a = -0.45$.

Mesh	Additions	Multiplications	Memory Locations
Standard	12	1	7
Filtered	24	7	13

Table 2.2: *Comparing computing requirements between the standard and allpass filtered waveguide meshes.*

2.6.2 Simulation

We now test the viability of the filtered mesh by comparing its performance with the standard mesh at high sample rates. Again we model a circular membrane struck at its centre with the same model parameters as before. We also include rimguides in each model. By ensuring the models are almost completely circular we are able to conclude that any errors in the models' frequency spectra have occurred solely due to dispersion error. We are then able to make a comparison of the two methods, standard and filtered mesh, in both suitability and performance. Shown in Table 2.2 is a description of the amount of processing and memory required for each method. It describes the number of additions, multiplications and memory locations required for each junction for each time step of a simulation. Shown in Figure 2-12 is a plot of the frequency output for a membrane model struck at its centre using the standard mesh at a sampling rate of $f_s = 66150Hz$. Again the resonant peaks are marked '+', with expected modes marked 'o'. It shows reasonable accuracy over the first twenty resonant modes as shown in Figure 2-14 with the error being entirely consistent with the dispersion. This is quite a heavy simulation to run, since the high sample rate results in a mesh of 44665 nodes. Compare this with the output of the allpass filtered mesh, ran at the same sample rate, as shown in Figure 2-13. This displays a high level of accuracy over the first twenty harmonics, with again the errors in each resonant mode (Figure 2-14)

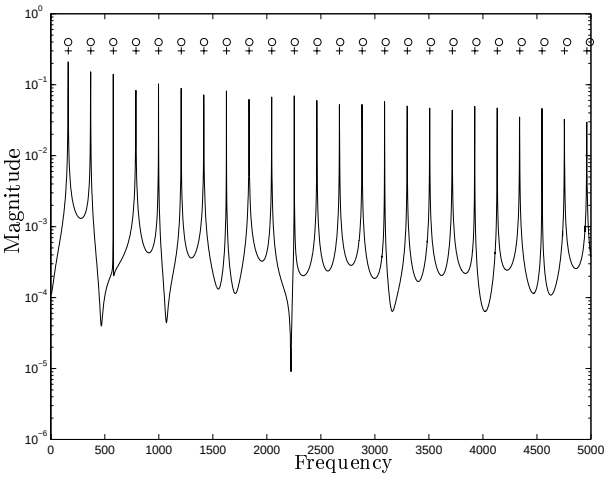

Figure 2-12: *Frequency Spectrum of Standard Mesh for* $f_s = 66150Hz$.

Mesh	F_s	Nodes	Additions	Multiplications	Memory Locations
Standard	66150	44665	3.546×10^{10}	2.995×10^9	312655
Filtered	66150	3403	5.403×10^9	1.576×10^9	44239
Filtered	88200	6007	1.272×10^{10}	3.709×10^9	78091

Table 2.3: *Performance Comparison Between Standard and Filtered Meshes.*

being predicted by the shape of the dispersion curve of Figure 2-11. Furthermore due to the slower average wave speed the mesh need only consist of some 3403 nodes. Note however the large error in the 20th mode. This is due to the double peaks which start to appear higher up the frequency spectrum. These double peaks are most probably a consequence of the angular dependence of the dispersion error in the case of the allpass filtered mesh as shown in Figure 2-11 which compromises the circular boundary. Double peaks can occur in the standard mesh, but to a lesser extent. It is important to note however the difference in the computational requirements of each method. Shown in Table 2.3 are the computational and memory requirements of each method. The table describes the number of additions and multiplications each method must perform to create one second of sound, and the number of memory locations required at each time step. Clearly the filtered mesh is much less of a burden, since it uses many fewer nodes. Thus we may consider increasing the sample rate still further and obtaining accurate results over a wide bandwidth using the filtered mesh. For example, by increasing the sample rate to $f_s = 88200$ we obtain a highly accurate model up to around $6000Hz$, as shown in Figure 2-15, with comparable computational resources as were used by the standard mesh at the lower sample rate, where accuracy was only maintained up to around $2500Hz$.

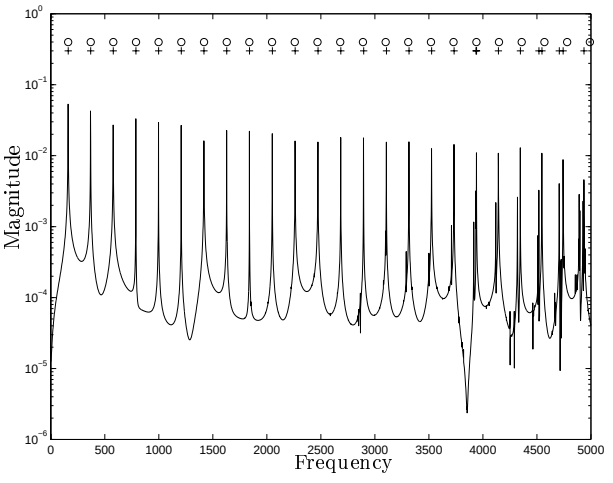

Figure 2-13: *Frequency Spectrum of Filtered Mesh for* $f_s = 66150Hz$.

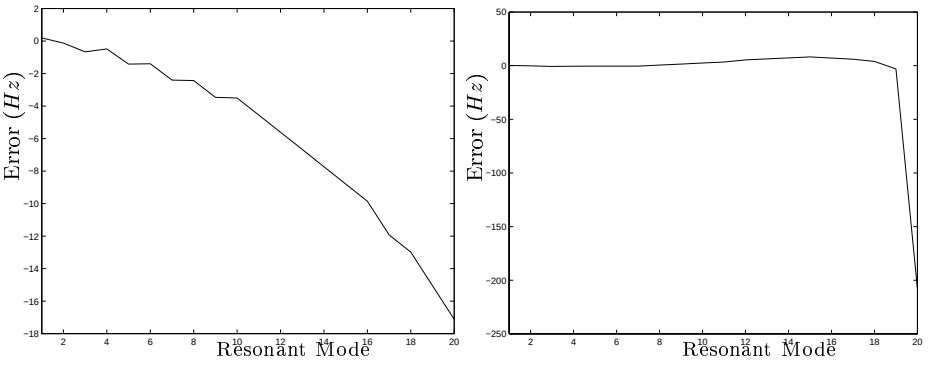

Figure 2-14: *(a)-Errors for Standard Mesh with* $f_s = 66150Hz$. *(b)-Errors for Filtered Mesh with* $f_s = 66150Hz$.

2.7 Conclusion and Discussion

In this chapter we have shown that a circular membrane may be accurately modelled using a triangular waveguide mesh. Furthermore the use of fractional length rimguides at the boundary improves the quality of the circular boundary implementation, and consequently the only errors in the simulation are due to dispersion. On line correction of dispersion error using embedded allpass filters can be used to improve the bandwidth of the simulation. However we believe it introduces some angular dependence to the dispersion which may compromise its immediately perceived improvements. The structure of having allpasses placed between nodes however could have a dual purpose in order to model tension modulation in membranes and we discuss this a little further in chapter 8. The filtered mesh provides a high level of accuracy over its useful bandwidth, out of which the signal seems to degrade rapidly. Using the standard mesh,

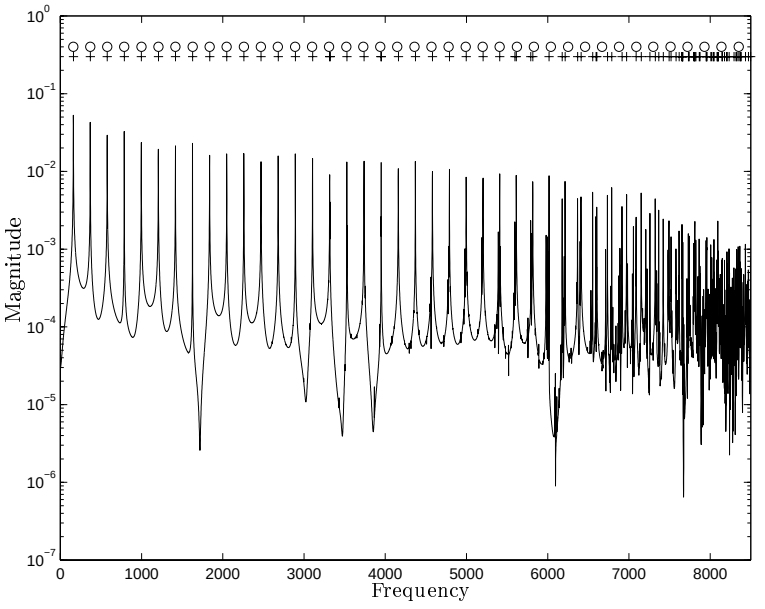

Figure 2-15: *Frequency Spectrum of Filtered Mesh for* $f_s = 88200Hz$.

we obtain a much more gentle increase in the error with increasing frequency, without the sudden change experienced with the filtered mesh. Thus if computational requirements are not an issue, then perhaps the standard mesh used at a high sample rate will suffice for reasonable membrane simulations. Otherwise, if a high level of accuracy is required over a particular bandwidth, then the allpass filtered mesh is suitable. In the former case, and the case where only 2D modelling is required, it may be better to frequency warp the output of a standard mesh to correct the dispersion error. Frequency warping has been used to improve the simulation results obtained by the waveguide mesh [43, 44, 45]. However, as it is a post-process, it could not be used whenever the mesh was required to interact, or be interfaced with another mesh. Thus we disregard it in the context of this thesis.

Chapter 3

3D Waveguide Meshes

In this chapter we simply extend the waveguide mesh method of the previous chapter into 3D. Different 3D mesh structures have previously been considered such as the 3D rectilinear mesh [41] and the tetrahedral mesh [55, 56]. Also a dodecahedral mesh has been presented in [18] and [27]. By way of analogy to the previous chapter we concentrate on the rectilinear and dodecahedral structures in this chapter. After discussing their construction and dispersion errors, we discuss the application to problems involving the modelling of rectangular and cylindrical 3D enclosures.

3.1 The Rectilinear 3D Mesh

The rectilinear waveguide mesh is a straightforward extension of the square mesh described previously. It is made up from 6-port scattering junctions arranged at integer valued spatial positions in each of the three axial directions. Analogously with the 2D case this mesh structure can quite easily be shown to be equivalent to a stable FDS for the 3D wave equation (A.1). It is useful to follow through the process as it also helps to understand the practical operation of the method. By writing the pressure at junction (i, j, k) by $P_{i,j,k}(n)$ we write the junction pressure in terms of travelling pressure waves into each port using the standard scattering junction equation (2.9), and proceed as

follows.

$$
\begin{aligned}
P_{i,j,k}(n+1) &= \frac{1}{3}\sum_{l=0}^{5} P^{+}_{i,j,k,l}(n+1) \\
&= \frac{1}{3}\Big[P^{-}_{i+1,j,k,2}(n) + P^{-}_{i,j+1,k,3}(n) + P^{-}_{i-1,j,k,0}(n) + P^{-}_{i,j-1,k,1}(n) + P^{-}_{i,j,k+1,5}(n) \\
&\qquad\qquad + P^{-}_{i,j,k-1,4}(n)\Big] \\
&= \frac{1}{3}\Big[P_{i+1,j,k}(n) + P_{i,j+1,k}(n) + P_{i-1,j,k}(n) + P_{i,j-1,k}(n) + P_{i,j,k+1}(n) + P_{i,j,k-1}(n)\Big] \\
&\quad - \frac{1}{3}\Big[P^{+}_{i+1,j,k,2}(n) + P^{+}_{i,j+1,k,3}(n) + P^{+}_{i-1,j,k,0}(n) + P^{+}_{i,j-1,k,1}(n) + P^{+}_{i,j,k+1,5}(n) \\
&\qquad\qquad + P^{+}_{i,j,k-1,4}(n)\Big] \\
&= \frac{1}{3}\Big[P_{i+1,j,k}(n) + P_{i,j+1,k}(n) + P_{i-1,j,k}(n) + P_{i,j-1,k}(n) + P_{i,j,k+1}(n) + P_{i,j,k-1}(n)\Big] \\
&\quad - \frac{1}{3}\sum_{l=0}^{5} P^{+}_{i,j,k,l}(n-1) \\
&= \frac{1}{3}\Big[P_{i+1,j,k}(n) + P_{i,j+1,k}(n) + P_{i-1,j,k}(n) + P_{i,j-1,k}(n) + P_{i,j,k+1}(n) + P_{i,j,k-1}(n)\Big] \\
&\quad - P_{i,j,k}(n-1).
\end{aligned}
$$

Now, simplifying this expression and subtracting $2P_{i,j,k}(n)$ from each side, we reduce to

$$
\begin{aligned}
P_{i,j,k}(n+1) - 2P_{i,j,k}(n) + P_{i,j,k}(n-1) &= \\
\frac{1}{3}\left[P_{i+1,j,k}(n) - 2P_{i,j,k}(n) + P_{i-1,j,k}(n)\right] \\
+\frac{1}{3}\left[P_{i,j+1,k}(n) - 2P_{i,j,k}(n) + P_{i,j-1,k}(n)\right] \\
+\frac{1}{3}\left[P_{i,j,k+1}(n) - 2P_{i,j,k}(n) + P_{i,j,k-1}(n)\right]
\end{aligned} \tag{3.1}
$$

and this is quite clearly a centered FDS for the 3D wave equation by comparing to equation (B.1) in Appendix B.2. We may hence deduce the relationship between the spatial step Δ and time step T as $Tc/\Delta = 1/\sqrt{3}$. Thus, the size of a spatial step in the mesh may be calculated from the sample rate f_s as

$$\Delta = \frac{\sqrt{3}c}{f_s}.$$

The dispersion factor can be calculated in the usual manner by computing the spectral amplification factor $G(\mathbf{w})$, which is now a function of the 3D frequency vector $\mathbf{w} =$

$(w_x, w_y, w_z)^T$. We again have

$$G(\mathbf{w}) = \frac{-b \pm \sqrt{b^2 - 4}}{2}, \tag{3.2}$$

where for the rectilinear mesh

$$b = -\frac{2}{3}\left(\cos(w_x) + \cos(w_y) + \cos(w_z)\right).$$

We note that again $b^2 < 4$ so that the amplification factor is complex, with unit magnitude, and hence the scheme is stable and lossless. The dispersion is calculated as usual from the phase of the amplification factor as

$$K(\mathbf{w}) = \frac{1}{|\mathbf{w}|}\tan^{-1}\left(\frac{\sqrt{4 - b^2}}{-b}\right),$$

where we note that for a 3D waveguide mesh the DC wave speed is $K(0) = \frac{1}{\sqrt{3}}$. Shown in Figure 3-1 are dispersion plots from various viewpoints in the (w_x, w_y, w_z) plane. The first two plots are identical since the mesh is a 2D square mesh when viewed along any of the axial directions. Notice how in each plane of view we incur a direction dependent error, and that this dependence is not the same when we change the plane of view. This inconsistency in the dispersion characteristics of the mesh makes it quite undesirable. Another mesh which offers similarly irregular dispersion characteristics, but with a multiply free implementation is the tetrahedral mesh described in [55] and [56]. We will disregard it here as we concern ourselves with accuracy over speed of calculation.

3.2 The 3D Dodecahedral Mesh

We have already encountered in section 2.5 a preference for mesh structures which display a uniform angular dependence in the dispersion error. For the 2D case we saw how such a characteristic could be obtained using a triangular mesh geometry or perhaps the interpolated structure described in Appendix B.4.2. For the 3D case we consider a mesh based upon the densest arrangement of nodes within 3D space which allows orientation-less mesh connections, as has been presented in both [18] and [27]. This mesh is constructed of 12-port scattering junctions whose neighbours are placed according to the coordinates described in Table 3.1. Shown in Figure 3-2 is a plan view of a scattering junction in the mesh, thus we may note that the mesh is triangular in each horizontal plane.

The mesh is named the *Dodecahedral* mesh, since the element of volume which each

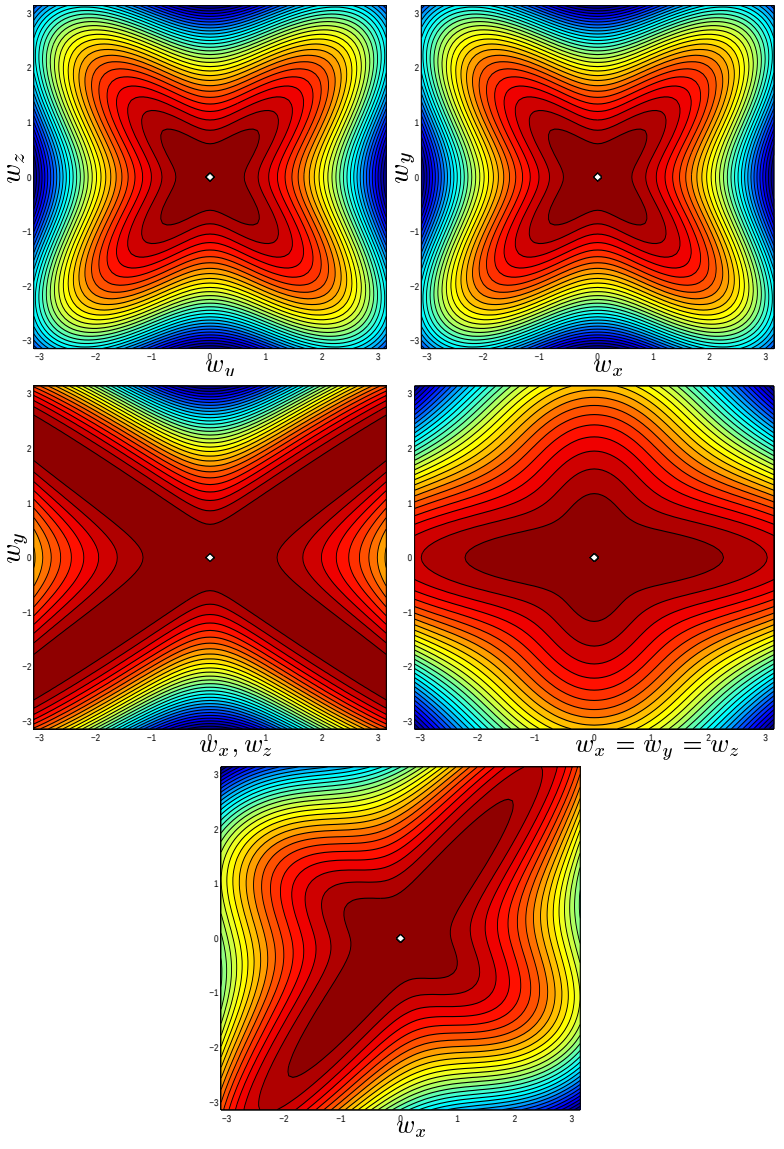

Figure 3-1: *Dispersion plots for the standard rectilinear mesh. (a)* $w_x = 0$, *(b)* $w_z = 0$, *(c)* $w_x = w_z$, *(d)* $w_x = w_y = w_z$, *(e)* $w_y = w_z = \frac{1}{\sqrt{3}} w_x$

Neighbour	Co-ordinate	Neighbour	Co-ordinate
0	$(1, 0, 0)$	6	$(0, \frac{1}{\sqrt{3}}, \sqrt{\frac{2}{3}})$
1	$(\frac{1}{2}, \frac{\sqrt{3}}{2}, 0)$	7	$(-\frac{1}{2}, -\frac{1}{2\sqrt{3}}, \sqrt{\frac{2}{3}})$
2	$(-\frac{1}{2}, \frac{\sqrt{3}}{2}, 0)$	8	$(\frac{1}{2}, -\frac{1}{2\sqrt{3}}, \sqrt{\frac{2}{3}})$
3	$(-1, 0, 0)$	9	$(\frac{1}{2}, \frac{1}{2\sqrt{3}}, -\sqrt{\frac{2}{3}})$
4	$(-\frac{1}{2}, -\frac{\sqrt{3}}{2}, 0)$	10	$(-\frac{1}{2}, \frac{1}{2\sqrt{3}}, -\sqrt{\frac{2}{3}})$
5	$(\frac{1}{2}, -\frac{\sqrt{3}}{2}, 0)$	11	$(0, -\frac{1}{\sqrt{3}}, \sqrt{\frac{2}{3}})$

Table 3.1: *Coordinates of neighbouring mesh points for node at* $(0, 0, 0)$

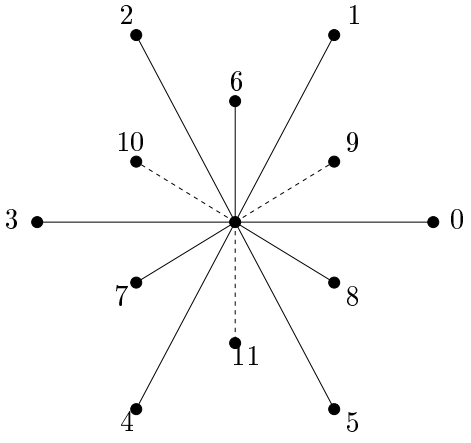

Figure 3-2: *Junction in the Dodecahedral Mesh*

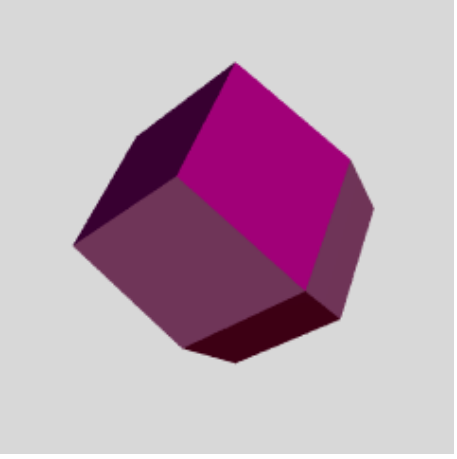

Figure 3-3: *A Rhombic Dodecahedron*

node represents is a 12 sided shape called a Rhombic Dodecahedron [35] (Figure 3-3). The mesh operations may be summarised as follows

$$
\begin{aligned}
P^{+}_{i,j,k,0}(n) &= P^{-}_{i+1,j,k,3}(n-1) \\
P^{+}_{i,j,k,1}(n) &= P^{-}_{i+\frac{1}{2},j+\frac{\sqrt{3}}{2},k,4}(n-1) \\
P^{+}_{i,j,k,2}(n) &= P^{-}_{i-\frac{1}{2},j+\frac{\sqrt{3}}{2},k,5}(n-1) \\
P^{+}_{i,j,k,3}(n) &= P^{-}_{i-1,j,k,0}(n-1) \\
P^{+}_{i,j,k,4}(n) &= P^{-}_{i-\frac{1}{2},j-\frac{\sqrt{3}}{2},k,1}(n-1) \\
P^{+}_{i,j,k,5}(n) &= P^{-}_{i+\frac{1}{2},j-\frac{\sqrt{3}}{2},k,2}(n-1) \\
P^{+}_{i,j,k,6}(n) &= P^{-}_{i,j+\frac{1}{\sqrt{3}},k+\sqrt{\frac{2}{3}},11}(n-1) \\
P^{+}_{i,j,k,7}(n) &= P^{-}_{i-\frac{1}{2},j-\frac{1}{2\sqrt{3}},k+\sqrt{\frac{2}{3}},9}(n-1) \\
P^{+}_{i,j,k,8}(n) &= P^{-}_{i+\frac{1}{2},j-\frac{1}{2\sqrt{3}},k+\sqrt{\frac{2}{3}},10}(n-1) \\
P^{+}_{i,j,k,9}(n) &= P^{-}_{i+\frac{1}{2},j+\frac{1}{2\sqrt{3}},k-\sqrt{\frac{2}{3}},7}(n-1) \\
P^{+}_{i,j,k,10}(n) &= P^{-}_{i-\frac{1}{2},j+\frac{1}{2\sqrt{3}},k-\sqrt{\frac{2}{3}},8}(n-1) \\
P^{+}_{i,j,k,11}(n) &= P^{-}_{i,j-\frac{1}{\sqrt{3}},k-\sqrt{\frac{2}{3}},6}(n-1).
\end{aligned}
$$

where $P^{\pm}_{i,j,k,l}(n)$ represents the incoming or outgoing velocity in direction l from the junction at mesh coordinates (i,j,k) and at time step n, and where $0 \leq l \leq 11$.

By considering and manipulating the junction pressure equations it is easily shown that this mesh is equivalent to the following FDS,

$$
\begin{aligned}
P_{i,j,k}(n+1) - 2P_{i,j,k}(n) + P_{i,j,k}(n-1) = \frac{1}{6}\Big[& P_{i+1,j,k}(n) - 2P_{i,j,k}(n) + P_{i-1,j,k}(n) \\
& + P_{i+\frac{1}{2},j+\frac{\sqrt{3}}{2},k}(n) - 2P_{i,j,k}(n) + P_{i-\frac{1}{2},j+\frac{\sqrt{3}}{2},k}(n) \\
& + P_{i-\frac{1}{2},j-\frac{\sqrt{3}}{2},k}(n) - 2P_{i,j,k}(n) + P_{i+\frac{1}{2},j-\frac{\sqrt{3}}{2},k}(n) \\
& + P_{i,j+\frac{1}{\sqrt{3}},k+\sqrt{\frac{2}{3}}}(n) - 2P_{i,j,k}(n) + P_{i,j-\frac{1}{\sqrt{3}},k-\sqrt{\frac{2}{3}}}(n) \\
& + P_{i-\frac{1}{2},j-\frac{1}{2\sqrt{3}},k+\sqrt{\frac{2}{3}}}(n) - 2P_{i,j,k}(n) + P_{i+\frac{1}{2},j+\frac{1}{2\sqrt{3}},k-\sqrt{\frac{2}{3}}}(n) \\
& + P_{i+\frac{1}{2},j-\frac{1}{2\sqrt{3}},k+\sqrt{\frac{2}{3}}}(n) - 2P_{i,j,k}(n) + P_{i-\frac{1}{2},j+\frac{1}{2\sqrt{3}},k-\sqrt{\frac{2}{3}}}(n)\Big].
\end{aligned}
$$

Clearly this is a centered FDS for the 3D wave equation when the spatial difference is formed using the allowed propagation direction for axes as described by equation (B.2)

of Appendix B.2. We may also calculate the dispersion factor by using

$$b = \frac{1}{3}\left[\cos(w_x) + \cos\left(\frac{1}{2}w_x + \frac{\sqrt{3}}{2}w_y\right) + \cos\left(\frac{1}{2}w_x - \frac{\sqrt{3}}{2}w_y\right)\right.$$
$$\left. + \cos\left(\frac{1}{2}w_x + \frac{1}{2\sqrt{3}}w_y - \sqrt{\frac{2}{3}}w_z\right) + \cos\left(\frac{1}{2}w_x - \frac{1}{2\sqrt{3}}w_y + \sqrt{\frac{2}{3}}w_z\right)\right].$$

in equation 3.2. We plot the dispersion characteristics in Figure 3-4 and compare to the 3D square mesh dispersions of Figure 3-1. The new mesh certainly offers much better performance since the error is nearly independent of direction, and there is little variation between the different planar viewpoints. A mesh with an even better performance in the dispersion battle is the tri-linearly interpolated mesh discussed in Appendix B.4.2. Although highly computationally expensive, it offers near direction independent dispersion error through every plane of view, as shown in Figure B-5.

3.3 Using 3D meshes to model Acoustic Spaces

We now consider using a 3D waveguide mesh to model the propagation of sound pressure waves in air. The rectilinear and interpolated meshes have been used to model square shaped rooms in [40] and [41], and the interior of a kettle drum (semi-ellipsoidal) has been modelled in [27] using the dodecahedral mesh. In this section we will demonstrate the practical use of 3D meshes by modelling cubic, rectangular and cylindrical enclosures of air. The biggest problem to be encountered when designing a simulation is the boundary and there are two points of consideration. The first of these is to define the type of boundary, and to that end we shall assume a rigid boundary, and describe how to implement such a condition below. Secondly we must consider the shape of the boundary and geometry of the mesh. Using a square mesh for a square boundary is quite straightforward, however, if the mesh were not of such a regular geometry, or the boundary were of a different shape, say curved, then difficulties clearly arise.

3.3.1 Boundary Conditions

In order to present a general model which could easily be adapted to model differently shaped domains, we approach the boundary problem by including *rimguides* much as we did in section 2.5 for membrane simulations. When using either the square or interpolated meshes to model square enclosures it would be possible to adjust the sample rate so as to have an exact number of nodes in each direction. However, any output signal would then have to be resampled and considering that most domains will

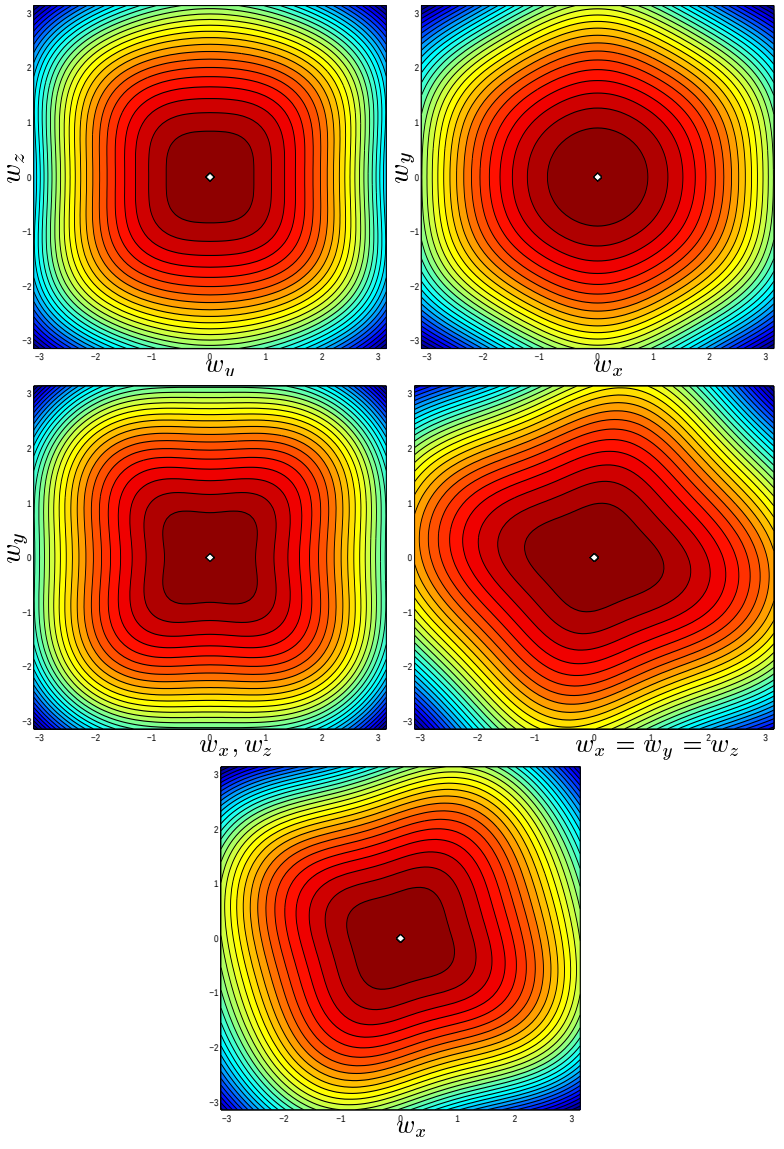

Figure 3-4: *Dispersion plots for the dodecahedral/cuboctahedral mesh. (a)* $w_x = 0$, *(b)* $w_z = 0$, *(c)* $w_x = w_z$, *(d)* $w_x = w_y = w_z$, *(e)* $w_y = w_z = \frac{1}{\sqrt{3}} w_x$

not have exactly square boundaries, we investigate the use of other mesh structures and the use of rimguides. First we formulate the boundary problem in the finite difference domain, and describe its analogy in the waveguide domain.

Now, the boundary conditions for pressure waves are not quite as they were for transverse waves on a membrane or string. For a perfectly rigid boundary at say, $x = l$, we must have $\frac{\partial p}{\partial x} = 0$ [15, 33]. This means setting the boundary node to zero will not be appropriate. In other words, the travelling waves at the boundary do not incur an inverting reflection. For the case of the standard rectilinear mesh we may consider approximating the boundary condition on the spatial derivative by setting $P_{i,j,k}(n) - P_{i+1,j,k}(n) = 0$, that is $P_{i,j,k}(n) = P_{i+1,j,k}(n)$. Then the FDS of equation (3.1) becomes

$$\begin{aligned} P_{i,j,k}(n+1) - 2P_{i,j,k}(n) + P_{i,j,k}(n-1) = \frac{1}{3}\Big[P_{i+1,j,k}(n) - P_{i,j,k}(n)\Big] \\ + \frac{1}{3}\Big[P_{i,j+1,k}(n) - 2P_{i,j,k}(n) + P_{i,j-1,k}(n)\Big] \\ + \frac{1}{3}\Big[P_{i,j,k+1}(n) - 2P_{i,j,k}(n) + P_{i,j,k-1}(n)\Big]. \end{aligned} \tag{3.3}$$

Now terminating our mesh in the x-direction with a non-inverting self loop (so that $P^+_{i,j,k,0}(n) = P^-_{i,j,k,0}(n-1)$) means the junction velocity calculation may proceed as follows

$$\begin{aligned} P_{i,j,k}(n+1) &= \frac{1}{3}\sum_{l=0}^{5} P^+_{i,j,k,l}(n+1) \\ &= \frac{1}{3}\Big[P^-_{i,j,k,0}(n) + P^-_{i,j+1,k,3}(n) + P^-_{i-1,j,k,0}(n) + P^-_{i,j-1,k,1}(n) + P^-_{i,j,k+1,5}(n) \\ &\qquad + P^-_{i,j,k-1,4}(n)\Big] \\ &= \frac{1}{3}\Big[P_{i,j,k}(n) + P_{i,j+1,k}(n) + P_{i-1,j,k}(n) + P_{i,j-1,k}(n) + P_{i,j,k+1}(n) + P_{i,j,k-1}(n)\Big] \\ &\quad - \frac{1}{3}\Big[P^+_{i,j,k,0}(n) + P^+_{i,j+1,k,3}(n) + P^+_{i-1,j,k,0}(n) + P^+_{i,j-1,k,1}(n) + P^+_{i,j,k+1,5}(n) \\ &\qquad + P^+_{i,j,k-1,4}(n)\Big] \\ &= \frac{1}{3}\Big[P_{i,j,k}(n) + P_{i,j+1,k}(n) + P_{i-1,j,k}(n) + P_{i,j-1,k}(n) + P_{i,j,k+1}(n) + P_{i,j,k-1}(n)\Big] \\ &\quad - \frac{1}{3}\sum_{l=0}^{5} P^-_{i,j,k,l}(n-1) \\ &= \frac{1}{3}\Big[P_{i,j,k}(n) + P_{i,j+1,k}(n) + P_{i-1,j,k}(n) + P_{i,j-1,k}(n) + P_{i,j,k+1}(n) + P_{i,j,k-1}(n)\Big] \\ &\quad - P_{i,j,k}(n-1), \end{aligned}$$

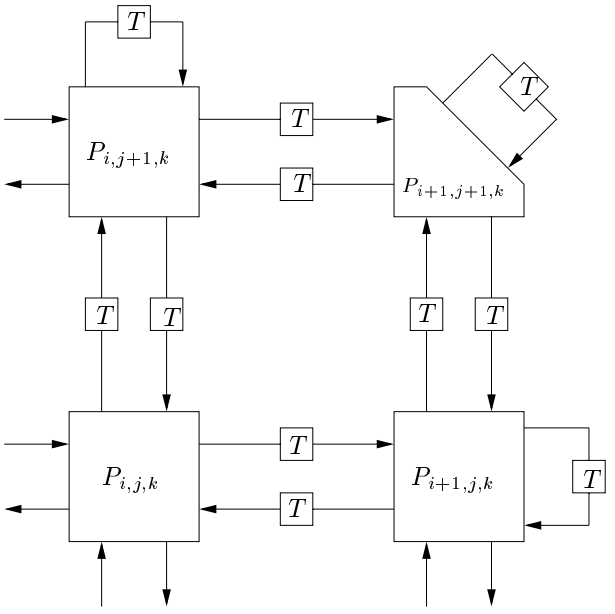

Figure 3-5: *Boundary Conditions for Square Mesh*

and this is quite clearly identical to the FDS of equation (3.3). Such self-loops model a spatial distance of half a spatial sample out to the boundary, and half a spatial sample back. In our simulations we shall also be considering the use of rimguides to model spatial distances other than a half.

3.3.2 Sensitivity of Resonant Modes to Changes in Room Size

Before we begin our discussions on simulation of acoustic spaces using either the square or dodecahedral meshes, it is important to make note of a few points regarding the expected resonant modes of a particularly shaped room. Beginning with a cubical room, we may calculate its resonant modes using the following equation derived in Appendix A.1.3,

$$f_{lmn} = \frac{c}{2L}(l^2 + m^2 + n^2)^{\frac{1}{2}}. \tag{3.4}$$

Table 3.2 shows the values of the resonant modes for small changes in room length. Note that the fundamental mode can change by up $13Hz$ while the 8th mode moves by almost $40Hz$. However the change in length would be almost inperceptible to the human eye.

A similar sensitivity can be observed for cylindrically shaped spaces. In this case the resonant modes of a cavity of radius r metres and height h metres can be calculated

Mode	$L = 0.5m$	$L = 0.51$	$L = 0.52$
f_1	344.0	337.3	330.8
f_2	486.5	477.0	467.8
f_3	595.8	584.1	572.9
f_4	688.0	674.5	661.5
f_5	769.2	754.1	739.6
f_6	842.6	826.1	810.2
f_7	973.0	953.9	935.6
f_8	1032.0	1011.8	992.3

Table 3.2: *Resonant Modes for different sized square enclosures.*

Mode	$h = 0.5m, r = 0.25m$	$h = 0.52m, r = 0.26m$
f_{001}	344.0	330.8
f_{002}	688.0	661.5
f_{010}	839.1	806.9
f_{011}	906.9	872.0
f_{003}	1032.0	992.3
f_{012}	1085.1	1043.4
f_{013}	1330.1	1278.9
f_{004}	1376.0	1323.1

Table 3.3: *Resonant Modes for different sized cylindrical enclosures.*

using

$$f_{mnl} = \frac{c}{2\pi}\sqrt{\left(\frac{\alpha_{mn}}{r}\right)^2 + \left(\frac{l\pi}{h}\right)^2}, \tag{3.5}$$

where α_{mn} is the nth zero of J'_m, the derivative of the mth Bessel Function. The values of α_{0n} for $n \leq 4$ are

$$\alpha_{01} = 3.83171, \alpha_{01} = 7.01559, \alpha_{01} = 10.17347, \alpha_{01} = 13.32369.$$

Expected modes for some small changes in the dimensions are shown in Table 3.3 where we excite the air along the central axis of the cylinder. In this instance the change in the circular modes is quite large. Thus we anticipate that it will be important to model correctly the circular boundary. In general, we may expect that due to direction dependent dispersion error in both the square and dodecahedral meshes we may find it difficult to model correctly all the modes for a given space.

Mode	Modelled	Expected (length l_m)	Mag Error	Expected (length l)
f_{100}	335	335.0	0.0	344.0
f_{110}	474	473.7	0.3	486.5
f_{111}	580	580.2	0.2	595.8
f_{200}	668	669.9	1.9	688.0
f_{210}	748	749.0	1.0	769.2
f_{211}	819	820.5	0.5	842.6
f_{220}	946	947.4	1.4	973.0
$f_{221} = f_{300}$	998	1004.9	6.9	1032.0
f_{310}	1053	1059.2	6.2	1087.8
f_{311}	1106	1110.9	4.9	1140.9
f_{222}	1160	1160.3	0.3	1191.7
f_{320}	1204	1207.7	3.3	1240.3
f_{321}	1250	1253.3	3.3	1287.1
$f_{322} = f_{410}$	1324	1339.8	15.8	1376.0
f_{330}	1380	1381.1	1.1	1418.3
f_{331}	1416	1421.1	5.1	1459.5
f_{332}	1486	1498.0	12.0	1538.4

Table 3.4: *Performance Evaluation for Square Mesh.*

3.3.3 Simulation of a Rectangular Space

We begin by considering a model for a cubical room of length $l = 0.5$ metres. Working at a sample rate of $f_s = 22050Hz$, the size of a spatial sample in the mesh may be calculated as $\Delta = \frac{\sqrt{3}c}{f_s} \approx 0.0270216$ where the speed of sound was taken to be $c = 344ms^{-1}$. The required mesh must therefore have length $L = l/\Delta = 18.503716$ waveguides.

Using A Square Mesh

Firstly we consider simply fitting a square mesh within the required boundary L, and implement the boundary simply by applying self-loops at the mesh boundary as described previously. Each self loop measures a half spatial sample out to the boundary and a half spatial sample back again. Thus the overall modelled length will be $L_m = 18 + 1$ waveguides, or equivalently, $l_m = 19\Delta = 0.5134104$ metres. Consequently this approximation for the boundary will yield an expected fundamental of $f_1 = c/2l_m = 335Hz$. Shown in Table 3.4 are the resonant modes as measured from the output of our waveguide simulation compared with the expected modes both for a square space of length l_m and a room at the original desired length l. This simulation is an excellent example to illustrate the dispersion error of Figure 3-1 in action. We observe very little error in the fundamental mode and the purely diagonal modes f_{111} and

Mode	Modelled	True	Mag Error
f_{100}	353	344.0	9.0
f_{110}	493	486.5	5.5
f_{111}	596	595.8	0.2
f_{200}	703	688.0	5.0
f_{210}	776	769.2	6.8
f_{211}	840	842.6	2.6
f_{220}	982	973.0	9.0
f_{300}	1029	1032.0	3.0
f_{310}	1089	1087.8	1.2
f_{311}	1127	1140.9	13.9
f_{222}	1191	1191.7	0.7
f_{320}	1246	1240.3	5.7
f_{321}	1276	1287.1	11.1

Table 3.5: *Performance Evaluation for Square Mesh Using Rimguides.*

f_{222}, while the horizontal modes f_{200} and f_{300} incur the largest error initially. Higher up the spectrum we see that as a general rule accuracy decreases with frequency and that the errors are inconsistent, in keeping with the angular dependence of the dispersion error. Finally we note that, although this simulation does not model the desired size correctly, the modes are in keeping with a square space to a reasonable level of accuracy. We may attribute this level of accuracy to the close relationship between the boundary shape and the mesh geometry.

Let us now consider the inclusion of fractional length rimguides in an attempt truly to model the target boundary. Recalling the discussion of section 2.5 we set the mesh boundary to 0.75 spatial samples smaller all round. That is the mesh fits within a boundary of length $L_m = l/\Delta - 1.5 = 17.00362$ waveguides. The remaining size is made up by using fractional length rimguides to model the delay to and from the boundary. The output of such a simulation is presented in Table 3.5. At first glance these results may seem a little disappointing. However, the errors observed here are certainly smaller than those found when modelling the space by a mesh whose length was the closest integer number of samples to the desired amount. Again we note the directional dependence of the dispersion error is clearly prevalent. Furthermore we also find that the sequence of simulated mode frequencies is consistently greater than the desired frequencies. Thus we may suppose that the modelled space is in fact too small. When preparing the simulation we found that each rimguide was required to implement a delay $d = 2.50374$ samples. Thus the model mesh terminated some 1.25187 spatial samples from the desired boundary. By simply using 1D waveguides to model this intermediate space we are effectively reducing the mesh density near the boundary,

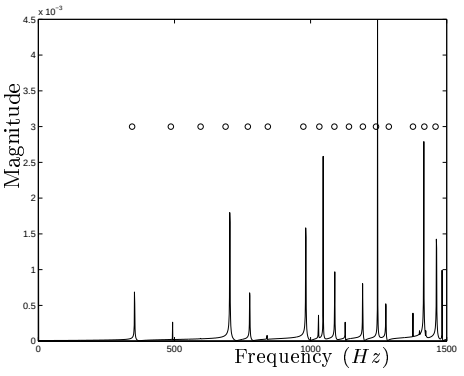

Figure 3-6: *Frequency Spectrum For Square Mesh.*

and consequently the modelled space could effectively appear to be too small. We describe this in more detail in the next section. Finally we note that we observed also some extraneous modes which can be seen in Figure 3-6 where the circles represent the true mode positions. Extra modes occur higher up the spectrum in the form of triple peaks, especially around the 15th mode, although the energy in these extra modes is small. These superfluous modes are probably generated since the direction dependence of the dispersion error and imperfection of the allpass filter cause the cubic shape not to be completely upheld at all frequencies.

Using the Dodecahedral Mesh

Next we consider simulating our cubic space using a dodecahedral mesh. First we consider the implementation of the mesh within the target boundary $L = l/\Delta$ with simple self-loops terminating the mesh. The output of such a simulation is shown in the left-hand plot of Figure 3-7, where as usual the expected modes are shown as circles. We found that the mode frequencies observed in the simulation were systematically too low. This is because the dodecahedral mesh is of a higher density and hence fills up the space closer to the boundary. Consequently, the self loops which terminate the mesh will typically extend outwith the desired boundary. We also note that each mode was in fact represented by three peaks. This is because the dodecahedral mesh is not the same in each axial direction, so that it does not naturally fit the boundary. Thus the simulated space is no longer cubic, but will have a rectangular cross section. Thus we consider using the fractional length rimguides to improve the square boundary shape. Such a simulation is summarised by the right-hand plot of Figure 3-7. This plot shows that the resonant peaks are much better resolved and the although it is not perfect, we are closer to the desired cubic shape. Futhermore we observed that each of the resonant mode clusters were centred closer to the desired mode frequency with the rimguides

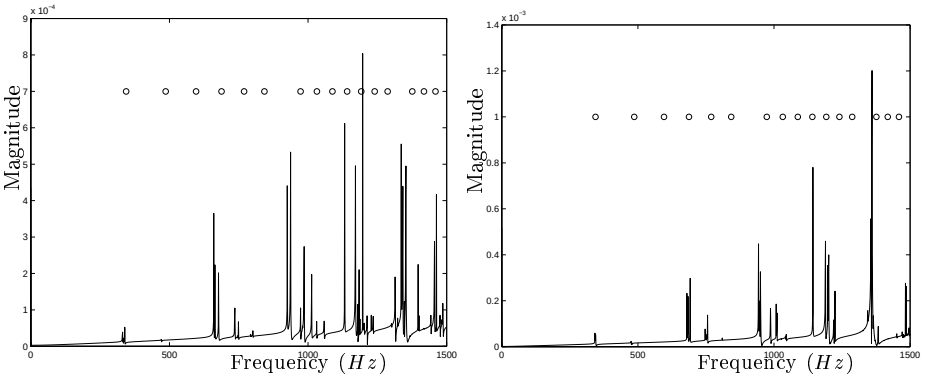

Figure 3-7: *Frequency Spectra For Dodecahedral Mesh Simulations of Cubic Enclosures.*

Mode	Modelled	True	Mag Error
f_{001}	286	286.7	0.7
f_{010}	344	344.0	0.0
f_{100}	436	430.0	6.0
f_{101}	510	516.8	6.8
f_{110}	541	550.7	9.7
f_{002}	570	573.3	3.3
f_{020}	684	688.0	4.0

Table 3.6: *Performance Evaluation for Dodecaheral Mesh Simulation of Rectangular Enclosure.*

than without. It is also worth noting that the mode errors were more consistently spread across the frequency spectrum, generally increasing with increasing frequency, which was to be expected since the dispersion error of the dodecahedral mesh is much less direction dependent than its square mesh counterpart.

We have seen that when modelling a cubic enclosure, it is perhaps better to use a square mesh, since its geometry will naturally fit the boundary shape. However we also include the results of a simulation of a dodecahedral mesh applied to a rectangular enclosure. The space we chose had length $l = 0.4m$, width $w = 0.5m$, and height $h = 0.6m$. Results of the simulation are shown in Table 3.6 where the observed resonances are compared against the expected mode frequencies as calculated using equation (A.3). A good level of accuracy is achieved despite the nature of the boundary.

3.3.4 Simulation of a Cylindrical Space

Let us now consider application of our mesh structures to the problem of simulating a cylindrical enclosure. This type of enclosure will require to be modelled when dealing with the drum model in the next chapter. We chose a cylinder of radius $r = 0.25$

Mode	Modelled	Expected (h_m, r_m)	Mag Error	Expected (h, r)	Mag Error
f_{001}	335	335.0	0.0	344.0	9.0
f_{002}	668	670.0	2.0	688.0	20.0
f_{010}	823	823.0	0.0	839.1	16.1
f_{011}	889	888.6	0.4	906.9	17.9
f_{003}	998	1005.1	7.1	1032.0	34.0
f_{012}	1062	1061.3	0.7	1085.1	23.1
f_{013}	1297	1299.0	2.0	1330.1	33.1
f_{004}	1323	1340.1	17.1	1376.0	53.0

Table 3.7: *Performance Evaluation for Cylinder Using a Square Mesh .*

metres and height $h = 0.5$ metres for our test case. The true resonant modes may be calculated from equation (3.5) and are listed in Table 3.3. As with the case for a rectangular room we apply our models at a sample rate $f_s = 22050Hz$ resulting in a spatial sample size $\Delta = 0.0270216$. Consequently the ideal mesh should have radius $R = 9.251870$ waveguides and height $H = 18.50374$ waveguides.

Using The Square Mesh

We begin with a square mesh. First of all we consider fitting the mesh within the desired ideal boundary, and terminating with simple self-loops, so as to impose an non-inverting reflection at the boundary. Consequently we may expect our mesh to have an operational height $h_m = (18 + 1)\Delta = 0.5134104$ metres as encountered previously when modelling the cubic enclosure. Results of the simulation are summarised in Table 3.7 when the mesh was excited along the central axis. We compare the results to two expected outputs. First we consider the expected output for a cylinder of height h_m and whose radius matches that predicted by the first circular mode, that is $r_m = 0.2549$. A cylinder of this radius should provide a fundamental circular mode $f_{010} = 823Hz$. Also note that $r_m \approx (9 + \frac{1}{2})\Delta$ which is an approximation to the average radius around the staircase boundary imposed by the mesh. We also include the desired modes for the real cylinder for comparison. While the mode positions are quite clearly inaccurate when compared to the desired modes of the given cylinder, there remains a self-correctedness about the modes when compared to a cylinder of height h_m and radius r_m. This shows that although the mesh is slightly too large, it has roughly modelled a cylindrical shape. Again, we note that the magnitude of the error increases with frequency and behaves according to the dispersion error.

We now consider the introduction of rimguides in order to model a cylinder of the desired dimensions. The results of our simulation are shown in Table 3.8. As with the case for the square mesh we note that the frequencies of the modes are systemati-

Mode	Modelled	Expected (h, r)	Mag Error
f_{001}	352	344.0	8.0
f_{002}	700	688.0	12.0
f_{010}	869	839.1	29.9
f_{011}	926	906.9	19.9
f_{003}	1041	1032.0	9.0
f_{012}	1111	1085.1	25.9
f_{013}	1360	1330.1	29.9
f_{004}	1370	1376.0	6.0

Table 3.8: *Performance Evaluation for Cylinder Using a Square Mesh With Rimguides.*

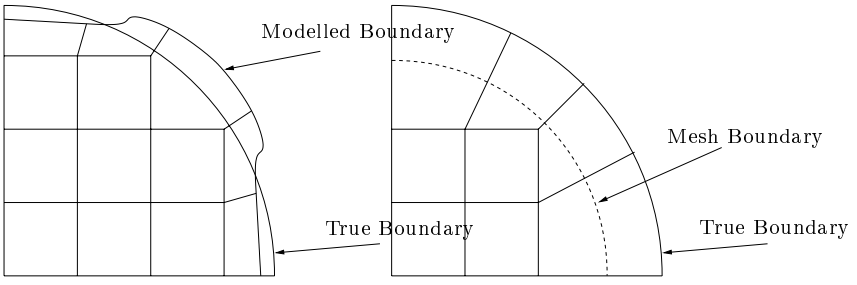

Figure 3-8: *Boundary implementations at the circular boundary of a cylindrical enclosure using a square mesh.*

cally too high. Again we discovered that the mesh was terminated quite far from the boundary, resulting in relatively long rimguide lengths, particularly when dealing with the circular boundary. The resultant loss in mesh density near the boundary means the modelled space is slightly too small. This problem is less severe near the vertical boundaries at the top and bottom of the cylinder, and consequently these modes are more accurately modelled.

A comparison of the two boundary methods, the staircase boundary and the rimguide method, is summarised in Figure 3-8. This clearly show that the effective modelled shape using the staircase method is too large, and not truly circular, but that the mesh fills much of the space. The right hand plot of Figure 3-8 shows that using rimguides will compromise the mesh density, since the rimguides must be of at least 0.75 spatial samples long. Consequently the mesh will consist of fewer nodes, and the the modelled space will appear a little too small, giving mode frequencies which are too high.

Using the Dodecahedral Mesh

Finally we apply the dodecahedral mesh to the problem of modelling the cylindrical air cavity. Shown in Table 3.9 are the positions of the resonant modes observed in

Mode	Expected	Modelled	Mag Error	Modelled (Rimguides)	Mag Error
f_{001}	344.0	331	13.0	341	3.0
f_{002}	688.0	662	26.0	676	12.0
f_{010}	839.1	832	7.1	858	18.9
f_{011}	906.9	889	12.9	907	0.1
f_{003}	1032.0	989	43.0	1000	32.0
f_{012}	1085.1	1059	26.1	1085	0.1
f_{013}	1330.1	1290	40.1	1326	4.1

Table 3.9: *Performance Evaluation for Cylinder Using a Dodecahedral Mesh.*

simulations using a simplified staircase boundary, and when applying rimguides. Using rimguides clearly improves the quality of the simulation over the simplified case, and indeed offers generally improved results over the same simulation using a square mesh. Inconsistencies in the errors are mostly due to non-regularity of the dodecahedral mesh structure. Recall that this means straight edges (edges perpendicular to the axial directions), of which the cylinder has two, are not naturally well represented using the dodecahedral mesh structure.

3.4 Conclusion and Discussion

In this chapter we have discussed the application of two mesh structures to the problem of 3D acoustic modelling. We described the 3D-square and dodecahedral mesh structures and showed each was equivalent to a FDS for the 3D wave equation. Consequently we were able to compare dispersion characteristics and conjectured that, due to a smaller direction dependence of the dispersion error, the dodecahedral mesh structure would be preferred. It is also probable that this mesh structure should exhibit a larger usable bandwidth, due to its increased density, much in the same way that a triangular mesh offered a larger bandwidth than a square mesh in 2D [18]. We then went on to discuss practical implementations of these mesh structures and considered modelling cubic, rectangular and cylindrical enclosures of air. We found that we could generally improve the quality of the simulations using rimguides. However we also highlighted a drawback with the rimguides, in that for certain boundaries, due to the minimum delay imposed by the allpass filter, we often required rimguides of quite a long length. This meant we compromised mesh density near the boundary and hence were unable to achieve as high a level of accuracy as was desired. Furthermore, we observed that the choice of mesh structure was also dependent on the shape of the space. Square and cylindrical spaces have boundaries at right angles to the axial directions, thus the square mesh naturally fitted this boundary quite well. In general however, for a more

arbitrary boundary shape, the dodecahedral mesh structure would be preferred. For example the dodecahedral mesh has been implemented to good use to model the near hemi-spherical boundary in a kettle drum in [27].

Chapter 4

Building a Drum Model

In this chapter we demonstrate a method which will allow us build complete models of musical instruments. We propose to use two and three dimensional waveguide meshes to model each constituent part of the instrument and we describe an interfacing technique which will be used to connect these together. The process is described in the context of modelling a tom-tom drum [15], and the method was first described in [3]. The work has since been extended by Laird to provide an accurate model for a kettle drum [27].

4.1 Setting up the Simple Drum Model

To demonstrate the principles behind the interfacing method, we restrict our model by representing only the interactions of the two skins and the interior air. Each skin is modelled as an ideal membrane using a triangular waveguide mesh, while the cylindrical interior column of air is modelled using, for the purposes of simplicity, a 3D square mesh. The model presented in [27] uses a dodecahedral mesh, and a full derivation of the interfacing technique, both for interfacing 2D meshes of different geometries, and meshes in different dimensions, is given.

4.1.1 Interfacing 2D and 3D Meshes at an Impedance Discontinuity

There are two problems to be faced when attempting to represent the passage of energy between the membrane and the surrounding air. Firstly, the impedance of the membrane will be different to that of the air, and secondly the densities and geometries of each mesh will be different. The first problem is easily solved since the waveguide scattering junction is equipped (by design) to connect waveguides of differing impedances. Thus we consider creating the triangular membrane mesh, not from 6-port junctions, but using 7-port junctions, 6 of which carry the membrane impedance Z_m and sit in a

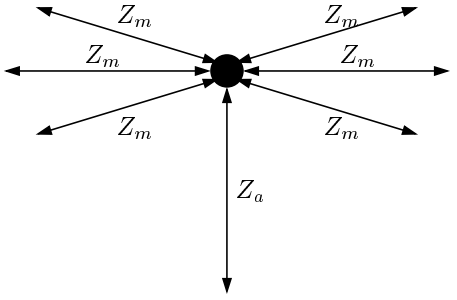

Figure 4-1: *Membrane Mesh Scattering Junction*

Mesh	f_s (Hz)	Wave Speed c ms^{-1}	$K(0)$	Δ	Number of Nodes
Membrane	11025	80.03	$\frac{1}{\sqrt{2}}$	0.01078	18.55288
Air	11025	344	$\frac{1}{\sqrt{3}}$	0.05404	3.70096

Table 4.1: *Comparison Of Model Parameters in the Drum Model.*

2D plane, and the 7th of which extends downwards or upwards towards the air mesh, and carries the air impedance Z_a. Consideration will be given to the calculation of the impedances in section 4.1.2. This scattering junction structure is shown in Figure 4-1. The other problem we encounter may be easily highlighted using a couple of quick calculations. The size of a spatial sample in a waveguide mesh may be calculated as $\Delta = K(0)cT$, where $K(0)$ is the nominal speed of wave propagation in spatial samples per sample interval, c is the true speed of wave propagation in metres per second, and $T = 1/f_s$ where f_s is the sample rate. Thus, given a drum radius of r metres, the radial number of spatial samples required may be calculated as $D = r/\Delta$. If we set the tension of the membrane to $F = 1850N/m$, the density to $\rho = 0.262kg/m^2$ and the radius as $r = 0.2m$ then differences in the required mesh parameters are summarised in Table 4.1. Clearly the membrane mesh will require many more nodes than the air mesh. A pictorial representation of this disparity is shown in Figure 4-2. Note the inclusion of the rimguides as discussed in the previous section.

The Air to Skin Interface

To create the interface from skin to air, we assume that the junction pressure at an air mesh node near the membrane is constant over an element of area $A = l_a^2$ centered over the air mesh node, where l_a is the length of a unit waveguide in the air mesh. By doing this we are approximating the incoming pressure front to the membrane by a piecewise constant function. We now use this constant pressure value to calculate output pressure values in the direction of each of the membrane nodes which are placed

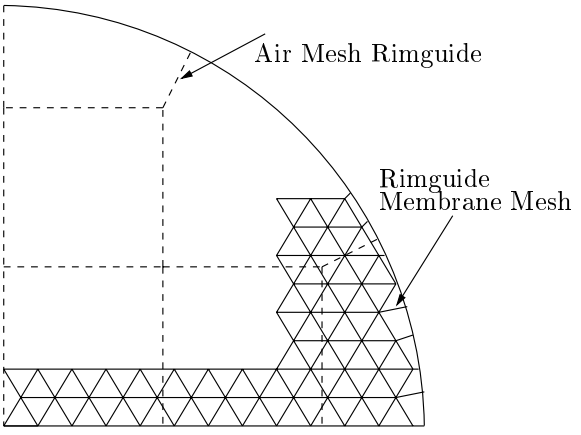

Figure 4-2: *Membrane Mesh with Underlying Air Mesh.*

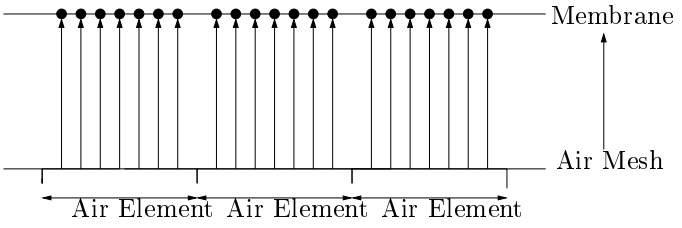

Figure 4-3: *The Air to Skin Interface.*

spatially over this air mesh node. To convert to a transverse velocity, we must divide by the air impedance Z_a [21]. Finally, since this represents pressure over an element of area A, and if there are n velocity nodes associated to this portion of the air mesh, we must scale each membrane nodes air impedance by A/n. Note that the value n is not necessarily constant for each air mesh node. We may now compute the membrane mesh junction velocity using the scattering junction equation as

$$v_j(n) = 2\left(\frac{\sum_{i=1}^{6} Z_m v_{j,i}^{+}(n) + \frac{Z_a A}{n} v_{j,a}^{+}}{6Z_m + \frac{Z_a A}{n}}\right),$$

where $v_{j,i}^{+}$ is the incoming velocity from the neighbouring membrane nodes, and $v_{j,a}^{+}$ is the incoming velocity from the air. Figure 4-3 shows a side-on view of the interface.

The Skin to Air Interface

We may now consider the interface from skin to air by referring to Figure 4-4. Since each membrane node had an input velocity from the air mesh, we can calculate the reflected velocity back in the direction of the air using equation (2.8). We may then convert these velocities into pressures by multiplying by the air impedance Z_a. Thus,

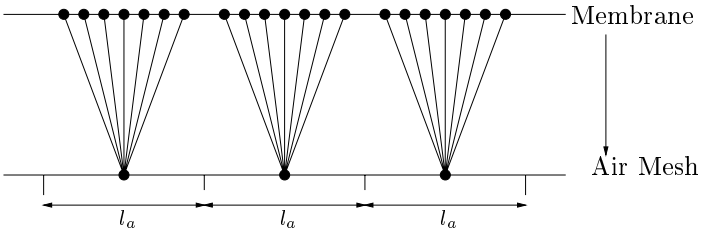

Figure 4-4: *The Skin to Air Interface.*

for each air mesh node, we must include n new inputs to replace the vertical input. To avoid an impedance discontinuity, each waveguide connecting to the membrane mesh must have an impedance Z_a/n, giving a junction pressure equation

$$p_j(n) = \frac{2}{6Z_a}\left(\sum_{i=1}^{5} Z_a p^+_{j,i}(n) + \frac{Z_a}{n}\sum_{k=1}^{n} p^+_{m,k}(n)\right), \tag{4.1}$$

where $p^+_{j,i}(n)$ are the input pressures from within the mesh, and $p^+_{m,k}(n)$ are the n input pressures from the membrane. This is entirely equivalent to taking the average of the n pressures coming from the membrane and placing the resulting value at the vertical input of the air mesh node. This can be more easily deduced by rearranging equation (4.1) as

$$p_j(n) = \frac{\sum_{i=1}^{5} p^+_{j,i}(n) + \frac{1}{n}p^+_m(n)}{3},$$

where $p^+_m(n)$ is the sum of the n inputs from the membrane. Now, each of the n inputs from the membrane are stored in memory in order to compute the reflected pressures back in the direction of the membrane. Note that the length in units of delay for each of the waveguides attaching each air mesh node to the membrane mesh is the same (this could include a fractional delay), thus the interface can be thought of in terms of Figure 4-3. Figure 4-4 however helps explain how all the connections to the membrane nodes act as the vertical input to the air mesh node.

4.1.2 Computed Membrane Impedance

The description of the proposed interface method has been based on representing the impedance discontinuity between the drum skin and the air. We discussed string impedance in section 1.3.3 where it was shown that the force and velocity waves are related via the constant $Z = \sqrt{F\rho}$. In the case of a membrane however, the impedance cannot be defined by considering the ratio of force and velocity. This is because a finite

force applied at an interior point on the membrane will result in an infinite deflection as described in Appendix A.1.2. Consequently it is necessary to describe any driving forces as being distributed over a finite area of the membrane, as opposed to being applied at a point. It has been computed in [27] that the impedance of an element in the triangular waveguide mesh is

$$Z_e = \sqrt{\frac{3}{2}}\frac{F}{f_s},$$

where F is the tension applied to the membrane, and f_s is the model sampling rate. Consequently the impedance of each waveguide within the mesh is simply

$$Z_m = \frac{R_e}{3} = \sqrt{\frac{1}{6}}\frac{F}{f_s}.$$

Finally, we also note that the area of an element of the triangular mesh is

$$A_m = \sqrt{3}\frac{c^2}{f_s^2}. \tag{4.2}$$

This choice for the impedance value is justified later when we analyse the output from the drum model.

4.2 Simulation Results

In order to assess the accuracy of the proposed interfacing technique we considered building a model for a tom-tom drum using two membrane mesh models and a 3D rectilinear mesh for the enclosed cylinder of air. For simplicity each membrane was set to have the same superficial density and be held at the same tension. We identified three criteria by which we could assess the accuracy of the model. Firstly, the interior air cavity should resonate according to its shape (and should thus exhibit resonances consistent with a cylindrical air cavity). Secondly, we considered the transmittance of energy through the air to the lower membrane, where the lower membrane should vibrate as the upper one. Finally, by modelling an interaction between skin and air, we should expect the presence of an air load. This should contribute to a lowering of the fundamental frequencies of vibration.

4.2.1 Correctly Modelling the Cylindrical Air Cavity

By forcing the velocities of each membrane mesh to zero in the drum model, we may examine the output from only the air within the drum. Each membrane acts as a pure

Mode	Modelled	Expected $r = 0.2$, $h = 0.54$	Expected $r = 0.218$, $h = 0.506$
f_{001}	340	318	340
f_{002}	674	636	680
f_{010}	961	1049	961
f_{003}	997	954	1020
f_{011}	1003	1096	1019
f_{012}	1173	1227	1177
f_{004}	1300	1272	1360

Table 4.2: *Comparison of measured and expected modes in drums air cavity.*

reflection via the interface between the membranes and the air. Thus the accuracy of the interface can be assessed. Note that the interface connections impose a distance of one waveguide between each membrane mesh and the air mesh so that the modelled height will always be greater than the desired height. In the future we could incorporate a fractional delay filter in order to correctly model this height. In the meantime we may consider our drum model when the model height is $H = 8$ waveguides. Because of the extra two spatial samples incurred during the interfacing procedure, the effective height is in fact $H = 10$ waveguides. Given a spatial sample length $\Delta = \sqrt{3}c/f_s = 0.0540431$ metres, where $f_s = 11025Hz$, the resulting drum should have height $h = 0.540431$ metres. We may thus make an analysis on the vertical modes of the cylinder of air represented by our model. Table 4.2 describes the output of such a simulation. Note that the cylindrical boundary was implemented by bounding the mesh at a radius $r = 0.2$ metres, which corresponds to a distance of $R = 3.7$ waveguides, and that the mesh was terminated by simple self-loops as described in the previous chapter. In the complete drum model we would also wish to include fractional length rimguides in order to more accurately model the circular boundary, but since in this analysis we are merely concerned with the performance of the interface at the vertical boundary, we may disregard those considerations here and concentrate mainly on the vertical mode frequencies.

In order to assess the performance of the interfacing technique, we consider only the first four vertical modes $f_{001} \ldots f_{004}$ which are listed in the left most column in Table 4.2. By comparison with the desired modes in the next column we see that the interfacing technique has caused an increase in all of the modes under observation. However, the fundamental horizontal and cylindrical mode (f_{010}) is consistent with a cylinder of radius $r = 0.218$ and height $h = 0.506$. Comparing the drum output with the expected modes of a cylinder with these dimensions, we see that a cylindrical nature is roughly preserved and there is again evidence of dispersion error. We also note that the error is larger than that found for a similar model described in Table 3.7

in section 3.3.4. This is due in part to the interface method, but also in part to the lower sample rate employed in the drum model.

Thus we conclude that with our interfacing procedure in place, we may model a cylindrical enclosure of air to a reasonable level of accuracy, and that the averaging/interpolation occurring at the boundary between the 3D and 2D meshes causes a uniform increase in the horizontal modes of vibration. From Table 4.2 we observe an accuracy of within 2.25% up to $1000Hz$. This level of accuracy could be improved by increasing the sample rate. For the piecewise constant interpolation employed in this model we should expect to halve the interpolation error when doubling the sample rate. The uniform increase in the frequencies of vibration suggest that the modelled space is too small. This could be because we have not implemented the interface near the circular boundary. We also note that since we have not included rimguides in the termination of the 3D mesh, the effective radius is too large, as was observed in chapter 3, and consequently the first circular mode is too small.

A greater level of accuracy could be achieved by implementing the model at much higher sample rates. The nature of the finite difference approximations, as described in Appendix B show how the output of the FDS will converge to the true solution as the spatial and time steps tend to zero.

4.2.2 Results from the Complete Drum model

To evaluate the overall output from the drum model we will examine measured outputs from each of the skins, and from the interior of the drum (something that is easy to do in a simulation, but perhaps harder to do in reality). First we recall the output from a simple membrane in vacuo as shown in the plots of Figure 4-5, where the left hand plot is for a membrane struck at its centre and the right hand plot represents the output of a membrane struck off centre. We chose to model a membrane of radius $r = 0.2$ metres, density $\sigma = 0.262kg/m^2$ and held at a tension $F = 1850N/m$. We discussed membrane simulations in chapter 2 where we concluded that the inclusion of rimguides would improve the quality of the simulation, and that errors in the positions of the modes were consistent with the dispersion error. Using these parameters the fundamental frequency should be $f_{01} = 160.8Hz$.

The left hand plot of Figure 4-6 shows the output of the drum model as measured as an average of all the velocities on the top skin, while the right hand plot measures the bottom skin. The drum depth has been set at approximately $h = 0.5m$. We say approximately in view of the discussion in the previous section, where we saw that setting the drum height to 8 waveguides effectively gave cylindrical mode frequencies consistent with a cylinder of height $h = 0.506m$. First of all we observe that each

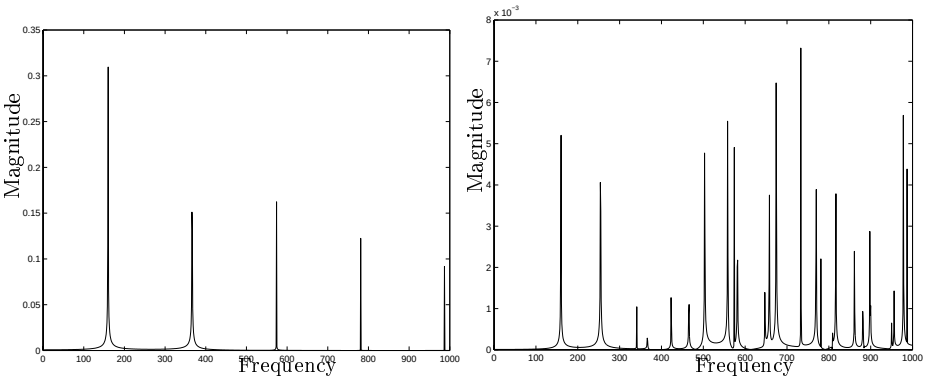

Figure 4-5: *Membranes Struck at Centre and Off Centre.*

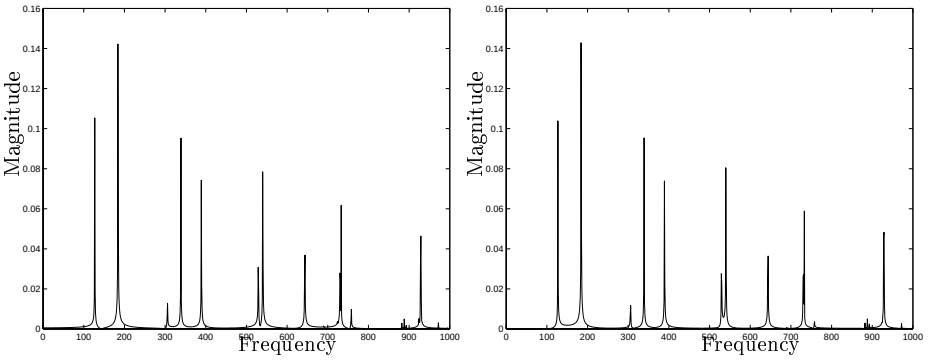

Figure 4-6: *(a) Drum model output measured from top skin. (b) Drum model output measured from Bottom skin.*

plot is almost identical, thus the air is transmitting the vibrations of each skin to its counterpart at the opposite end of the drum. Secondly we regard the properties of the output. We note that there is a sequence of strong peaks which we can identify with the resonant modes of the membrane, but that the fundamental frequency has dropped, and subsequent modes are also lower. This is consistent with the expected behaviour due to the air load and we discuss this in more depth later. We could expect this phenomena to be even more noticeable were we to model the surrounding air around the drum as well [15], however we leave that to further study. We also note the inclusion of new modes of vibration. In fact the distribution of frequencies is much more consistent with that of a membrane excited in all its modes of vibration, not just its central modes as shown in the right-hand plot of Figure 4-5. Thus we conclude that the inclusion of the resonating chamber has caused other modes of vibration near the central modes to be excited also.

	Membrane		Drum (One Skin)		Drum (Two Skins)	
Mode (mn)	f_{mn}	f_{mn}/f_{11}	f_{mn}	f_{mn}/f_{11}	f_{mn}	f_{mn}/f_{11}
01	160	0.63	151	0.75	108	0.55
11	254	1.00	199	1.00	198	1.00
21	341	1.34	285	1.43	286	1.44
02	366	1.44	356	1.79	317	1.60
31	423	1.67	376	1.89	356	1.70
12	466	1.84	388	1.95	387	1.96
41	503	1.98	423	2.13	410	2.07

Table 4.3: *Output from the Drum Model*

4.2.3 Modelling the Air Load

We briefly discussed the effect of an air load on a membrane in the previous section and now consider this property in more detail. In general the presence of an air load will effectively raise the density of the membrane, and hence lower the frequencies of vibration. This phenomenon is typically frequency dependent, and the lower frequencies are affected more. If the air is confined in some way, such as by the kettle in a tympani drum, or by the shell and lower skin of a tom-tom drum, then we should expect a rise in the axisymmetric modes, in particluar the (01) mode [15].

We discuss the output of our model with respect to this desired behaviour, and also by comparing to measured output in [15]. Table 4.3 describes the output of our tom-tom drum model in terms of mode frequencies and the sequence of ratios of the mode frequencies. We considered two simulations, one where both skins were allowed to vibrate, and one where the lower skin was held at zero to act as a rigid termination. The second of these simulations allowed us to examine the effect of an enclosed air load. Shown in Table 4.4 are measured output from experiments reported in [15]. They describe the pattern of mode frequencies measured from a membrane with and without a tympani kettle attached. We note that these measurements also include the effect of the external air load, contrary to our model which represents only the interior air.

Beginning with the drum model where one skin is held rigid, we see, from Table 4.3, a lowering of all the mode frequencies and a reordering of the partials. The ratio of the fundamental mode, the (11) mode for membranes, to the other frequencies is raised. This is similar to the general behaviour encountered for the membrane with kettle, as described in Table 4.4. Now, examining the output of the drum model with two skins, we find a greater lowering of the mode frequencies than the case with only one skin, although the fundamentals are almost identical. The ratio $f_{11} : f_{01}$ is lower than the one skin case, as are the ratios $f_{11} : f_{02}$, $f_{11} : f_{31}$, $f_{11} : f_{22}$ and $f_{11} : f_{41}$. This difference

	With Kettle		Without Kettle	
Mode (mn)	f_{mn}	f_{mn}/f_{11}	f_{mn}	f_{mn}/f_{11}
01	140	0.81	92	0.54
11	172	1.00	173	1.00
21	258	1.50	253	1.47
02	284	1.65	266	1.54
31	340	1.97	330	1.91
12	344	2.00	365	2.12
41	420	2.44	408	2.36

Table 4.4: *Measured output from Real Drums*

in the ratios is similar to that found when comparing the membrane with kettle to the membrane without. In particular, note that including a second skin has lowered the ratio $f_{11} : f_{01}$ quite significantly, as has removing the kettle, while in both cases the ratio $f_{11} : f_{12}$ has been raised.

It is interesting to note how the presense of the air load in a tympani drum serves to convey a sense of pitch in the output sound. In Table 4.4 the ratios of the frequencies $1.00 : 1.50 : 1.97 : 2.44$ is nearly harmonic. An investigation into this introduction of harmonicity could be an interesting experiment using the drum model for the future.

4.3 Conclusion and Discussion

In this chapter we have described a technique by which we may interface a 2D and 3D waveguide mesh and applied the method in a model for a tom-tom drum. We observed a behaviour qualitatively similar to the expected by considering the transmission of pressure waves from top skin to bottom skin and the interior resonances. The model was implemented at quite a low sample rate ($f_s = 11025Hz$) and much improved accuracy could be achieved by increasing the sampling resolution. We went on to show that the model seemed to be representing air loading on the membrane. We compared the model with measured output from an air loaded membrane and tympani drum, and saw a qualitative similarity. The results are certianly encouraging, and seem to show that the interface method can be used to model air loading and indeed be used to design drum models. Differences between our model and measured output could be due to simplifications in the model. We have included only the interface between the membranes and the interior air, plus we neglected other effects such as dispersion and internal damping of the membrane. Furthermore, each of the membranes in the drum model will suffer from dispersion error. Consequently we have only been able to provide a qualitative comparison between modelled and measured outputs. A more accurate

tympani drum model has been designed using digital waveguide meshes connected with the interface technique described here [27]. In this study the model was compared to a Finite Element Method (FEM) model and was shown to perform reasonably well.

Chapter 5

1D Models Including Material Properties

The models presented so far have been shown to work well for ideal wave propagation in 1D and 2D. We have also shown that simple musical instrument models can be constructed using simple waveguide meshes. However, real instruments vibrate in a much more complicated manner where material properties such as stiffness are important. Examples include the vibrating bars in xylophones or thick stiff strings in pianos. We have already observed in our model for a drum in chapter 4 that the sequence of resonant frequencies was heavily affected by the stiffness of the drum skin, which for a tom-tom drum was prevalent since the skins are typically thicker than those found in tympanis. In general stiffness causes a non-constant speed of wave propagation, with the higher frequencies travelling faster, and this causes a spreading out of the higher mode frequencies.

It has been theorised that stiffness may be simulated using allpass filter banks placed at the reflection of a digital waveguide [6, 37, 48, 53]. Such an approach uses the non-linear phase property of the allpass filter (Appendix C.2.1) in order to alter the wave speed characteristics, essentially speeding up the higher frequencies. It has been shown that this provides a reasonable simulation for stiff strings however, the model has little physical significance and the filter coefficients must be statistically matched to the expected phase response of the true system. Furthermore the method could not be extended to model stiff bars where the DC wave speed will be zero.

In this chapter we describe and discuss some explicit waveguide models for vibrating bars and stiff strings which represent numerical simulations of the stiff bar and stiff string PDEs described in Appendix A.2. The models are formed by using coupled *interleaved* waveguide models for two-variable systems which are equivalent to the

governing equations. The methods described here were originally proposed in [8] and extended in [1, 2].

5.1 Interleaved Digital Waveguides

In order to design waveguide models for the more complicated systems describing the stiff bar or plate, we consider a new waveguide formulation called an *interleaved* waveguide. Such a structure is useful since it makes use of two separate wave variables. In the case of the ideal string, we define the transverse velocity by $v = \frac{\partial u}{\partial t}$, and define a force term $i = -F\frac{\partial u}{\partial x}$, where F is string tension. Note how the force term is proportional to string slope, with tension as the proportionality constant. Such a definition is intuitive when we think of the derivation of the 1D wave equation in Appendix A.1.1. Thus we may decouple the 1D wave equation into a system of PDEs

$$\begin{aligned} \frac{\partial v}{\partial t} &= -\frac{1}{\rho}\frac{\partial i}{\partial x} \\ \frac{\partial i}{\partial t} &= -F\frac{\partial v}{\partial x}. \end{aligned} \tag{5.1}$$

This alternative approach to representing the wave equation was presented in [8] where it is presented in its equivalent form as a special case of the transmission line equations [12]. In this instance the two variables are voltage u and current i,

$$\begin{aligned} l\frac{\partial i}{\partial t} + \frac{\partial u}{\partial x} + ri + e &= 0, \\ c\frac{\partial u}{\partial t} + \frac{\partial i}{\partial x} + gu + h &= 0. \end{aligned} \tag{5.2}$$

The special case where $r = e = g = h = 0$, and l and c are constant, reduces to the standard 1D wave equation

$$\left.\begin{aligned} l\tfrac{\partial i}{\partial t} + \tfrac{\partial u}{\partial x} &= 0 \\ c\tfrac{\partial u}{\partial t} + \tfrac{\partial i}{\partial x} &= 0 \end{aligned}\right\} \Rightarrow \frac{\partial^2 u}{\partial t^2} = \frac{1}{lc}\frac{\partial^2 u}{\partial x^2}. \tag{5.3}$$

Thus we may identify velocity as a voltage like variable, while force may be consider a current like variable.

Now, the interleaved waveguide which models the system of equation (5.1) must be

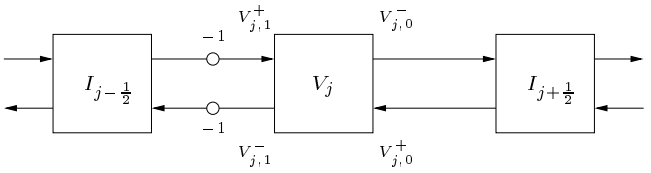

Figure 5-1: *Interleaved Waveguide.*

equivalent to the centered FDS

$$\begin{aligned} I_{j+\frac{1}{2}}(n+\frac{1}{2}) - I_{j+\frac{1}{2}}(n-\frac{1}{2}) &= -\lambda F\left(V_{j+1}(n) - V_j(n)\right), \\ V_j(n) - V_j(n-1) &= -\lambda\frac{1}{\rho}\left(I_{j+\frac{1}{2}}(n-\frac{1}{2}) - I_{j-\frac{1}{2}}(n-\frac{1}{2})\right), \end{aligned} \tag{5.4}$$

where $\lambda = T/\Delta$.

The corresponding interleaved waveguide is constructed by splitting each unit of delay between junctions on a standard 1D waveguide into two half units of delay within which we place a series junction and add a sign inversion as shown in Figure 5-1. This gives a construction including extra junctions at which junction force may be computed. We recall from chapter 2 that velocity and force travelling waves are related as follows

$$\begin{aligned} V^+ = ZI^+ \quad &\Rightarrow \quad I^+ = YV^+ \\ V^- = -ZI^- \quad &\Rightarrow \quad I^- = -YV^-, \end{aligned} \tag{5.5}$$

where Z is the impedance of the delay line, with admittance $Y = 1/Z$, and where as usual a superscript $+$ denotes an incoming wave to a scattering junction, with a $-$ denoting an outgoing wave.

Just as was the case in previous chapters, we may derive a relationship between incoming velocity or force waves at a particular junction in terms of output waves at neighbouring junctions. For velocity waves the relationship is simple,

$$\begin{aligned} V^+_{j,0}(n) &= V^-_{j+\frac{1}{2},1}(n-\frac{1}{2}), \\ V^- + j,1(n) &= V^-_{j-\frac{1}{2},0}(n-\frac{1}{2}). \end{aligned} \tag{5.6}$$

while for force waves

$$\begin{aligned} I^+_{j,0}(n) &= YV^+_{j,0}(n) \\ &= YV^-_{j+\frac{1}{2},1}(n-\frac{1}{2}) \\ &= -I^-_{j+\frac{1}{2},1}(n-\frac{1}{2}) \end{aligned} \tag{5.7}$$

and similarly

$$I^+_{j,1}(n) = -I^-_{j-\frac{1}{2},0}(n-\frac{1}{2}). \tag{5.8}$$

Thus we observe that force waves travel with a sign inversion.

Referring to Figure 5-1 we use equations (5.5), (5.6), (5.7) and (5.8) to manipulate the junction velocity equation,

$$\begin{aligned} V_j(n) &= V^+_{j,0}(n) + V^+_{j,1}(n) \\ &= Z\left(I^+_{j,0}(n) + I^+_{j,1}(n)\right) \\ &= -Z\left(I^-_{j+\frac{1}{2},1}(n-\frac{1}{2}) - I^-_{j-\frac{1}{2},0}(n-\frac{1}{2})\right) \\ &= -Z\left(I_{j+\frac{1}{2}}(n-\frac{1}{2}) - I_{j-\frac{1}{2}}(n\frac{1}{2})\right) \\ &+ Z\left(I^+_{j+\frac{1}{2},1}(n-\frac{1}{2}) - I^+_{j-\frac{1}{2},0}(n-\frac{1}{2})\right) \\ &= -Z\left(I_{j+\frac{1}{2}}(n-\frac{1}{2}) - I_{j-\frac{1}{2}}(n-\frac{1}{2})\right) \\ &+ V^-_{j,0}(n-1) + V^-_{j,1}(n-1) \\ &= -Z\left(I_{j+\frac{1}{2}}(n-\frac{1}{2}) - I_{j-\frac{1}{2}}(n-\frac{1}{2})\right) + V_j(n-1), \end{aligned} \tag{5.9}$$

which is equivalent to the second of the expressions in equation (5.4) when we set $Z = \frac{\lambda}{\rho}$. Similarly we may begin from a series junction representing junction force to get

$$I_{j+\frac{1}{2}}(n+\frac{1}{2}) = -\frac{1}{Z}\left(V_{j+1}(n) - V_j(n)\right) - I_{j+\frac{1}{2}}(n-\frac{1}{2}), \tag{5.10}$$

where we require $Z = \frac{1}{\lambda F}$ for equivalence with equation (5.4). Consequently we may choose $Z = \sqrt{F\rho}$, giving $\lambda = \sqrt{\frac{F}{\rho}}$. Note that this is exactly as was the case in the original waveguide formulation. Furthermore, since the impedances and admittances of each waveguide are the same, the extra series junction becomes merely a 'through' with

a sign-inversion [7], and that the impedances at the velocity junctions are arbitrary and we reduce once again to the standard waveguide. However this formulation is useful in the case of spatially varying parameters, and will also form the basis of our discussions on modelling more difficult systems.

5.2 A Digital Waveguide Model for the Euler-Bernoulli Beam

In this section we describe a digital waveguide network which models the Euler-Bernoulli formulation for an ideal bar as described in Appendix A.2. In this thesis we restrict ourselves to a detailed treatise on this formulation as opposed to the more accurate formulations of either Rayleigh or Timoshenko [20]. We do this for two reasons. Firstly, as was the case when formulating the drum model in the previous chapter, we wish to retain a certain level of simplicity. This makes the physical comparisons clearer, making it is easier to see how these individual models fit into the larger framework we are developing, and making the visualisation of extensions to two dimensions, plus inclusion into complete instrument models, a little more straightforward and intuitive. Secondly, it has been remarked that the simplified theory is valid, to a first degree of approximation, in the low frequency range, when compared to measurements on real instruments [11].

The model we assess and describe was first presented in March 2001 by Stefan Bilbao [8]. In this section we describe the model and its physical significance (that is, how it could be designed using a little intuition). We show that the model is equivalent to a FDS for the underlying PDE and we examine its accuracy by comparing its dispersion characteristics with that of a real bar, and examine the frequency spectrum of its output. What we present here is a slightly simplified version which does not account for any spatial variation in parameters. Hence the PDE we consider, as described in Appendix A.2, is

$$\frac{\partial^2 u}{\partial t^2} = -\frac{EI}{\rho A}\frac{\partial^4 u}{\partial x^4}, \tag{5.11}$$

where ρ is the materials density, E its Young's Modulus, and I the moment of gyration about the beam's perpendicular axis. If we were to consider spatial variation of the parameters, the equation would be

$$\rho A\frac{\partial^2 u}{\partial t^2} = -\frac{\partial}{\partial x^2}\left(EI\frac{\partial^2 u}{\partial x^2}\right),$$

where now EI and ρA are both functions of position.

Consider now approaching the problem by decoupling equation (5.11) into a two variable system. The is done by writing the velocity as $v = \frac{\partial u}{\partial t}$ as before, and this time we take the force to be $m = EI\frac{\partial^2 u}{\partial x^2}$. We note that since there is no tension, and that the restoring force is proportional to how much the bar is bent, the force term in this case is related to the bar's curvature. The de-coupled equation is

$$\begin{aligned} \frac{\partial v}{\partial t} &= -\frac{1}{\rho A}\frac{\partial^2 m}{\partial x^2} \\ \frac{\partial m}{\partial t} &= EI\frac{\partial^2 v}{\partial x^2}. \end{aligned}$$

By applying centered differences to these equations we arrive at the following difference scheme,

$$\begin{aligned} V_j(n+1) - V_j(n) &= -\frac{\mu}{\rho A}\left[M_{i+1}(n+\frac{1}{2}) - 2M_i(n+\frac{1}{2}) + M_{i-1}(n+\frac{1}{2})\right] \\ M_i(n+\frac{1}{2}) - M_i(n-\frac{1}{2}) &= \mu EI\left[V_{i+1}(n) - 2V_i(n) + V_{i-1}(n)\right], \end{aligned} \tag{5.12}$$

where we define $\mu = \frac{T}{\Delta^2}$ for time step $T = \frac{1}{f_s}$ and spatial step Δ, and where f_s is the sample rate of the simulation.

Shown in Figure 5-2 is a diagram of the proposed digital waveguide model for the Euler-Bernoulli bar. The model is comprised of two coupled interleaved waveguides arranged so as to allow measurement of each of the wave variables at every spatial step. In the framework of transmission line modelling, we may think of the variable V as being voltage-like, while M can be thought of as being current-like. Notice how the form of the coupling means that at any junction where we calculate M we are intuitively approximating $V_{j+1}(n) - 2V_j(n) + V_{j-1}(n)$, which is of course a finite difference approximation to the curvature. Furthermore, note that this diagram differs from that in [8] since we have simplified our model to deal only with bars of spatially uniform material parameters. To include spatially varying parameters we may attach self-loops to each junction. We shall see later on how these self loops can be used to alter the dispersion characteristics of any waveguide model. The form of the FDS in equation (5.12) also indicates why we take half time steps between junctions, and why we require access to both variables at each spatial step.

Recalling the rules of propagation for the alternate wave variables from the previous section we now prove the equivalence of the waveguide structure in Figure 5-2 to the FDS in equation (5.12). We indicate incoming and outgoing velocities to the velocity junctions by $V^+_{j,0}(n), \ldots, V^+_{j,3}(n)$ and $V^-_{j,0}(n), \ldots, V^-_{j,3}(n)$ respectively. The velocities

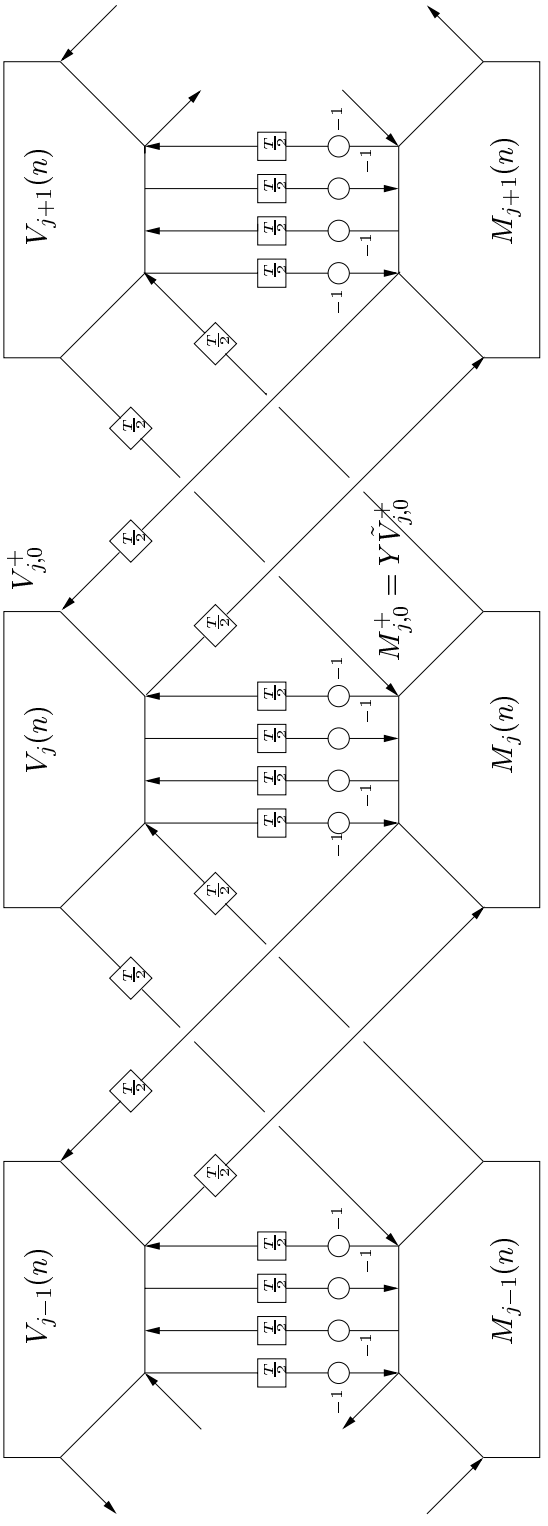

Figure 5-2: *Digital Waveguide Network for the Euler-Bernoulli Bar*

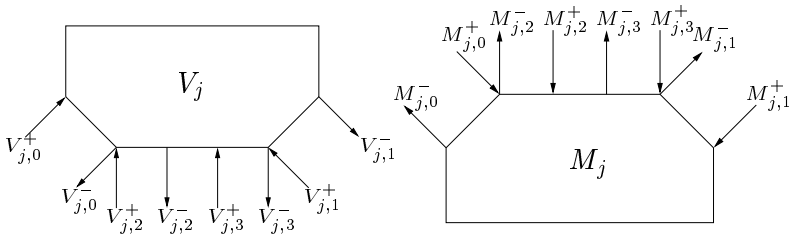

Figure 5-3: *Junction structure and input parameters*

impinge upon the junction with impedance Y. Similarly, incoming and outgoing velocities to the force junctions are written as $\tilde{V}^+_{j,0}(n), \ldots, \tilde{V}^+_{j,3}(n)$ and $\tilde{V}^-_{j,0}(n), \ldots, \tilde{V}^-_{j,3}(n)$ respectively, where $\tilde{V}^+_{j,i}(n) = ZM^+_{j,i}(n)$, $\tilde{V}^-_{j,i}(n) = -ZM^-_{j,i}(n)$ and $Z = 1/Y$, according to the rules for force and velocity waves discussed in section 5.1. Beginning at a force junction, we may write the total force M_j at junction j as

$$\begin{aligned} M_j(n+\frac{1}{2}) &= \frac{2}{Z_j}\left[ZM^+_{j,0}(n+\frac{1}{2}) + ZM^+_{j,1}(n+\frac{1}{2}) + ZM^+_{j,2}(n+\frac{1}{2}) + ZM^+_{j,3}(n+\frac{1}{2})\right] \\ &= \frac{2}{Z_j}\left[\tilde{V}^+_{j,0}(n+\frac{1}{2}) + \tilde{V}^+_{j,1}(n+\frac{1}{2}) + \tilde{V}^+_{j,2}(n+\frac{1}{2}) + \tilde{V}^+_{j,3}(n+\frac{1}{2})\right], \end{aligned}$$

where $Z_j = 4Z$ is the total junction admittance. Notice that we choose not to cancel Z in the junction scattering equation above. Now, by using the now standard technique, we write inputs to the current junction as outputs from adjacent junctions at the previous time step. By doing this we are able to write the total force M_j at junction j in terms of velocities and forces of other junctions at other time steps.

$$\begin{aligned} M_j(n+\frac{1}{2}) &= \frac{2}{Z_j}\left[V^-_{j-1,1}(n) + V^-_{j+1,0}(n) - V^-_{j,2}(n) - V^-_{j,3}(n)\right] \\ &= \frac{2}{Z_j}\left[V_{j-1}(n) + V_{j+1}(n) - 2V_j(n)\right] \\ &\quad - \frac{2}{Z_j}\left[V^+_{j-1,1}(n) + V^+_{j+1,0}(n) - V^+_{j,2}(n) - V^+_{j,3}(n)\right] \\ &= \frac{2}{Z_j}\left[V_{j-1}(n) + V_{j+1}(n) - 2V_j(n)\right] \\ &\quad - \frac{2}{Z_j}\left[\tilde{V}^-_{j,0}(n-\frac{1}{2}) + \tilde{V}^-_{j,1}(n-\frac{1}{2}) + \tilde{V}^-_{j,2}(n-\frac{1}{2}) + \tilde{V}^+_{j,3}(n-\frac{1}{2})\right] \\ &= \frac{2}{Z_j}\left[V_{j-1}(n) + V_{j+1}(n) - 2V_j(n)\right] \\ &\quad - \frac{2}{Z_j}\left[ZM^-_{j,0}(n-\frac{1}{2}) + ZM^-_{j,1}(n-\frac{1}{2}) + ZM^-_{j,2}(n-\frac{1}{2}) + ZM^+_{j,3}(n-\frac{1}{2})\right] \\ &= \frac{2}{Z_j}\left[V_{j-1}(n) + V_{j+1}(n) - 2V_j(n)\right] + M_j(n-\frac{1}{2}). \end{aligned} \tag{5.13}$$

Now this difference equation is identical to that of equation (5.12) if we set

$$Z_j = \frac{2}{EI\mu}.$$

Similarly we may begin with a velocity junction as follows, where total junction impedance is $Y_j = 4Y$ and again we choose not to cancel,

$$\begin{aligned}
V_j(n+1) &= \frac{2}{Y_j}\Big[YV^+_{j,0}(n+1) + YV^+_{j,1}(n+1) + YV^+_{j,2}(n+1) + YV^+_{j,3}(n+1)\Big] \\
&= \frac{2}{Y_j}\Big[Y\tilde{V}^-_{j-1,1}(n+\tfrac{1}{2}) + Y\tilde{V}^-_{j+1,0}(n+\tfrac{1}{2}) - Y\tilde{V}^-_{j,2}(n+\tfrac{1}{2}) - Y\tilde{V}^-_{j,3}(n+\tfrac{1}{2})\Big] \\
&= \frac{2}{Y_j}\Big[-M^-_{j-1,1}(n+\tfrac{1}{2}) - M^-_{j+1,0}(n+\tfrac{1}{2}) + M^-_{j,2}(n+\tfrac{1}{2}) + M^-_{j,3}(n+\tfrac{1}{2})\Big] \\
&= \frac{2}{Y_j}\Big[-M_{j-1}(n+\tfrac{1}{2}) - M_{j+1}(n+\tfrac{1}{2}) + 2M_j(n+\tfrac{1}{2})\Big] \\
&\quad - \frac{2}{Y_j}\Big[-M^+_{j-1,1}(n+\tfrac{1}{2}) - M^+_{j+1,0}(n+\tfrac{1}{2}) + M^+_{j,2}(n+\tfrac{1}{2}) + M^+_{j,3}(n+\tfrac{1}{2})\Big] \\
&= -\frac{2}{Y_j}\Big[M_{j-1}(n+\tfrac{1}{2}) - 2M_j(n+\tfrac{1}{2}) + M_{j+1}(n+\tfrac{1}{2})\Big] \\
&\quad - \frac{2}{Y_j}\Big[-Y\tilde{V}^+_{j-1,1}(n+\tfrac{1}{2}) - Y\tilde{V}^+_{j+1,0}(n+\tfrac{1}{2}) + Y\tilde{V}^+_{j,2}(n+\tfrac{1}{2}) + Y\tilde{V}^+_{j,3}(n+\tfrac{1}{2})\Big] \\
&= -\frac{2}{Y_j}\Big[M_{j-1}(n+\tfrac{1}{2}) - 2M_j(n+\tfrac{1}{2}) + M_{j+1}(n+\tfrac{1}{2})\Big] \\
&\quad - \frac{2}{Y_j}\Big[-YV^-_{j,0}(n) - YV^-_{j,1}(n) - YV^-_{j,2}(n) - YV^-_{j,3}(n)\Big] \\
&= -\frac{2}{Y_j}\Big[M_{j-1}(n+\tfrac{1}{2}) - 2M_j(n+\tfrac{1}{2}) + M_{j+1}(n+\tfrac{1}{2})\Big] \\
&\quad + V_j(n), \qquad (5.14)
\end{aligned}$$

which is clearly equivalent to the FDS of equation (5.12) by putting the total junction impedance

$$Y_j = \frac{2\rho A}{\mu}.$$

The two equivalence equations are clearly satisfied when we set

$$\mu = \frac{1}{2}\sqrt{\frac{\rho A}{EI}},$$

with $Y = \sqrt{\rho AEI}$. In his thesis Stefan Bilbao carefully describes the choice of

impedance values for each input to each series or parallel junction when the material parameters vary spatially [8]. What we have given here is a generalisation for constant material values.

5.2.1 Evaluating Dispersion in the Bar Model

Before moving on to a simulation, we discuss expected performance of the model by considering aspects of the spectral amplification factor for the underlying FDS. This FDS may be written as

$$\begin{aligned} &V_j(n+1) - 2V_j(n) + V_j(n-1) \\ &\quad = -b^2\mu^2\left[V_{j+2}(n) - 4V_{j+1}(n) + 6V_j(n) - 4V_{j-1}(n) + V_{j-2}(n)\right], \end{aligned}$$

where $b^2 = \frac{EI}{\rho A}$ and $\mu^2 = \frac{T^2}{\Delta^4}$. Then stability can be assessed by considering the spectral amplification factor $g(w)$, which is found by solving the following equation.

$$g^2 + \left(16b^2\mu^2\sin^4(w/2) - 2\right)g + 1 = 0.$$

Now, writing $B = 16b^2\mu^2\sin^4(w/2) - 2$, we see that the amplification factor g is always complex when $B^2 - 4 < 0$, that is when $\mu \leq \frac{1}{2}\sqrt{\frac{\rho A}{EI}}$. This is also the stability condition in our model. Thus the amplification factor can be written as

$$g(w) = -\frac{B}{2} \pm i\frac{\sqrt{4 - B^2}}{2}.$$

Given the amplification factor we may examine the accuracy of the scheme by noting that $g(w)$ has unit magnitude. Thus the scheme is lossless and any deviation from the true solution will be caused by a phase error. The phase of the amplification factor can be used to calculate the speed of wave propagation in the bar model, as was done in chapters 2 and 3. This time the wave speed will be frequency dependent and a comparison of the modelled wave speed with the desired wave speed as calculated in Appendix A.2.2 is shown in Figure 5-4. We notice a qualitative similarity between the modelled wave speed (right hand plot) and the desired wave speed, but wave speeds in the modelled system are systematically too low. To evaluate this deviation more directly, and to examine how changes in the sampling resolution affect the accuracy, we consider the relative phase [34]. This is calculated as the ratio of the phase of the FDS to that of the true system, that is,

$$K(w) = \frac{arg\{g(w)\}}{bTk^2},$$

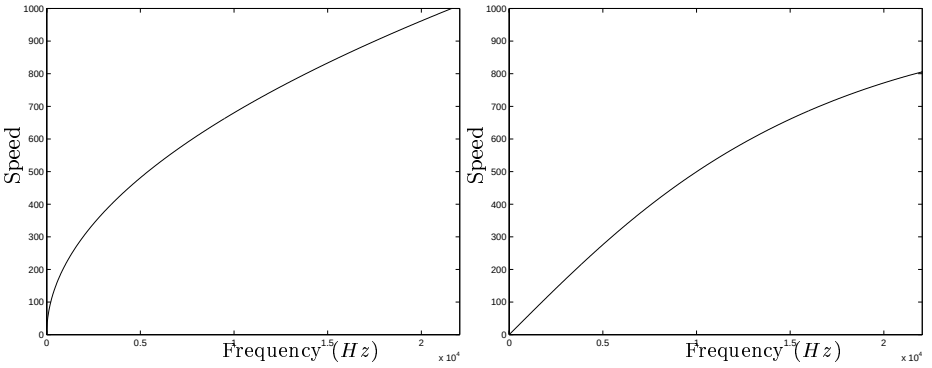

Figure 5-4: *Comparison of Modelled and True Wave Speeds for the Bar Model.*

where, as described in [34], $w = k\Delta$ and

$$arg\{g(w)\} = \tan^{-1}\left(\frac{\sqrt{4-B^2}}{-B}\right).$$

Resolving the identity for w gives

$$\begin{aligned} K(w) &= \frac{arg\{g(w)\}}{b\frac{T}{\Delta^2}w^2} \\ &= \frac{1}{b\mu}\frac{arg\{g(w)\}}{w^2}. \end{aligned} \tag{5.15}$$

It is worth noting that this quantity is identical to the relative dispersion (or relative wave speed). In order to calculate dispersion from phase we divide by frequency w, as was done in chapters 2 and 3. Thus to calculate relative dispersion we would have to divide both the numerator and denominator of the above expression by w. Thus the relative phase is a quantity which describes the deviation of the modelled wave speed from the desired wave speed and where the ideal model would have $K(w) = 1$ for all frequencies. In essence we computed the same property previously for non stiff media, since in those cases the ideal wave speed was a constant.

Shown in Figure 5-5 are some relative phase plots (or equally, relative dispersion) plots (in Hz) for the bar model for various values of the sample rate f_s. We see that in all cases the accuracy is best over the low frequency range, and that deviation from the ideal relative phase increases with increasing frequency. Furthermore we note that, as expected, increasing the sample rate will improve the quality of the simulation. Since the FDS to which the waveguide model is equivalent uses centred differences to approximate the derivatives, the scheme will converge to the true solution as the sample rate increases. This means that with an arbitrarily large sampling resolution we could

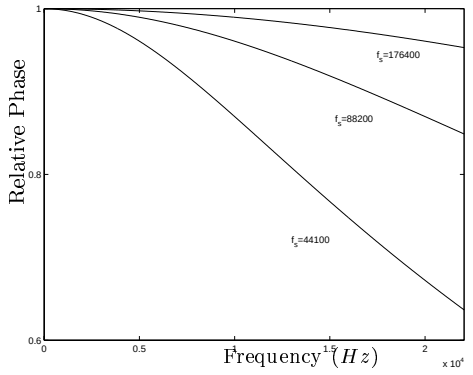

Figure 5-5: *Relative Phase Plots for the Bar Model.*

make the two curves in Figure 5-4 identical.

Changes in the simulation parameters cause only a change in the stability condition, and hence a change in μ, that is, the relationship between between the spatial step size and the time step. For example, if we were to consider increasing the stiffness E, then to maintain the same spatial resolution Δ, would mean increasing the sample rate f_s, since at the lower limit of stability we have $\mu = \frac{1}{2}\sqrt{\frac{\rho A}{EI}}$, that is, $T = \frac{1}{2}\sqrt{\frac{\rho A}{EI}}\Delta^2$. Hence increasing E would result in a decrease in the time step T. Thus for highly stiff systems in order to maintain stability we should expect to need quite high sample rates. Similarly when we require a low spatial resolution we will also require high sample rates. A FDS for a bar has been presented in [11]. In this paper they reduce the spatial step size as low as $\Delta = 0.53mm$ in order to observe convergence to within 0.5% in the output of the scheme. Such a spatial step size in our model would result in a sample rate of approximately $f_s = 50MHz$, and this is similar to the resolution adhered to in their paper.

5.2.2 Boundary Conditions

We consider the application of three common boundary types found in the literature: simply supported, clamped or free. The inclusion of these boundary conditions in our waveguide model is quite straightforward. Theoretical prediction of the modes of vibration is based on the boundary type and is discussed in Appendix A.2.

The simplest case is of a *simply supported* edge, where the bar is fixed, but allowed to pivot. In this case we set both the velocity and the bending moment at the boundary to zero so that for a simply supported edge at $x = 0$ we require to satisfy $v(0,t) = m(0,t) = 0$. This may be achieved quite simply by putting the outermost junctions $V_0(n) = 0$ and $M_0(n) = 0$ for every n. Since energy only enters the edge junctions from within the waveguide, each of these may be left as a one-port junction, and

consequently each acts so as to send an inverted signal back. Formally for a simply supported velocity junction at $j = 0$, we will have $V^-_{0,1}(n) = -V^+_{0,1}(n)$, while for a force junction at $j = 0$, $M^-_{0,1}(n) = -M^+_{0,1}(n)$. Note that we may resolve velocity waves at the simply supported termination for the M junction so that

$$\tilde{V}^-_{0,1}(n) = -ZM^-_{0,1}(n) = ZM^+_{0,1}(n) = \tilde{V}^+_{0,1}(n).$$

This shows that velocity waves invert at a velocity junction which is set to zero, while they do not invert at a force junction.

For a *clamped* boundary we require $v(0,t) = 0$ and $\frac{\partial v}{\partial x}(0,t) = 0$. The first of these conditions is implemented for the velocity junction as above for the simply supported edge. For the force junction at $j = 0$, using the FDS we see that we have,

$$M_0(n + \frac{1}{2}) - M_0(n - \frac{1}{2}) = \mu EI\left[V_1(n) - 2V_0(n) + V_{-1}(n)\right],$$

given that we had access to $V_{-1}(n)$. Setting $V_1(n) = V_{-1}(n)$ gives a second order accurate approximation to $\frac{\partial v}{\partial x}(0,t) = 0$ and results in

$$M_0(n + \frac{1}{2}) - M_0(n - \frac{1}{2}) = 2\mu EIV_1(n),$$

since $V_0(n) = 0$. Thus our digital waveguide must match this finite difference at the boundary. To do this we make our junction M_0 a two port junction consisting of a self-loop of one unit of delay and a sign inversion and a connection to V_1 as shown in the left-hand plot of Figure 5-6. The impedance of each of these ports is set to $Z = 1/Y = 1/\sqrt{\rho AEI}$. Then,

$$\begin{aligned}
M_0(n + \frac{1}{2}) &= \frac{1}{Z_j}\left[\tilde{V}^+_{0,0}(n + \frac{1}{2}) + \tilde{V}^+_{0,1}(n + \frac{1}{2})\right] \\
&= \frac{1}{Z_j}\left[V^-_{1,1}(n) - \tilde{V}^-_{0,1}(n - \frac{1}{2})\right] \\
&= \frac{1}{Z_j}V_1(n) - \frac{1}{Z_j}\left[V^+_{1,1}(n) + \tilde{V}^-_{0,1}(n - \frac{1}{2})\right] \\
&= \frac{1}{Z_j}V_1(n) - \frac{1}{Z_j}\left[\tilde{V}^-_{0,0}(n - \frac{1}{2}) + \tilde{V}^-_{0,1}(n - \frac{1}{2})\right] \\
&= \frac{1}{Z_j}V_1(n) + M_0(n - \frac{1}{2}),
\end{aligned}$$

where $1/Z_j = \sqrt{\rho AEI} = 2\mu EI$ as required.

Finally, for a *free* end we require $m(0,t) = 0$ and $\frac{\partial m}{\partial x}(0,t) = 0$. The first of these conditions can be implemented as with the simply supported edge. The second

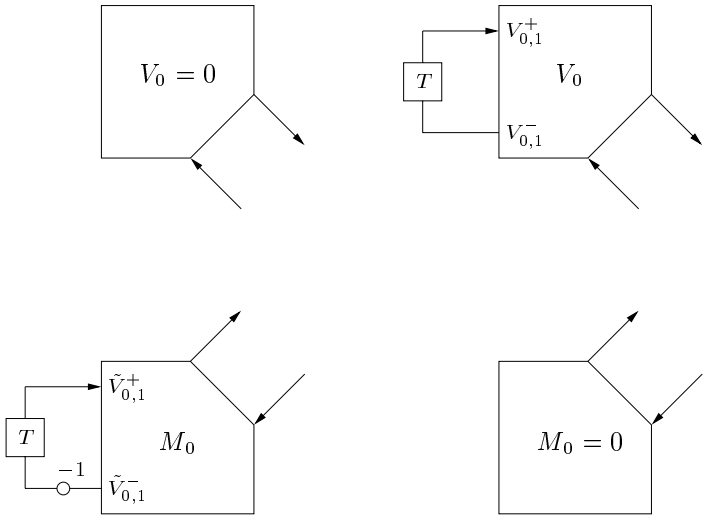

Figure 5-6: *Boundary Conditions for clamped and free ends.*

condition is analogous to that of the clamped boundary, only we apply the condition to the velocity junction as shown in the right-hand plot of Figure 5-6. This time V_0 becomes a two port junction, with one port attached to M_1, and the other employing a self loop with one unit of delay, but this time with no sign inversion.

5.2.3 Simulation

We carried out the following simulation to test the performance of the proposed model. We set the sample rate to $f_s = 44100Hz$, which would give a spatial step,

$$\Delta = \sqrt{\frac{1}{f_s \mu}}$$

in metres. We chose to model a steel bar with the following characteristics,

$$E = 1.4 \times 10^{12} N/m^2,$$
$$\rho = 5.38 \times 10^4 kg/m^3,$$

with a square cross section of height $h = 0.005m$. This results in a step size of approximately $\Delta = 1/55m$ and we considered modelling a bar of length $1m$. Notice that we chose a bar with a very small cross-section. This was done so as to keep the required sample rate down for the purposes of demonstration. Shown in Figure 5-7 are the transverse velocities along the bar for the first 20 steps of our simulation, where the bar had fixed ends which were allowed to pivot. The model clearly exhibits a frequency dependent speed of wave propagation, with the higher frequencies reaching the bound-

Mode n	f_n Theoretical (Hz)	f_n Modelled (Hz)	Error	f_n/f_1
1	11.56	11.5	0.06	1.000
2	46.26	45.5	0.76	3.957
3	104.09	103.0	1.9	8.957
4	185.05	182.5	2.55	15.870
5	289.14	284.5	4.64	24.740
6	416.37	408.5	7.87	35.522
7	566.72	554.0	12.72	48.217

Table 5.1: *Comparing theoretical and modelled resonant modes for the bar model.*

ary first. Furthermore the shape adopted by the impulse excitation as it spreads is entirely consistent with the expected shape as described in [33].

The analysis presented above is clearly an intuitive approach. We have already compared the dispersion characteristics of the model with the theory, and our observations are reaffirmed by this pictorial approach. However, in order to perform a more scientific analysis, we must consider the frequency spectrum of the output. This is shown in Figure 5-8. The sequence of resonant modes is clearly inharmonic. In fact, we observe that the spacing between the partials increases with increasing frequency in a manner consistent with the theory, as described in Appendix A.2. It is also possible to compare the numerical values of these resonant frequencies with the desired frequencies, which can be calculated using equation (A.10) from Appendix A.2.2. This comparison is presented in Table 5.1. We note that the fundamental is well tuned, although we predict that the inclusion of fractional delay loops at the boundary of the model would help represent the true length of the bar, and hence give a more accurate measure of the fundamental. Subsequent partials become more mis-tuned with increasing frequency, and this discrepancy is in keeping with the relative phase error of Figure 5-5 where errors increase with frequency. The amount of inharmonicity can be measured by calculating the ratio of each resonant frequency with the fundamental, as indicated in the final column of Table 5.1. This shows that the frequencies increase almost proportionally with n^2 as desired.

5.3 A Waveguide Stiff String Model

We now consider an extension to the stiff bar model described previously towards a model for a stiff string. The stiff string is described in Appendix A.2.3 and its equation consists of both a 'string' part and a 'bar' part.

$$\frac{\partial^2 u}{\partial t^2} = \frac{F}{\rho A}\frac{\partial^2 u}{\partial x^2} - \frac{EI}{\rho A}\frac{\partial^4 u}{\partial x^2}. \tag{5.16}$$

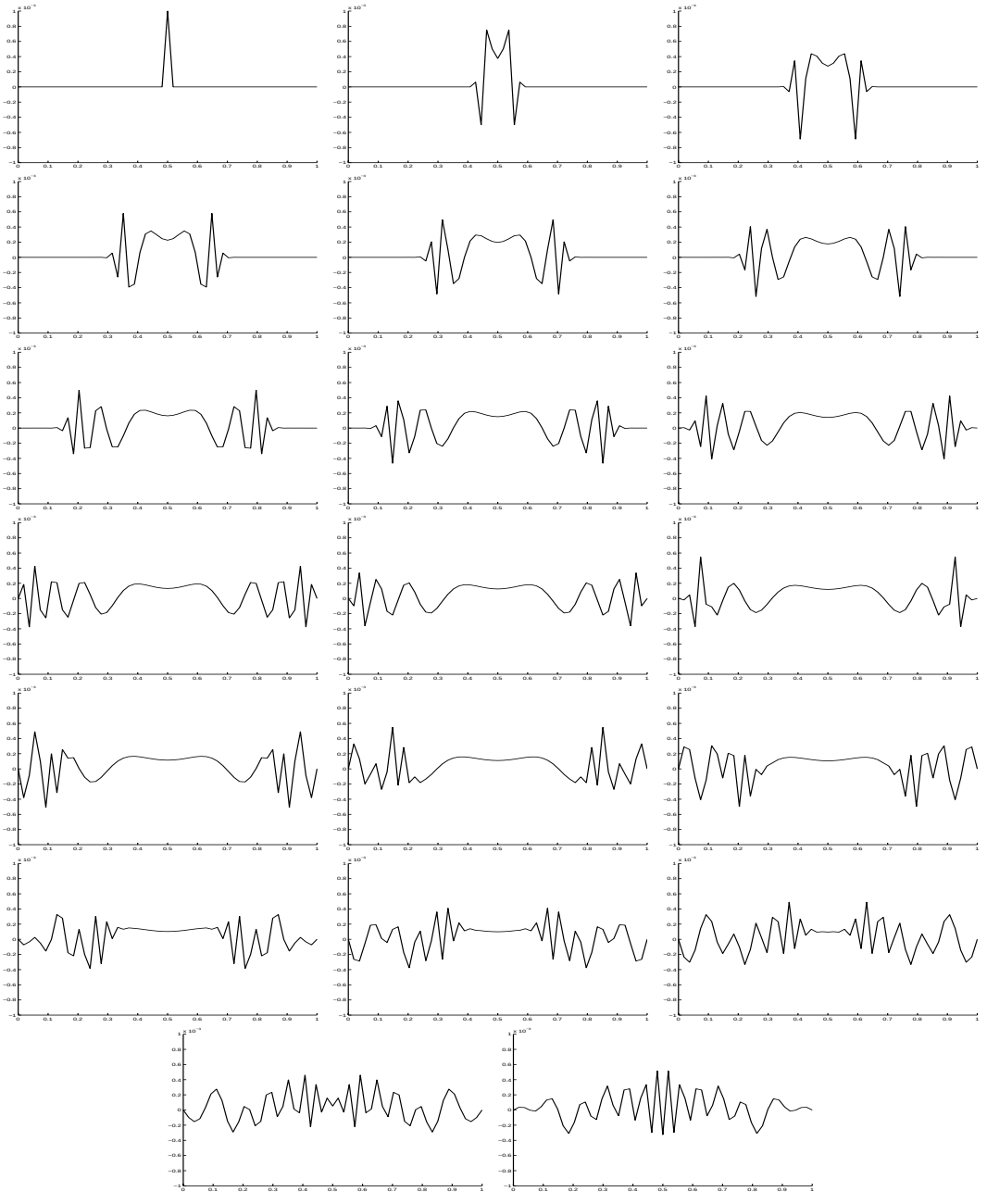

Figure 5-7: *Evolution of transverse velocity waves along Euler-Bernoulli Bar.*

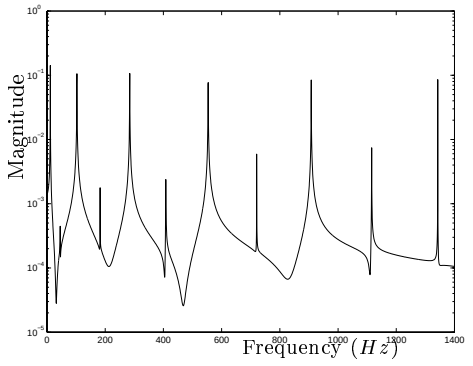

Figure 5-8: *Frequency Spectrum observed from bar model output.*

Since the PDE is constructed as a combination of the PDEs representing the string and bar, we consider a similar approach with our waveguide models. To each velocity junction in the waveguide bar model, we attach two new ports which attach to the neighbouring velocity junctions via a waveguide comprising one unit of delay. Such a construction is described in Figure 5-9. Notice the different impedances at each velocity junction. The 'string' part has impedance Y_F, while the bar part has impedance Y_E. We may also think of a stiff string as a thin circular bar, held at a particular tension, and this intuitive description is mirrored in the waveguide construction. Similarly to the bar model, the admittance at each force junction is $Z = \frac{1}{Y_E}$, although in the calculation of the junction force, this value cancels since each input has the same admittance so that Z is essentially arbitrary.

5.3.1 A FDS for the Stiff String Equation

Just as was the case in the previous sections, we may show that this waveguide model is entirely equivalent to a FDS for the underlying PDE. Using centered differences, a FDS for equation (5.16) is

$$\begin{aligned} U_j(n+1) - 2U_j(n) + U_j(n-1) &= \lambda^2 \frac{F}{\rho A}\left[U_{j-1}(n) - 2U_j(n) + U_{j+1}(n)\right] \\ &- \mu^2 \frac{EI}{\rho A}\left[U_{j-2}(n) - 4U_{j-1}(n) + 6U_j(n) - 4U_{j+1}(n) + U_{j+2}(n)\right], \quad (5.17) \end{aligned}$$

where $\lambda = \frac{T}{\Delta}$ and $\mu = \frac{T}{\Delta^2}$. Stability and dispersion characteristics of this scheme may be evaluated by computing the spectral amplification factor in the usual way. The amplification factor $g(w)$ is found as usual by solving the quadratic $g^2 + Bg + 1 = 0$

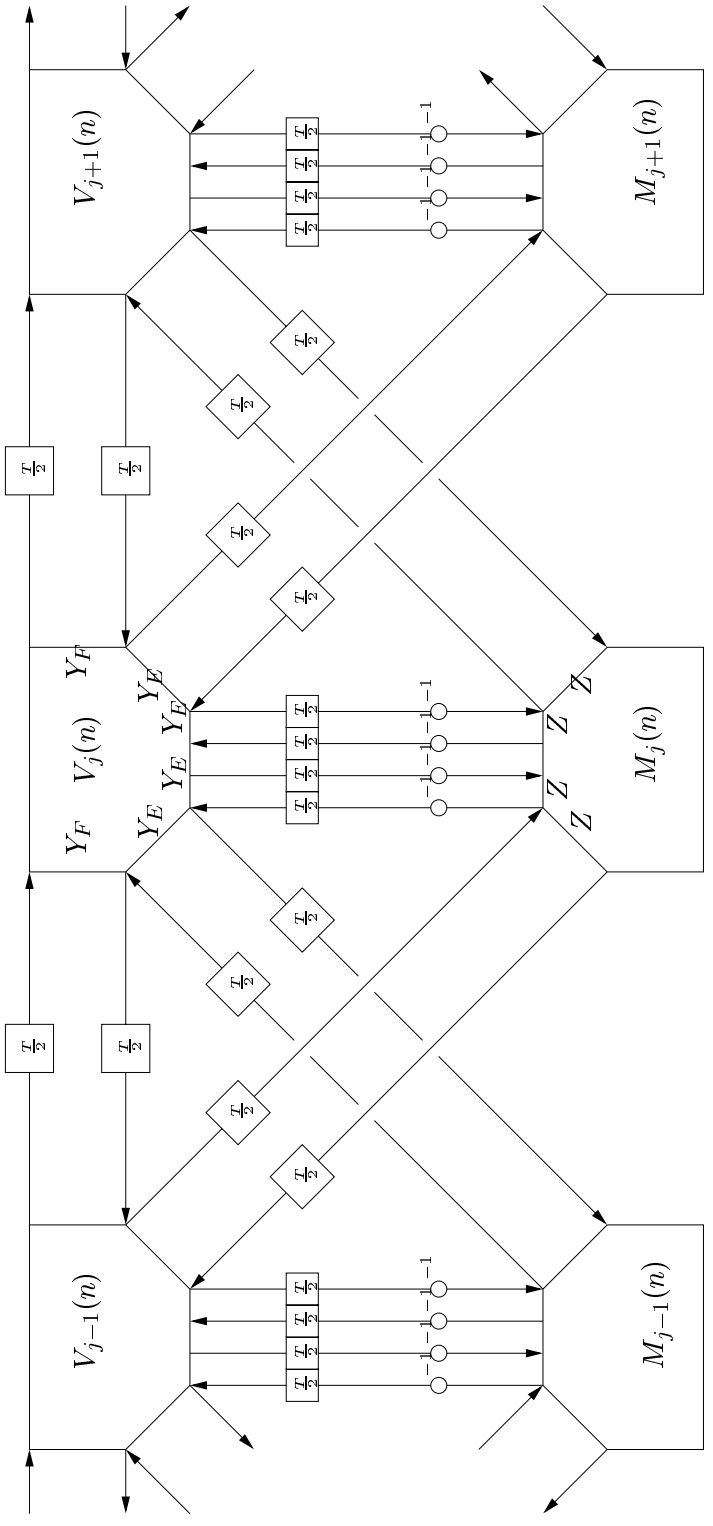

Figure 5-9: *Digital Waveguide Network for the Stiff String*

where

$$B = -2 + 4a^2\lambda^2 \sin^2\left(\frac{w}{2}\right) + 16b^2\mu^2 \sin^4\left(\frac{w}{2}\right),$$

and where $a^2 = \frac{F}{\rho A}$ and $b^2 = \frac{EI}{\rho A}$. As usual stability is achieved when $B^2 \leq 4$. For this to hold we thus require to have

$$a^2\lambda^2 \sin^2\left(\frac{w}{2}\right) + 4b^2\mu^2 \sin^4\left(\frac{w}{2}\right) \leq 1.$$

It is quite easy to show that the limit of stability is thus where $a^2\lambda^2 + 4b^2\mu^2 = 1$. Solving this equation gives the following relationship between the spatial and time steps

$$\frac{1}{\Delta^2} = \frac{a^2}{8b^2}\left[\sqrt{1 + \frac{16b^2}{a^4T^2}} - 1\right]. \tag{5.18}$$

Similarly to the analysis of the stiff bar model previously, we may discern the accuracy of the stiff string model by considering the relative phase of the amplification factor $g(w)$. This is calculated by considering the ratio of the phase of $g(w)$ with that of the true system. Formally, the relative phase is expressed as

$$\begin{aligned} K(w) &= \frac{arg\{g(w)\}}{T(a^2k^2 + b^2k^4)^{\frac{1}{2}}} \\ &= \frac{arg\{g(w)\}}{(a^2T^2k^2 + b^2T^2k^4)^{\frac{1}{2}}} \\ &= \frac{arg\{g(w)\}}{(a^2\frac{T^2}{\Delta^2}w^2 + b^2\frac{T^2}{\Delta^4}w^4)^{\frac{1}{2}}} \\ &= \frac{arg\{g(w)\}}{(a^2\lambda^2w^2 + b^2\mu^2w^4)^{\frac{1}{2}}} \end{aligned} \tag{5.19}$$

where again $w = k\Delta$ and

$$arg\{g(w)\} = \tan^{-1}\left(\frac{\sqrt{4 - B^2}}{-B}\right).$$

We note how putting $a = 0$ reduces the relative phase of the stiff string model to that of the stiff bar described in equation (5.15), while putting $b = 0$ gives the relative phase of the standard 1D waveguide for the ideal string.

Shown in Figure 5-10 are relative phase (or equally, relative dispersion) plots (in Hz) for the stiff string model for three values of the sample rate f_s. As was the case with the bar model previously we observe that dispersion error increases with frequency

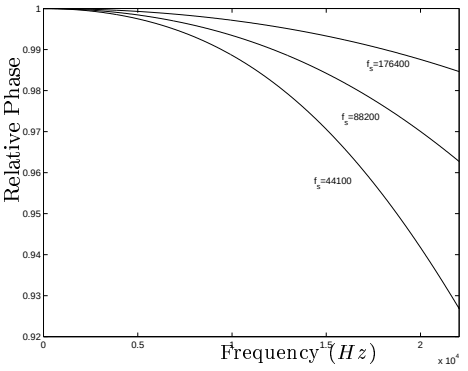

Figure 5-10: *Relative Phase Plots for the Stiff String Model.*

and that in increasing the sample rate the modelled output will converge to the true solution. We also note improved performance over the bar model discussed previously. This is not surprising, since at low frequencies in the stiff string model, tension will dominate, and the 1D waveguide for the ideal string is exact up to the Nyquist rate ($w = \pi$), and hence will have a relative phase of $K(w) = 1$ for all frequencies. At higher frequencies, stiffness dominates, and the system becomes more bar like, and consequently the phase error in the bar model shown in Figure 5-5 will compromise the accuracy.

5.3.2 Equivalence of the Stiff String Model to the FDS

It can be shown that the waveguide stiff string model of Figure 5-9 is equivalent to the FDS of equation (5.17). The proof of the equivalence follows much the same lines as that for the bar, but is a little unwieldy so we summarise the result here. A full derivation of the equivalence is given in Appendix D.1. The model results in the following difference scheme for the velocity waves

$$\begin{aligned} V_j(n+1) - 2V_j(n) + V_j(n-1) = \frac{2Y_F}{Y_J}\big[V_{j-1}(n) - 2V_j(n) + V_{j+1}(n)\big] \\ - \frac{Y_E}{Y_J}\big[V_{j-2}(n) - 4V_{j-1}(n) + 62V_j(n) - 4V_{j+1}(n) + V_{j+2}(n)\big], \end{aligned}$$

where the junction impedance is $Y_J = 2Y_F + 4Y_J$. This scheme is entirely equivalent to that of equation (5.17) by matching

$$\begin{aligned} \frac{2Y_F}{Y_J} &= \frac{F}{\rho A}\lambda^2 = a^2\lambda^2 \\ \frac{Y_E}{Y_J} &= \frac{EI}{\rho A}\mu^2 = b^2\mu^2. \end{aligned}$$

By working at the stability limit where $a^2\lambda^2 + 4b^2\mu^2 = 1$, and setting $Y_F = 1$ we must set the final impedance Y_E to

$$Y_E = \frac{2b^2\mu^2}{1 - 4b^2\mu^2} = \frac{1 - a^2\lambda^2}{2a^2\lambda^2}.$$

When performing a simulation in the next section, we shall see the importance of the value Y_E in determining how much closer to a bar or a string the model behaves, and consequently to the level of inharmonicity in the sound.

5.3.3 Simulation Results

We considered modelling two different strings in order to demonstrate the accuracy of the model, but also to serve as a demonstration of the inharmonicity observed in stiff string sounds. In real instruments, inharmonicity is generally undesired. For thicker strings this inharmonicity becomes greater, and thus such strings in pianos for instance, are usually constructed by wrapping a string around a central core so as to minimise the effect [15]. From our model we may quite readily isolate the effect of stiffness in strings without worrying about other frequency dependent or non-linear phenomena.

We consider representing two strings from a guitar. First of all we take a high E-string. We set the length to $65cm$. From [15, 49] such a string has Young's Modulus $E = 2 \times 10^{10}\ N/m$ and should be held at a tension $F = 123N/m$. Taking the string's cross-sectional radius to be $r = 0.0003385m$ means that to attain an ideal string fundamental frequency $f_1 = 330Hz$, the density should be $\rho = 1.8565 \times 10^3$. With such parameters, the ratio of the constants a and b is

$$\frac{a}{b} = 772.281.$$

Thus we should expect little inharmonicity, since the tension clearly dominates the PDE. The results of this simulation are summarised in Table 5.2. They show very little inharmonicity for the thin high pitched string. Note also the mis-tuned fundamental in each case.

In our second simulation we double the string radius and hold the string at a tension of $F = 30.38N/m$ in order to model a low E-string which should vibrate at $f_1 = 82Hz$. In this instance we expect greater inharmonicity and in fact the ratio of the model parameters a and b in this case is

$$\frac{a}{b} = 95.953.$$

Results of this simulation are shown in Table 5.3. Again we note the mis-tuned funda-

	Modelled		Theoretical	
Mode (n)	f_n	f_n/f_1	f_n	f_n/f_1
1	340	1.000	331.337	1.0000
2	679	1.997	662.713	2.0001
3	1018	2.994	994.167	3.0005
4	1358	3.994	1325.737	4.0012
5	1697	4.992	1657.462	5.0023
6	2038	5.994	1989.381	6.0041
7	2377	6.992	2321.533	7.0066
8	2719	7.997	2653.956	8.0098
9	3061	9.003	2986.690	9.0141
10	3403	10.009	3319.771	10.0193

Table 5.2: *Comparison of modelled and theoretical mode frequencies for a High E-string*

mental, but in this case where the string is thicker and the tension lower, we see how the inharmonicity is much greater as expected. This has identified the problem faced by string instrument manufacturers, where stiffness causes strings to vibrate inharmonically. This is why real strings found in musical instruments are usually constructed by wrapping one string around another string acting as a central core, and this construction minimises the effect of the stiffness.

Also shown in Tables 5.2 and 5.3 are theoretical mode frequencies as calculated using equation (A.12) in Appendix A.2.3. The parameters used are the same as were used in our models. Notice how the fundamental in each case is slightly higher than the desired fundamental. This is because the stiffness will cause an increase in all the mode frequencies, with a greater increase in the higher end of the spectrum. Also note how the models do not quite model the true fundamentals accurately. This can be attributed to an approximation in the length of each string in order to be represented by an integer number of waveguide junctions. We have seen earlier how this can be overcome by the use of fractional length waveguides, or by carefully specifying the sample rate. Comparing the theoretical and modelled outputs we observe a good level of accuracy in the model. In the case of the thicker low E-string we see how the stretching of the mode frequencies is less than that of the theory. This will be a consequence of the phase error observed in Figure 5-10. We also see the phase error evident in the high E-string simulation. In this case the contraction has caused the sequence of relative modes f_n/f_1 in the model to fall below that of a harmonic sequence. This is since we should be expecting little inharmonicity while the model still incurs a phase error. Examining the theoretical output, this inharmonicity should only be observed greatly in the 9th and 10th modes and this is mirrored in the model output.

	Modelled		Theoretical	
Mode (n)	f_n	f_n/f_1	f_n	f_n/f_1
1	87	1.0000	84.823	1.000
2	174	2.0000	170.270	2.0074
3	261	3.0000	256.965	3.0294
4	351	4.0345	345.334	4.0712
5	443	5.0920	436.598	5.1472
6	539	6.1954	530.784	6.2576
7	637	7.3228	628.715	7.4121
8	740	8.5057	731.015	8.6181
9	847	9.7356	838.309	9.8830
10	959	11.0230	951.221	11.2132

Table 5.3: *Comparison of modelled and theoretical mode frequencies for a Low E-string*

5.4 Conclusion and Discussion

In this chapter we discussed methods to model the bending waves inherent in the vibrations in stiff strings and bars. We discounted techniques involving non-linear phase filters since we felt they had little physical significance. We introduced and discussed a waveguide model for a vibrating bar and pointed out that such a model would be impossible using filters applied to a standard waveguide due to the need to represent a zero DC wave speed.

We calculated and analysed the phase error of the model and showed that dispersion error would increase with increasing frequency. We showed how increasing the sample rate yielded improved accuracy and demonstrated the convergence of the scheme for some different sample rates. This convergence is a feature of centred difference schemes. We briefly discussed the output of such a model where we noted that the errors were consistent with the dispersion error previously described.

We then extending the technique to include a model for a stiff string and similarly analysed the dispersion error which we note noted was less than that of the bar model since the model was closer to the original waveguide for the ideal string. Finally we discussed a simulation for the stiff string, demonstrating the inharmonicity found in real strings.

Chapter 6

2D Models Including Material Parameters

In this chapter we extend the ideas of the last section to 2D in order to model stiff plates and stiff membranes. The extension to meshes of both a square and triangular geometry is quite intuitive. A practical approach to modelling stiffness in membranes could have been to use the filtered mesh structure of chapter 2 with filter coefficients which not only correct the dispersion error, but speed up the higher frequencies. However, due to the existing dispersion error in the waveguide mesh, it would not be possible to provide the required variation in the wave speed between low and high frequencies. We examined this possibility, and surmised that such an approach was not useful [4].

6.1 Modelling Stiff Plates

The extension of the 1D digital waveguide model for a bar to two dimensions is quite straightforward. In this section we first describe a FDS for the 2D stiff plate equation based on a rectilinear grid and discuss its dispersion characteristics. We show how we may similarly derive a FDS for a triangular grid and discuss perceived improvements in propagation characteristics. Then we describe a digital waveguide model for the stiff plate, based on a simple extension of the 1D waveguide bar model discussed in the previous chapter. We provide a performance evaluation by comparing the model output to the expected output from the theory.

The complete theory for a vibrating plate is quite complex and is described in Appendix A.4. Given a rectangular plate for example, each edge may be terminated in any of three ways, with a clamped, pinned or free edge. Thus, there are 27 different combinations of boundary conditions, each leading to its own set of vibrational modes.

The difficulties experienced in finding analytical solutions in each of these cases is one of the reasons why an accurate modelling technique can be extremely useful.

6.1.1 Finite Difference Schemes for the Stiff Plate Equation

We begin by describing a FDS for the underlying PDE representing the stiff plate. The ideal plate is described by the governing equation

$$\frac{\partial^2 u}{\partial t^2} + \frac{Eh^2}{12\rho(1-\nu^2)}\nabla^4 u = 0, \tag{6.1}$$

where h is the plate thickness, ρ is the density, E is Young's Modulus, ν is Poisson's ratio and $u(x, y, t)$ represents transverse displacement of the plate in terms of spatial position and time. This is a clear generalisation of the Euler-Bernoulli equation encountered previously. In standard rectilinear coordinates the 4th order 2D spatial derivative on the right hand side of equation (6.1) is

$$\nabla^4 = \frac{\partial^4}{\partial x^4} + 2\frac{\partial^4}{\partial x^2 \partial y^2} + \frac{\partial^4}{\partial y^4}.$$

We note that we may also describe this derivative in triangular coordinates as

$$\nabla^4 = \frac{4}{9}\left(\frac{\partial^4}{\partial l^4} + \frac{\partial^4}{\partial m^4} + \frac{\partial^4}{\partial x^4} + 2\frac{\partial^4}{\partial l^2 \partial m^2} + 2\frac{\partial^4}{\partial l^2 \partial x^2} + 2\frac{\partial^4}{\partial m^2 \partial x^2}\right),$$

for the new axial directions l, m and x. Also we note that we have restricted our study to the idealised case based on the 2D extension of the Euler-Bernoulli bar as opposed to the Mindlin plate theory which is an extension of the Timoshenko beam theory. We do this since this theory should suffice for musical sound modelling and also for simplicity [11]. A waveguide plate model based on the Mindlin theory has also been presented in [8]. Again this model is theoretical and has yet to be subjected to rigorous simulation. Thus it seems more reasonable to begin with simulations of the more simplistic case. Furthermore, theory exists for the extension of this plate theory to deal with stiff membranes, much like the case for stiff strings, thus we feel it important to develop it for this study.

In a similar derivation to the 1D case, we consider the decoupled system

$$\begin{aligned} \frac{\partial v}{\partial t} &= -\frac{1}{12\rho(1-\nu^2)}\nabla^2 m \\ \frac{\partial m}{\partial t} &= Eh^2\nabla^2 v, \end{aligned} \tag{6.2}$$

achieved by putting $v = \frac{\partial u}{\partial t}$ and $m = Eh^2\nabla^2 u$. For standard rectilinear coordinates, a FDS for equation (6.2) can derived for the discrete variables V and M by applying centered differences directly

$$\begin{aligned} V_{i,j}(n+1) - V_{i,j}(n) &= -\frac{1}{l}\mu\big[M_{i,j+1}(n+\frac{1}{2}) - 2M_{i,j}(n+\frac{1}{2}) + M_{i,j-1}(n+\frac{1}{2})\big] \\ &\quad - \frac{1}{l}\mu\big[M_{i-1,j}(n+\frac{1}{2}) - 2M_{i,j}(n+\frac{1}{2}) + M_{i+1,j}(n+\frac{1}{2})\big], \\ M_{i,j}(n+\frac{1}{2}) - M_{i,j}(n+\frac{1}{2}) &= -c\mu\big[V_{i,j+1}(n) - 2V_{i,j}(n) + V_{i,j-1}(n)\big] \\ &\quad - c\mu\big[V_{i-1,j}(n) - 2V_{i,j}(n) + V_{i+1,j}(n)\big], \end{aligned} \tag{6.3}$$

where $\mu = \frac{T}{\Delta^2}$, $\frac{1}{l} = \frac{1}{12\rho(1-\nu^2)}$ and $c = Eh^2$. By expressing the FDS in this form, that is with two wave variables, it should be clear that any waveguide implementation will deal with two coupled waveguide meshes. Note, however, that these two coupled FDSs are entirely equivalent to the following scheme derived by applying centered differences to equation (6.1),

$$\begin{aligned} &V_{i,j}(n+1) - 2V_{i,j}(n) + V_{i,j}(n-1) = \\ &\quad -\frac{Eh^2}{12\rho(1-\nu^2)}\mu^2\big[V_{i+2,j}(n) + V_{i,j+2}(n) + V_{i-2,j}(n) + V_{i,j-2}(n) \\ &\quad -8V_{i+1,j}(n) - 8V_{i,j+1}(n) - 8V_{i-1,j}(n) - 8V_{i,j-1}(n) + 2V_{i+1,j+1}(n) \\ &\qquad + 2V_{i-1,j+1}(n) + 2V_{i-1,j-1}(n) + 2V_{i+1,j-1}(n) + 20V_{i,j}(n)\big]. \end{aligned} \tag{6.4}$$

We may analyse the relative phase of this FDS in the usual way by taking Fourier Transforms of each side of equation (6.4). The spectral amplification factor, $g(\mathbf{w})$, where $\mathbf{w}$ is the 2D spatial frequency vector $\mathbf{w} = (w_x, w_y)^t$, may be calculated by solving the quadratic

$$g(\mathbf{w})^2 + (B-2)g(\mathbf{w}) + 1 = 0,$$

where for a rectilinear mesh

$$\begin{aligned} B = \frac{Eh^2}{12\rho(1-\nu^2)}\mu^2\big[&2\cos(2w_x) + 2\cos(2w_y) - 16\cos(w_x) - 16\cos(w_y) \\ &+4\cos(w_x+w_y) + 4\cos(w_x-w_y) + 20\big]. \end{aligned} \tag{6.5}$$

The resultant amplification factor is always complex with unit magnitude. This means the scheme is stable and lossless. Then the relative phase is calculated similarly to

equation (5.15) in Section 5.2.1 as

$$K(\mathbf{w}) = \frac{arg\{g(\mathbf{w})\}}{b\mu|\mathbf{w}|^2}, \tag{6.6}$$

where $b^2 = \frac{Eh^2}{12\rho(1-\nu^2)}$.

Shown in Figure 6-1 are relative phase plots for plate models using both a square mesh and a triangular mesh. For a triangular mesh, the spectral amplification factor is calculated using

$$\begin{aligned} B = \frac{Eh^2}{12\rho(1-\nu^2)}\mu^2\frac{4}{9}\big[&42 - 20\cos(w_x) + 4\cos(\sqrt{3}w_y) \\ &-20\cos\frac{1}{2}(w_x + \sqrt{3}w_y) - 20\cos\frac{1}{2}(w_x - \sqrt{3}w_y) \\ &+4\cos\frac{1}{2}(3w_x + \sqrt{3}w_y) + 4\cos\frac{1}{2}(3w_x - \sqrt{3}w_y) \\ &+2\cos(2w_x) + 2\cos(w_x + \sqrt{3}w_y) + 2\cos(w_x - \sqrt{3}w_y)\big], \end{aligned} \tag{6.7}$$

in place of equation (6.5). The top left and right hand plots show grey scale relative phase plots of $K(\mathbf{w})$ for square and triangular mesh geometries respectively. A degree of direction dependence is clearly visible for the square mesh model in analogy to the direction dependence found in the dispersion of standard 2D waveguide meshes in section 2.4. The bottom left hand plot shows two cross sections of the relative phase plot for a square mesh plate model. The upper of the two curves shows the diagonal cross section which shows reasonable accuracy in keeping with that found in the 1D bar model of the previous chapter. The lower curve, however, indicates the horizontal cross section and quite poor dispersion is observed. This can be attributed to a combination of the error found in the 1D bar model and the phase error encountered in the standard 2D waveguide mesh. The bottom right hand plot of Figure 6-1 shows equivalent cross sections of the relative phase for the triangular mesh. This indicates a higher degree of error than the diagonal cross section of the square mesh, but also describes a direction independent nature. As was the case in 1D, increasing the sample rate will improve the quality of the simulation. In this case however, where the dispersion error is greater, we would need to raise the sample rate higher than in the 1D case to obtain the same levels of accuracy and convergence to the true solution would be slower.

6.1.2 The 2D Waveguide Plate Model

The 2D waveguide plate model is achieved by coupling two interleaved square meshes together. Two interleaved square waveguide meshes are placed one spatial position out

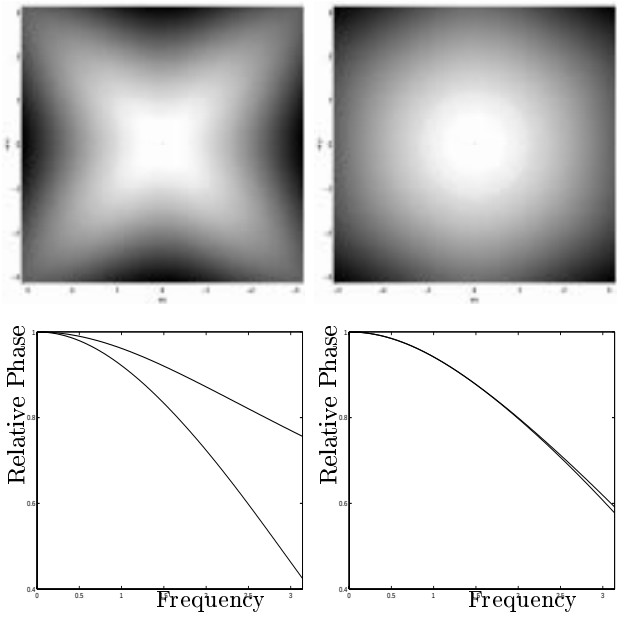

Figure 6-1: *Relative Phase Plots for Square and Triangular Mesh Stiff Plate Models*

of synchronisation with each other in each spatial direction as shown in Figure 6-2. Thus velocity junctions of one mesh align spatially with force junctions of the other mesh. The coupling (indicated with the large arrow in Figure 6-2) is performed using four waveguides, each implementing half a unit of delay and carrying a sign inversion, as shown in Figure 6-3. Also shown in Figure 6-3 are the wave variables, where we denote velocity waves impinging upon a force junction with $\tilde{V}$ so as to differentiate them with velocities impinging upon the velocity junction at the same spatial position.

To derive the equivalence of this waveguide structure to the FDS described in equation (6.3) we may proceed in a similar manner to that of the 1D case. We begin with the standard expression for junction velocity then use equations (5.5), (5.6), (5.7)

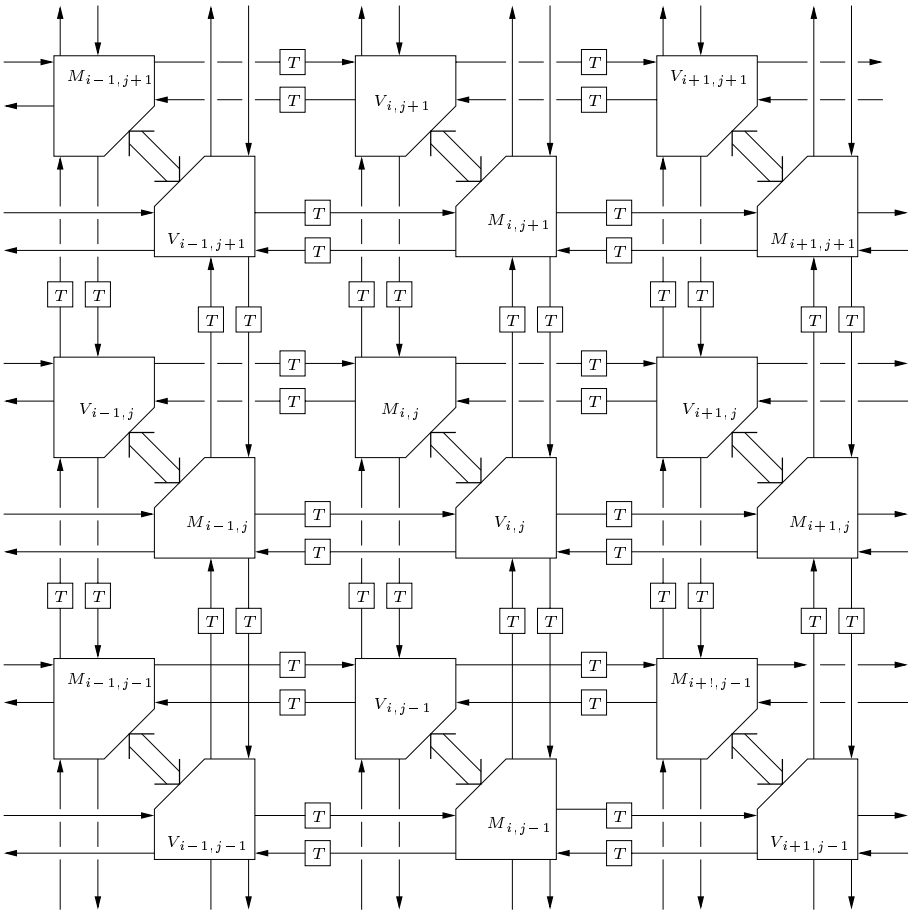

Figure 6-2: *Square Mesh Waveguide Plate Model.*

and (5.8),

$$
\begin{aligned}
V_{i,j}(n+1) &= \frac{2}{Y_J}\sum_{k=0}^{7} Y_k V^+_{i,j,k}(n+1) \\
&= \frac{2}{Y_J}\Big[Y_0\tilde{V}^-_{i+1,j,2}(n+\tfrac{1}{2}) + Y_1\tilde{V}^-_{i,j+1,3}(n+\tfrac{1}{2}) + Y_2\tilde{V}^-_{i-1,j,0}(n+\tfrac{1}{2}) + Y_3\tilde{V}^-_{i,j-1,1}(n+\tfrac{1}{2}) \\
&\qquad - \sum_{k=4}^{7} Y_k\tilde{V}^-_{i,j,k}(n+\tfrac{1}{2})\Big] \\
&= \frac{2}{Y_J}\Big[-M^-_{i+1,j,2}(n+\tfrac{1}{2}) - M^-_{i,j+1,3}(n+\tfrac{1}{2}) - M^-_{i-1,j,0}(n+\tfrac{1}{2}) - M^-_{i,j-1,1}(n+\tfrac{1}{2}) \\
&\qquad + \sum_{k=4}^{7} M^-_{i,j,k}(n+\tfrac{1}{2})\Big] \\
&= \frac{2}{Y_J}\Big[[-M_{i+1,j}(n+\tfrac{1}{2}) - M_{i,j+1}(n+\tfrac{1}{2}) - M_{i-1,j}(n+\tfrac{1}{2}) - M_{i,j-1}(n+\tfrac{1}{2}) + 4M_{i,j}(n+\tfrac{1}{2})\Big] \\
&\quad - \frac{2}{Y_J}\Big[-M^+_{i+1,j,2}(n+\tfrac{1}{2}) - M^+_{i,j+1,3}(n+\tfrac{1}{2}) - M^+_{i-1,j,0}(n+\tfrac{1}{2}) - M^+_{i,j-1,1}(n+\tfrac{1}{2}) \\
&\qquad + \sum_{k=4}^{7} M^+_{i,j,k}(n+\tfrac{1}{2})\Big] \\
&= -\frac{2}{Y_J}\Big[M_{i+1,j}(n+\tfrac{1}{2}) + M_{i,j+1}(n+\tfrac{1}{2}) + M_{i-1,j}(n+\tfrac{1}{2}) + M_{i,j-1}(n+\tfrac{1}{2}) - 4M_{i,j}(n+\tfrac{1}{2})\Big] \\
&\quad - \frac{2}{Y_J}\Big[-Y_0\tilde{V}^+_{i+1,j,2}(n+\tfrac{1}{2}) - Y_1\tilde{V}^+_{i,j+1,3}(n+\tfrac{1}{2}) - Y_2\tilde{V}^+_{i-1,j,0}(n+\tfrac{1}{2}) - Y_3\tilde{V}^+_{i,j+1,1}(n+\tfrac{1}{2}) \\
&\qquad + \sum_{k=4}^{7} Y_k\tilde{V}^+_{i,j,k}(n+\tfrac{1}{2})\Big] \\
&= -\frac{2}{Y_J}\Big[M_{i+1,j}(n+\tfrac{1}{2}) + M_{i,j+1}(n+\tfrac{1}{2}) + M_{i-1,j}(n+\tfrac{1}{2}) + M_{i,j-1}(n+\tfrac{1}{2}) - 4M_{i,j}(n+\tfrac{1}{2})\Big] \\
&\quad + \frac{2}{Y_J}\sum_{k=0}^{7} Y_k V^-_{i,j,k}(n) \\
&= -\frac{2}{Y_J}\Big[M_{i+1,j}(n+\tfrac{1}{2}) + M_{i,j+1}(n+\tfrac{1}{2}) + M_{i-1,j}(n+\tfrac{1}{2}) + M_{i,j-1}(n+\tfrac{1}{2}) - 4M_{i,j}(n+\tfrac{1}{2})\Big] \\
&\quad + V_{i,j}(n),
\end{aligned}
\tag{6.8}
$$

where $Y_J = \sum_{k=0}^{7} Y_k$ is the total junction impedance at a velocity junction and Y_k is the input impedance at the kth port. By inspection we see that this difference scheme is entirely equivalent to the FDS of equation (6.3) by setting

$$
\frac{2}{Y_J} = \frac{\mu}{12\rho(1-\nu^2)}. \tag{6.9}
$$

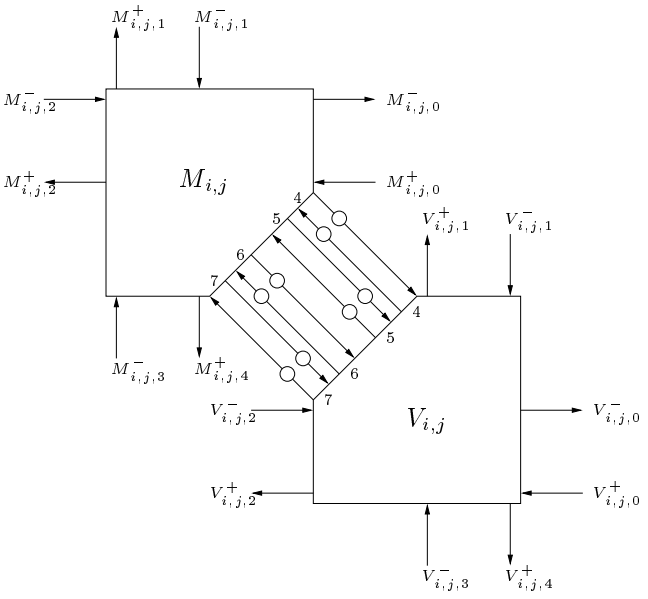

Figure 6-3: *Coupling in waveguide plate model.*

Similarly we may also begin with a force junction to yield the difference scheme

$$\begin{aligned} &M_{i,j}(n+\frac{1}{2}) - M_{i,j}(n-\frac{1}{2}) \\ &\quad = \frac{2}{Z_J}\left[V_{i+1,j}(n) + V_{i,j+1}(n) + V_{i-1,j}(n) + V_{i,j-1}(n) - 4V_{i,j}(n)\right], \end{aligned} \tag{6.10}$$

where $Z_J = \sum_{k=0}^{7} Z_k$ is the total junction admittance. This scheme is equivalent to the FDS of (6.3) by setting

$$\frac{2}{Z_J} = Eh^2\mu. \tag{6.11}$$

The two conditions (6.10) and (6.11) are satisfied for spatially constant material parameters by setting $Y_k = Y = \sqrt{12Eh^2\rho(1-\nu^2)}$, giving in turn

$$\mu = \frac{1}{4}\sqrt{\frac{12\rho(1-\nu^2)}{Eh^2}}. \tag{6.12}$$

Notice the similarity between the impedance value Y here with the corresponding value for the waveguide bar model described in section 5.2.

6.1.3 Simulation Example

We carried out a simulation for a square steel plate of length $a = 0.5m$, with thickness $h = 0.005m$, $E = 1.4 \times 10^{12} N/m^2$, $\rho = 53800 kg/m^3$ and $\nu = 0.3$. The resulting spatial

Mode	Theoretical	Modelled	Error	f_{mn}/f_{11} (Model)	f_{mn}/f_{11} (Theory)
f_{11}	96.9932	97	0.0068	1.0000	1.0
f_{12}	242.4831	241	1.4831	2.4845	2.5
f_{22}	387.9729	383	4.9729	3.9485	4.0
f_{13}	484.9662	479	5.9662	4.9381	5.0
f_{23}	630.4560	623	7.456	6.4227	6.5
f_{14}	824.4425	809	15.4425	8.3402	8.5
f_{33}	872.9391	861	11.9391	8.8763	9.0

Table 6.1: *Comparing theoretical and modelled resonant modes (in Hz) for the plate model.*

step size was $\Delta = 0.01323m$, giving a mesh of size 38×38 nodes.

The results of the simulation using a square mesh are summarised in Table 6.1 where the expected mode frequencies for a square plate with simply supported edges were calculated using the following equation from Appendix A.4.2.

$$f_{mn} = \frac{\pi}{2a}\sqrt{\frac{Eh^2}{12\rho(1-\nu^2)}}\left(n^2+m^2\right). \tag{6.13}$$

The simply supported boundary condition is implemented in the waveguide plate model by simply terminating the meshes with inverting self-loops, as was the case with the termination of the stiff bar. From the table we note a good tuning of the fundamental and by comparing the last two columns we observe that the level of inharmonicity over the first 5 modes is consistent with the theory. We see that the 6th mode is poorly represented, and that all the errors are of the form of a contraction, that is, the natural frequencies are underestimated. By noting that the $7th$ mode, the f_{33} mode, is better resolved than the previous one, f_{14}, we see how the direction dependence of the phase error affects any simulation. Figure 6-1 showed how the diagonal cross-section of the relative phase plot was better than the horizontal, and this is mirrored in the model output where diagonal modes are resolved more accurately than horizontal ones. We also note that the errors are generally larger than those found in the equivalent 1D bar model (Table 5.1). Firstly, this plate model has a larger fundamental frequency, so all subsequent modes are larger and should suffer more from phase error. Secondly, we might expect that the extension of the bar model to 2D should introduce additional dispersion error, similar to that found in the standard 2D waveguide mesh in chapter 2.

6.2 Stiff Membranes

A stiff membrane model may be quite easily realised by applying the stiff string model to two dimensions. Again we may consider meshes of either a square or triangular geometry. For a square mesh the waveguide stiff membrane model may be realised by adding extra waveguide connections of one unit of delay between velocity junctions to the plate model described in Figure 6-2. We begin by discussing the equivalent FDS.

6.2.1 FDS for the Stiff Membrane

The stiff membrane equation is described in Appendix A.4.3 as

$$\frac{\partial^2 u}{\partial t^2} = \frac{F}{\rho}\nabla^2 u - \frac{Eh^2}{12\rho(1-\nu^2)}\nabla^4 u,$$

where we have simply introduced tension F to the ordinary stiff plate equation. A centered FDS on a rectilinear grid is

$$\begin{aligned} V_{i,j}(n+1) - 2V_{i,j}(n) + V_{i,j}(n-1) = a^2\lambda^2\big[&V_{i+1,j}(n) - 2V_{i,j}(n) + V_{i-1,j}(n) \\ &+ V_{i,j+1}(n) - 2V_{i,j}(n) + V_{i,j-1}(n)\big] \\ - b^2\mu^2\big[&V_{i+2,j}(n) + V_{i,j+2}(n) + V_{i-2,j}(n) + V_{i,j-2}(n) \\ &- 8V_{i+1,j}(n) - 8V_{i,j+1}(n) - 8V_{i-1,j}(n) - 8V_{i,j-1}(n) \\ &+ 2V_{i+1,j+1}(n) + 2V_{i-1,j+1}(n) + 2V_{i-1,j-1}(n) \\ &+ 2V_{i+1,j-1}(n) + 20V_{i,j}(n)\big], \end{aligned} \tag{6.14}$$

where $a^2 = \frac{F}{\rho}$, $b^2 = \frac{Eh^2}{12\rho(1-\nu^2)}$ and as usual $\lambda = \frac{T}{\Delta}$, $\mu = \frac{T}{\Delta^2}$. Stability of this scheme is determined by considering the spectral amplification factor $g(\mathbf{w})$ found by solving the quadratic $g^2 + Bg + 1 = 0$ where

$$\begin{aligned} B &= -2 + 4a^2\lambda^2\big[\sin^2(\frac{w_x}{2}) + \sin^2(\frac{w_y}{2})\big] \\ &+ 16b^2\mu^2\big[\sin^4(\frac{w_x}{2}) + \sin^4(\frac{w_y}{2}) + \sin^2(\frac{w_x}{2}) + \sin^2(\frac{w_y}{2}) \\ &\quad -\frac{1}{2}\sin^2(\frac{w_x+w_y}{2}) - \frac{1}{2}\sin^2(\frac{w_x-w_y}{2})\big]. \end{aligned}$$

Stability of the scheme is achieved for $B < 2$, since where the amplification factor is complex with unit magnitude. Thus at the stability limit,

$$a^2\lambda^2 + 8b^2\mu^2 = \frac{1}{2}. \tag{6.15}$$

Note that when either a or b is zero, that is in the instances of zero tension or zero stiffness, the stability bound reduces to that found in the standard membrane or stiff plate schemes respectively. For example in the absence of any tension we have $a = 0$ and equation (6.15) becomes $\mu = \frac{1}{4}\frac{1}{b}$ which is the same as the bound for the stiff plate model in equation (6.12) in section 6.1.2. If, on the other hand, we remove the stiffness so that $b = 0$ we regain the relationship $\Delta = \sqrt{2}cT$ which is the standard stability bound for a 2D mesh applied to the 2D wave equation in section 2.3

Solving equation (6.15) for λ^2/T^2 gives the following expression for the spatial step Δ in terms of the PDE constants and the time step T.

$$\frac{\lambda^2}{T^2} = \frac{1}{\Delta^2} = \frac{a^2}{16b^2}\left[\sqrt{1 + \frac{16b^2}{a^4T^2}} - 1\right]. \tag{6.16}$$

Note the similarity between this expression and equation (5.18) for the stiff string model.

Using this value for the spatial step we may calculate the relative phase of the FDS for both square and triangular meshes as

$$K(\mathbf{w}) = \frac{arg\{g(\mathbf{w})\}}{(a^2\lambda^2|\mathbf{w}|^2 + b^2\mu^2|\mathbf{w}|^4)^{\frac{1}{2}}}, \tag{6.17}$$

where we note the similarity between this expression and that for the relative phase of the 1D stiff string model in equation (5.19).

Figure 6-4 shows grey scale and cross sectional plots of the relative phase errors for the stiff membrane model with both square and triangular meshes. Note the similarity to Figure 6-1, and in particular the direction dependence of the square mesh, shown in the two left hand plots. A closer inspection of the two cross sectional plots, which show best and worse cases of the relative phase for the square mesh, left, and the triangular mesh, right, show that better accuracy is attained at low frequencies, than was observed for the plate model. This is an analogy to the case of the stiff string, where for low frequencies where tension dominates the equation, the 1D waveguide model is highly accurate. It should be noted that in both this model, and that of the plate, the phase error observed in the equivalent 1D case is added to by the phase error found in the 2D membrane simulations examined in chapter 2.

6.2.2 Equivalent Waveguide Model

Deriving an equivalent waveguide structure to a FDS for the stiff membrane equation is a straightforward extension to the process described for the stiff string model in

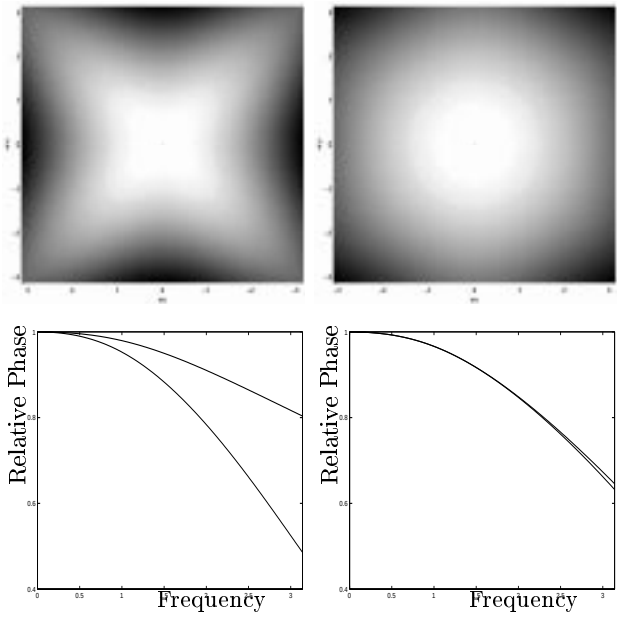

Figure 6-4: *Relative Phase Plots for Square and Triangular Mesh Stiff Membrane Models*

section 5.3. Again the calculation is very involved so we do not reproduce it here but give the derivation in Appendix D.2. The model consists of two coupled waveguide meshes, one comprised of velocity junctions, the other of force junctions. The force junctions have the same structure as in the waveguide plate model described earlier in this chapter. The velocity junctions are 12-ports, where 8 are attached with impedance Y_E and connect via half length waveguides to force junctions, and where the other four ports attach via unit length waveguides of impedance Y_F to the neighbouring velocity junctions. The equivalence with the FDS of equation (6.14) is achieved by setting

$$\frac{Y_E}{2Y_J} = \frac{Eh^2}{12\rho(1-\nu^2)}\mu^2, \qquad \frac{2Y_F}{Y_J} = \frac{F}{\rho}\lambda^2,$$

where Y_J is the total junction impedance given by $Y_J = 8Y_E + 4Y_F$. These equations may be easily solved by setting $Y_F = 1$ giving

$$Y_E = \frac{8b^2\mu^2}{1-16b^2\mu^2} = \frac{1-2a^2\lambda^2}{4a^2\lambda^2}.$$

6.3 Conclusion and Discussion

In this chapter we extended the 1D results of chapter 5 to 2D to include models for stiff plates and stiff membranes. We discussed dispersion characteristics for each system for

meshes of both square and triangular geometries and proved the equivalence of our waveguide structures with direct centred FDSs for the underlying PDEs.

We observed from the relative phase plots that dispersion error was dependent on both direction and frequency, with frequencies on the diagonal being better represented than horizontal and vertical angular frequencies. This was analogous to the case of using the standard square waveguide mesh when modelling an ideal membrane, as described in chapter 2. Consequently we observed that using a triangular mesh would reduce the level of directional dependence in the dispersion error, although the error was greater than that of the diagonal frequencies of the square mesh.

We discussed the accuracy of the plate model in section 6.1.3 where errors were consistent with those predicted by the dispersion error, that is errors were larger in the horizontal and vertical modes than in the diagonal modes. We also observed larger errors in the horizontal and vertical modes than those found in the 1D bar model of the previous chapter. This is again analogous to the case of the ideal membrane models described in chapter 2 where using a square mesh we had no dispersion error in the diagonal direction, but large dispersion error in the horizontal and vertical directions. The 2D bar model incurs a dispersion error which is a combination of the error found in the standard 2D waveguide mesh, and the dispersion error of the 1D bar model.

With the stiff membrane model described in section 6.2 a similar experiment to that performed in section 5.3.3 for a stiff string could be conducted. Inclusion of this model within the drum model framework of chapter 4 would also be an interesting exercise in order to investigate the effect of membrane stiffness on drum sounds.

Chapter 7

Representing Internal Damping

Often what characterises the sound of a vibrating object is the internal damping. In this chapter we discuss how it is possible to introduce simple viscoelastic behaviour to a waveguide model representing foundation stiffness or viscosity. This waveguide model is equivalent to a system formed by placing a string on a viscoelastic foundation of a spring and dashpot in parallel as described in Appendix A.3. In the future it is envisaged that this waveguide model could be extended to cover more complicated viscoelastic foundations which represent the frequency dependent damping found in real materials. However, this is left as a future study and in this section we discuss only the simplest case.

7.1 The string on an elastic sub-base

In this section we describe how it is possible to model a string placed on a purely elastic foundation. We discuss the theory in A.3 wherein we find that the principal consequence of the addition of an elastic sub-base is to introduce additional dispersion causing an increase in the fundamental frequency together with a change in the pattern of resonant modes. We observe that at low frequency each resonant mode is close to the next one, and that as we move up the frequency axis, the modes approach a harmonic sequence. In the waveguide model which follows we prove an equivalence with a FDS for the modified wave equation and discuss the accuracy by calculating fundamental frequencies and the arrangement of the resonant modes for various values of the spring stiffness coefficient. It is also important to note that the model may also be used to introduce locally varying dispersion which is important when looking towards modelling resonators whose material properties vary spatially.

We begin in the usual way by first describing a FDS for the underlying equation

described in Appendix A.3.1 by

$$\rho\frac{\partial^2 u}{\partial t^2} = F\frac{\partial^2 u}{\partial x^2} - Gy,$$

which corresponds to a string of density ρ, held at tension F and placed on an elastic foundation of stiffness G. By using centered differences we may quite simply write a FDS for this as

$$U_j(n+1) - 2U_j(n) + U_j(n-1) = \lambda^2\frac{F}{\rho}\left[U_{j-1}(n) - 2U_j(n) + U_{j+1}(n)\right] - T^2\frac{G}{\rho}U_j(n), \quad (7.1)$$

for time step T, spatial step Δ and with $\lambda = \frac{T}{\Delta}$.

Now, we construct our waveguide model by using a standard waveguide, but where each junction has an additional self loop consisting of one unit of delay together with a sign inversion. Now setting the impedance of the self loop to R_s and all other impedances to unity, the junction velocity equation may be manipulated as follows,

$$\begin{aligned}
V_j(n+1) &= \frac{2}{R}\left[V^+_{j,1}(n+1) + V^+_{j,2}(n+1) + R_s V^+_{j,3}(n+1)\right] \\
&= \frac{2}{R}\left[V^-_{j-1,2}(n) + V^-_{j+1,1}(n) - R_s V^-_{j,3}(n)\right] \\
&= \frac{2}{R}\left[V_{j-1}(n) + V_{j+1}(n) - R_s V_j(n)\right] \\
&- \frac{2}{R}\left[V^+_{j-1,2}(n) + V^+_{j+1,1}(n) - R_s V^+_{j,3}(n)\right] \\
&= \frac{2}{R}\left[V_{j-1}(n) + V_{j+1}(n) - R_s V_j(n)\right] \\
&- \frac{2}{R}\left[V^-_{j,1}(n-1) + V^-_{j,2}(n-1) + R_s V^-_{j,3}(n-1)\right] \\
&= \frac{2}{R}\left[V_{j-1}(n) + V_{j+1}(n) - R_s V_j(n)\right] - V_j(n-1),
\end{aligned}$$

where $R = 2 + R_s$ is the total junction impedance. This may be re-written as

$$V_j(n+1) - 2V_j(n) + V_j(n-1) = \frac{2}{R}\left[V_{j-1}(n) - 2V_j(n) + V_{j+1}(n)\right] - \frac{4R_s}{R}V_j(n).$$

Now this is clearly equivalent to the FDS of equation (7.1) by setting

$$\begin{aligned}
\frac{2}{R} &= \frac{F}{\rho}\lambda^2, \\
\frac{4R_s}{R} &= \frac{GT^2}{\rho},
\end{aligned}$$

Stiffness G	Model Frequency (Hz)	Theoretical Frequency (Hz)
0	96	96.1769
1	96	96.1776
10	96	96.1835
10^2	96	96.2427
10^3	97	96.8331
10^4	103	102.5501
10^5	148	148.0377
10^6	369	368.6482

Table 7.1: *Comparing modelled and theoretical fundamental frequencies for a string on an elastic foundation.*

which for a fixed time step T requires

$$R_s = \frac{2GT^2}{4\rho - GT^2},$$

with spatial step

$$\Delta = \sqrt{\frac{4T^2F}{4\rho - GT^2}}.$$

Notice that it is quite clear that when the stiffness $G = 0$ we reduce to the case for a waveguide string where $R_s = 0$ and $\Delta = Tc$ for string wave speed $c = \sqrt{F/\rho}$.

We carried out a simulation for a string of length $L = 0.5m$ with density $0.2kg/m^2$ held at tension $1850N/m$. The frequencies of vibration may be calculated from

$$f_n = \frac{c}{2\pi}\left[\left(\frac{n\pi}{L}\right)^2 + \frac{G}{F}\right]^{\frac{1}{2}}. \tag{7.2}$$

Shown in Table 7.1 are the modelled and theoretical fundamental frequencies for various values of the stiffness parameter G. Furthermore we also examine the dispersion properties by considering the positions of the resonant modes. Shown in the left hand plot Figure 7-1 is a plot of frequency against wavenumber for our model. The curves represent models for $G = 0$ to $G = 10^5$, where the lowest of the curves represents $G = 0$, while the highest curve represents $G = 10^5$. The fundamental frequency is that where the wave number is one and it clearly increases with increasing stiffness. We compare this graph to that of Figure A-4. At first the graphs have zero gradient, but then each curve tends towards a straight line representing a harmonic sequence. We note that for low values of stiffness G, the limiting line is that of the the same string in the absence of foundation stiffness. In fact, the curves for $G = 0$ to $G = 10^3$ are not

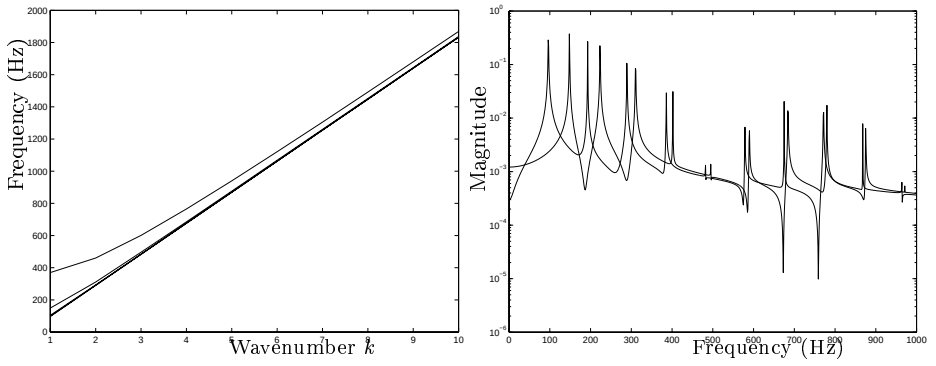

Figure 7-1: *Frequency versus wavenumber for waveguide on a bed of springs.*

individually visible on the plot. In the case where the stiffness is low, the output is dominated by the tension. However for higher spring stiffnesses, the shape of the curve will approach that of a string of a higher fundamental, rather than the fundamental of the string in the absence of foundation stiffness. The right hand plot of Figure 7-1 shows the frequency spectra of a standard waveguide and a waveguide placed on an elastic foundation. The curve with the lower fundamental is that of an ideal string. Note how the second curve has a higher fundamental frequency, but as frequency increases, the resonant modes of both systems align. This is in accordance with equation (7.2).

7.2 The string on a viscous sub-base

It is well documented that real strings exhibit losses which are roughly of a low-pass nature. What usually happens is that friction causes damping in the free vibrations, mainly at the higher end of the spectrum, and there is a slight change in the allowed frequencies. To characterise the losses correctly is not straightforward. Most of the energy is lost as heat to the surrounding air, while some goes into outgoing sound waves [33]. Losses can be added to a waveguide string model by including loss loop filters at the terminations of the waveguide. Using an IIR filter one can attempt to match the frequency dependent loss of a given material [27]. However, by considering methods to represent the linear viscoelastic response, we hope to provide a framework to construct more complicated damping models representing particular materials. We follow the work of Djoharian in [13, 14] and begin by reconsidering the ideas within a waveguide environment. The model we consider is one which represents a string on a purely viscous foundation as described in Appendix A.3. Although this does not introduce a frequency dependent loss it does show how we may represent simplified

internal friction. We hope to extend this idea to include more complicated linear viscoelastic responses in the future.

We note the equation of motion for a string on a viscous foundation as described in Appendix A.3.2 is

$$F\frac{\partial^2 u}{\partial x^2} - g\frac{\partial y}{\partial t} = \rho\frac{\partial^2 y}{\partial t^2}.$$

The proposed waveguide structure is similar to that of the previous section but we input a zero signal to the third port of each junction instead of attaching a self-loop. By doing this we are placing a *hole* at each junction, the size of which can be characterised by an input impedance R_d. Formally, for each junction j, the inputs are

$$\begin{aligned} V^+_{j,0}(n) &= V^-_{j+1,1}(n-1) \\ V^+_{j,1}(n) &= V^-_{j-1,0}(n-1) \\ V^+_{j,2}(n) &= 0. \end{aligned}$$

Now, setting the other impedances to R, giving a total junction impedance $R_J = 2R + R_d$ we manipulate the junction velocity equation as follows,

$$\begin{aligned} V_j(n+1) &= \frac{2}{R_J}\left[RV^+_{j,0}(n+1) + RV^+_{j,1}(n+1)\right] \\ &= \frac{2}{R_J}\left[RV^-_{j+1,1}(n) + RV^-_{j-1,0}(n)\right] \\ &= \frac{2}{R_J}\left[RV_{j+1}(n) + RV_{j-1}(n)\right] \\ &- \frac{2}{R_J}\left[RV^+_{j+1,1}(n) + RV^+_{j-1,0}(n)\right] \\ &= \frac{2}{R_J}\left[RV_{j+1}(n) + RV_{j-1}(n)\right] \\ &- \frac{2}{R_J}\left[RV^-_{j,0}(n-1) + RV^-_{j,1}(n-1) + R_dV^-_{j,2}(n-1)\right] \\ &+ \frac{2R_d}{R_J}V^-_{j,2}(n-1) \\ &= \frac{2R}{R_J}\left[V_{j+1}(n) + V_{j-1}(n)\right] - V_j(n-1) + \frac{2R_d}{R_J}V^-_{j,2}(n-1). \end{aligned}$$

By noting that $V^-_{j,2}(n-2) = V_j(n-2) - V^+_{j,2}(n-2) = V_j(n-2)$ we may now write the

waveguide as the following difference scheme,

$$\begin{aligned} V_j(n+1) - 2V_j(n) + V_j(n-1) &= \frac{2R}{R_J}\left[V_{j+1}(n) - 2V_j(n) + V_{j-1}(n)\right] \\ &+ \left(\frac{4R}{R_J} - 2\right) V_j(n) + \frac{2R_d}{R_J} V_j(n-1). \end{aligned}$$

Now

$$\frac{4R}{R_J} - 2 = \frac{4R}{R_J} - \frac{2(2R + R_d)}{R_J} = -\frac{2R_d}{R_J},$$

giving

$$\begin{aligned} V_j(n+1) - 2V_j(n) + V_j(n-1) &= \frac{2R}{R_J}\left[V_{j+1}(n) - 2V_j(n) + V_{j-1}(n)\right] \\ &- \frac{2R_d}{R_J}\left(V_j(n) - V_j(n-1)\right). \end{aligned}$$

This is entirely equivalent to a centered FDS for the governing equation by setting

$$\frac{2R}{R_J} = \frac{F}{\rho}\lambda^2, \qquad \frac{2R_d}{R_J} = \frac{g}{\rho}T,$$

where $\lambda = \frac{T}{\Delta}$ for time step T and spatial step Δ. To solve these equations we fix the time step, and set $R = 1$ giving,

$$R_d = \frac{2gT}{2\rho - gT}, \qquad \Delta = \sqrt{\frac{F}{\rho}}T\sqrt{\frac{2\rho}{2\rho - gT}}.$$

Note how in the absence of foundation viscosity when $g = 0$, then we have $R_d = 0$ and the spatial step is as in the case of a standard waveguide string where $\Delta = \sqrt{\frac{F}{\rho}}T$.

We may analyse this scheme by considering the spectral amplification factor $G(w)$, found by solving the quadratic

$$G^2 + BG + C = 0,$$

where $B = b^2T + 4a^2\lambda^2\sin^2(\frac{w}{2}) - 2$, $C = 1 - b^2T$, $a^2 = \frac{F}{\rho}$ and $b^2 = g/\rho$. We find that $B^2 - 4C < 0$ which means the amplification factor is always complex and thus we compute it's magnitude and phase. We find that the magnitude is represented by

$$|G(w)| = \sqrt{C} = \sqrt{1 - b^2T}.$$

We note that the magnitude is independent of frequency and that $|G| < 1$ whenever

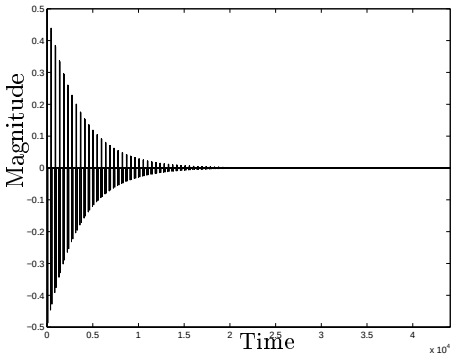

Figure 7-2: *Output from Viscous Waveguide with* $g = 5$.

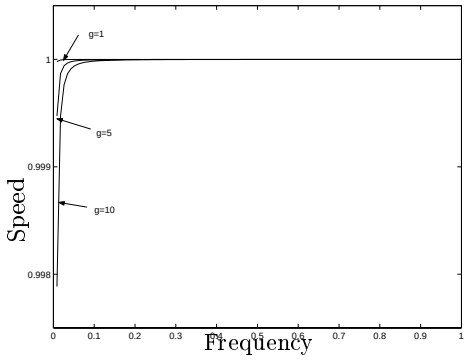

Figure 7-3: *Wave Speed on Viscous Waveguide.*

$g > 0$. Thus the damping acts evenly on all frequencies and increases with increasing g. Shown in Figure 7-2 is a plot of the output of a viscous waveguide when $g = 5$ shown in the time domain since we observed previously that damping will act evenly on all frequencies. We observe an exponential nature to the decay of the signal.

We may also examine the phase of the amplification factor and find that a small amount of additional dispersion is evident. Shown in Figure 7-3 are phase speed plots for viscous waveguides for three values of the viscosity parameter g. They show a small amount of dispersion where the wave speed will fall very slightly below the original waveguide wave speed of 1 spatial sample per time step. This deviation causes very little difference to the output signal as shown in Table 7.2 which shows that harmonicity is preserved.

It is also possible to combine the viscous waveguide model with the model of the previous section to model a string placed on a viscoelastic foundation, whose governing

n	f_n	f_n/f_1
1	96	1.00
2	193	2.01
3	289	3.01
4	385	4.01
5	483	5.03
6	578	6.02
7	674	7.02
8	769	8.01
9	867	9.03
10	964	9.03

Table 7.2: *Modelled modes for Viscous Waveguide with $g = 5$.*

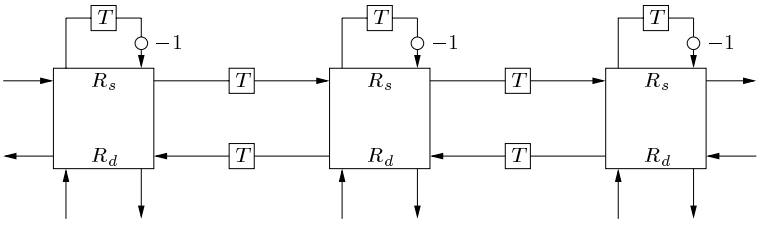

Figure 7-4: *Waveguide model for Viscoelastic String.*

equation is

$$F\frac{\partial^2 u}{\partial x^2} - g\frac{\partial u}{\partial t} - Gu = \rho\frac{\partial^2 u}{\partial t^2}.$$

This is equivalent to placing the string upon a foundation based upon parallel connections of springs and dampers called Voigt Units. The equivalent waveguide structure is described in Figure 7-4. Compare this to the diagram of the physical system in Figure A-5. In this instance the self loops and 'holes' are attached with respective impedances

$$R_s = \frac{2GT^2}{4\rho - 2gT - GT^2}, \qquad R_d = \frac{4gT}{4\rho - 2gT - GT^2},$$

and the spatial step is calculated from

$$\Delta = T\sqrt{\frac{4F}{4\rho - 2gT - GT^2}}.$$

This waveguide model and its corresponding physical system are analogous to the model for the transmission line equations described in [7, 8] in the constant coefficient

case.

Sounds from the model with damping only sound quite synthetic, since the damping is not frequency dependent, but the decay sounds seem reasonable. Sounds from the model with only an elastic foundation seem to add some modulation to the frequencies. In the future we hope to extend this simple model to include frequency dependent damping and we discuss some potential approaches in the next chapter.

Chapter 8

Conclusions and Future Research

In this chapter we provide a summary of the thesis, together with some possible avenues for future work. The thesis has provided some quite detailed descriptions and analyses of waveguide models of vibrating systems commonly found in musical instruments. We have described a simple waveguide model for a drum using waveguide structures for ideal wave propagation in air and across membranes. We pointed out that these ideal models were limited since they did not include phenomena such as stiffness or internal damping. Thus we went on to describe extended waveguide models for dispersive media such as stiff bars, strings, plates and membranes, as well as discussing a framework around which we could include internal damping. We now go on to describe further extensions which could improve the existing models. We then summarise the main results of the work and go on to discuss the limitations of the waveguide technique within the context of numerical modelling.

8.1 Suggestions for Future Research

8.1.1 Extensions to the Drum Model

There are many straightforward and immediate extensions that could be made to the drum model. In all cases the model is such that the basic structure would not change. First of all we note that in real tom-tom, side, or bass drums the two skins are typically held at different tensions and are of different thicknesses [15]. The variation in tension is simply implemented within the model framework and merely results in a different node density for the membrane mesh. Differences in thickness could be introduced, either by altering the density, or by replacing the ideal membrane meshes with stiff membrane meshes, described in section 6.2. The inclusion of a stiff membrane would also allow an investigation in to the effect of stiffness on the drum sounds. We also noted during

the course of chapter 4 that we would require fractional length delay lines to correctly model the size of the interior air, both at the circular boundary and at the interface. The interface method itself could be extended by considering its implementation near the circular boundary, which would certainly improve the accuracy.

It should also have become clear that we have not included a model for the shell of the drum. Such a shell would be typically made of wood or metal, and could be represented using the stiff plate model of chapter 6. The interface method already described could be used to model the passage of energy from the air to the shell and back. Using such a model we would be able to learn how important the shell is to the overall sound of the drum.

By using either a dodecahedral mesh or an interpolated mesh, we could improve the air mesh quite considerably. The interface process has been shown to be quite adaptable by its use in the modelling of a kettledrum in [27] where a dodecahedral mesh has been used to model sound propagation through the air within the kettle.

It is also clearly possible to model quite accurately air loading on a membrane by filling the surrounding air with an air mesh which may interact with the vibrating membrane through the interfacing technique.

Finally we note that since many musical instruments are made by hand using materials such as wood, that internal reflections will not always be specular, that is to say, diffusion will occur due to the rough nature of the surfaces. Such a phenomenon has been modelled successfully in [26] in 2D and could be extended to 3D for inclusion in the drum model.

8.1.2 Including other phenomena

Tension Modulation

In section 2.6 we discussed correcting dispersion error in a 2D waveguide mesh by replacing the units of delay with allpass filters. This structure could also be used to model the phenomenon of Tension Modulation. This is extremely important when observing the difference between a soft and vigorous pluck or strike of a string or membrane. When a string or membrane is displaced from its equilibrium it will necessarily have a larger than nominal length or area, and hence, due to stiffness of the material, there will be additional and time-varying tension. In strings this typically causes a time-varying fundamental frequency, where at first the fundamental increases, and then approaches the nominal frequency with time. It also causes generation of energy in the missing modes [29]. This is a phenomenon which has been accurately modelled in 1D for strings using time-varying FIR fractional delay filters in [49]. In this study the extra tension

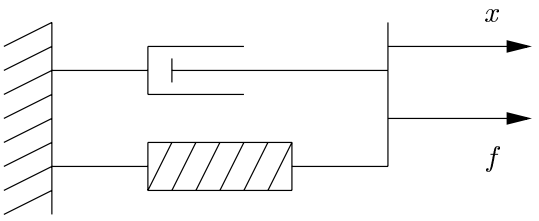

Figure 8-1: *The Voigt Unit.*

was commuted to the ends of the delay line and implemented using an FIR fractional delay filter. It is also possible to model this effect by using time-varying allpass filters placed between nodes in a digital waveguide [5]. Since the structure exists to place allpass filters between nodes in a waveguide mesh, an extension to model tension modulation in 2D should be possible. It is also important to note that it would not be possible to commute the extra tension to the edges of a 2D mesh, and the time-varying fractional delay filtering would have to be performed between nodes.

Frequency Dependent Damping

In chapter 7 we touched upon the need to represent a material's internal damping in order to fully represent the true sound of a material, and that this phenomenon was typically frequency dependent. It had been discussed and shown that a material's frequency dependent damping can be represented approximately in the linear case by series/parallel combinations of springs and dashpots [28, 38, 50]. The spring/dashpot models have a viscoelastic response which can be matched to the response of a real material. The model we presented in chapter 7 represented a string placed on a viscoelastic foundation whose response was of the simplest type called a Voigt Unit, described in Figure 8-1 as a parallel connection of a spring and dashpot. Another such foundation which could be considered would be based upon the Maxwell Unit, shown in Figure 8-2, to be a series connection of a spring and dashpot. Placing a string upon this type of foundation could mean that the damping would act in a manner dependent on the stiffness of the spring, and would hence introduce a frequency dependency. More complicated viscoelastic networks have been used in this way to model frequency dependent damping in [13, 14] and it could be possible to include such an approach within the waveguide framework using the procedure started in chapter 7.

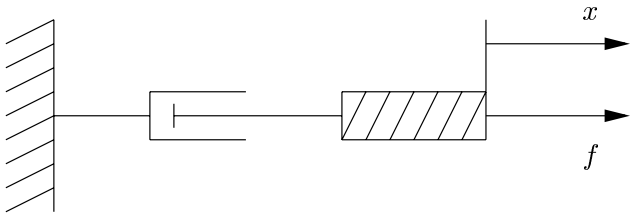

Figure 8-2: *The Maxwell Unit.*

Wooden Boards

Most musical instruments are made of wood, which presents an extra modelling problem. Disregarding the internal damping, the grain of the wood gives a directional property to the elastic constants which help describe the propagation of waves across a wooden surface. In theory, quarter cut wood boards are characterised by two Young's Moduli, two Poisson ratios and a shear modulus representing the different characteristics in line or against the grain of the wood [15]. A shear modulus can be introduced to a waveguide mesh plate model by considering the Mindlin plate theory, as opposed to the Euler-Bernoulli theory as described in [8]. Then the directional properties cause by the grain of the wood are quite easily covered in the waveguide domain by changing the impedance values. Bilbao [8] has shown how spatially varying material parameters can be incorporated into a waveguide model. For example, given a wooden plate with two Young's Moduli E_x and E_y, we could define two corresponding impedance values Y_x and Y_y in the plate model of chapter 6. Each horizontal input to a mesh scattering junction in the square would have input impedance Y_x, while each vertical input would have impedance Y_y.

Such a wooden board model could be used to model guitar or violin bodies, or the wooden shells found in drums.

8.2 Conclusions and Discussion

8.2.1 Thesis Summary

This thesis has presented a detailed description and analysis of the digital waveguide modelling technique when applied to physical systems representing vibrations of musical instruments. For each system considered, the model has been subjected to mathematical analysis, and then simulations have been presented where results have been explained and compared to expected theoretical output. In each case the physical theory has been separately described in the Appendix.

After an initial introduction to the concept and reasons for mathematical and nu-

merical modelling, and the waveguide modelling technique, we described in chapter 2 how to use the method in 2D to model a circular membrane, and considered improving the representation of the boundary where we concluded that the inclusion of *rimguides* was valid. At this stage we identified the problem of dispersion error, and introduced a novel method for correcting this inaccuracy using a filtered mesh. This work was carried out independently from similar work described in [17].

In chapter 3 we considered extensions of the waveguide mesh technique to 3D. Again we analysed the model mathematically and compared theoretically two mesh structures by examining their dispersion errors. We then used the two meshes in simulations of two acoustic spaces and discussed the accuracy of the models. We concluded that *rimguides* should in general improve the boundary resolution for arbitrarily shaped enclosures. We also concluded that in general a dodecahedral mesh structure should be used for accurate 3D acoustics simulations, but in some cases, due to the shape of the boundary of the space, it may be sufficient to use a 3D rectilinear mesh.

Having introduced and analysed models for sound wave propagation in 1D, 2D and 3D we described a model for a drum in chapter 4. It was proposed that the model should be constructed by representing drum skins by 2D waveguide meshes, and the internal air enclosed by the drum by a 3D waveguide mesh. Thus a method which interfaces 2D and 3D meshes was described. In this work, the method was applied to a new model for a tom-tom drum, and an analysis of the interfacing technique was presented. This showed that the model behaved encouragingly in accordance with theoretical and physical observations of real drums, and in particular, that the effect of the internal air load was represented.

By this point it was well established that waveguides and waveguide meshes could be applied to musical instrument modelling, but that simplifications in the underlying vibrating systems meant that considerations of such phenomena as stiffness and internal damping had been ignored. Following the work begun by Stefan Bilbao [8] we showed in chapter 5 how it was possible to extend the waveguide technique to models of stiff bars. We presented an analysis of the model and its output. We found that the models suffered from a dispersion error where accuracy decreased with increasing frequency. This was confirmed in the simulation. We then went on to describe an extension to the model for a stiff string, again analysing the model mathematically, and from the output of a simulation. We showed that the model behaved as expected for some experimental simulation values for steel guitar strings. We were able to demonstrate the inharmonicity encountered for thick, low frequency strings. This inharmonicity is countered in real guitars by forming the thicker, lower frequency strings, by wrapping one string around a central core. We then showed in chapter 6 that these models could

be extended to 2D to represent stiff plates and stiff membranes. These models were described and analysed for different mesh geometries by comparing their dispersions. We found that errors in these models were larger than those found in the for the corresponding 1D methods. This was because the phase errors of both the stiff 1D models and the standard 2D waveguide mesh models of chapter 2 were combined. Thus to obtain the same level of accuracy in the 2D case we would need a higher sampling resolution.

Finally, in chapter 7 we began an approach to the problem of including a material's internal damping. We described that this could be quite complex and discussed a new approach to including this phenomenon in waveguide models by considering a simple example. The work has so far concentrated on the simplest cases and we hope that the underlying principle could be extended to provide accurate frequency dependent damping models of real materials.

This thesis provides much practical advice on the use of digital waveguides for musical instrument models. For example we set out criteria for using a 2D waveguide mesh and a filtered mesh for membrane simulations, describing the boundary problem and the method of rimguides to correctly model a circular boundary. We discussed 3D waveguide meshes for use in simulations of cubic, rectangular and cylindrical enclosures and described and evaluated the boundary problem. We went on to describe a model for a drum and discussed extended mesh structures which would then need to be incorporated to yield more physically realistic models and models for complete musical instruments. The thesis could be thought of as a description of the building blocks required to build complete instrument models, which can be glued together using the interfacing technique described in chapter 4. Thus a complete virtual instrument builder could be developed which could help in the analysis of existing instruments, or indeed the design of entirely new ones.

8.2.2 Contributions of the Author

In chapter 2 a method was described by which the dispersion error in a 2D waveguide mesh could be corrected using embedded allpass filters. This method was devised by the author entirely independently of similar work carried out in [17]. The analysis presented in this thesis contains more detail. It was shown how to calculate the dispersion of the filtered mesh, and we pointed out that the presence of the filters introduced some direction dependence in the dispersion error. Simulations were carried out and it was noted that the directional dependence of the dispersion error was causing some of the higher frequencies to be poorly resolved, contributing double peaks in frequency spectrum. This issue was not discussed in the alternative work, where the output

signals were also low-pass filtered. An alternative performance analysis was described in this thesis which helped conclude that the filtered mesh would successfully decrease the effect of dispersion over a useful bandwidth, without increased computational cost over a standard waveguide mesh operating at an increased sample rate. However the issue of spatial resolution (the filtered mesh will have fewer nodes than the unfiltered mesh at the same sample rate) against temporal resolution is left to the discretion of the reader.

In chapter 3 we discussed the use of 3D waveguide meshes for the simulation of acoustic spaces. A performance analysis of the method was given which has not been previously presented in the literature. In particular we discuss the use of *rimguides* to correctly model the boundary in cubic, rectangular, and cylindrical enclosures using both square and dodecahedral meshes. Previous work had detailed only the performance of square and tetrahedral meshes for use with rectangular enclosures [41, 56]. The dodecahedral mesh has been previously defined in [18] and used in the model of a tympani drum [27] but we include a detailed performance analysis. Furthermore we have been able to identify the boundary problem, and give recommendations for use of waveguide meshes in the simulation of acoustic spaces.

In chapter 4 we introduced a method by which we may interface 2D and 3D waveguide meshes and applied the technique by building a model for a tom-tom drum. The development of this model was carried out by the author in conjunction with Joel Laird [27]. The use of the method in the model of a tom-tom drum was a novel implementation in this thesis. Also, the performance analysis presented in this thesis has not been discussed elsewhere.

In chapter 5 and 6 we discussed extensions to the waveguide method to include modelling dispersive media such as bars, stiff strings, plates and stiff membranes. First of all, a 1D waveguide model for the Euler-Bernoulli bar was given. This was taken from [8] but in this thesis we analysed the dispersion error and provided a numerical analysis of the output of such a model. This has not been previously reported where performance analysis had been presented pictorially [8]. The consequent extension of the 1D bar model to a model for a stiff string was derived entirely by the author. In chapter 6 we extended the Euler-Bernoulli bar model to 2D in order to model a stiff plate. This was a novel extension and we also included a numerical performance analysis and dispersion error comparisons not previously reported for 2D plate models. The subsequent extension of this plate model to a model for a stiff membrane was also a new model devised in this thesis.

Finally, in chapter 7 we proposed a novel method for introducing damping into a waveguide model. We showed how the method can be used to introduce additional dis-

persion and non-frequency dependent damping in a model for a string on a viscoelastic foundation. We conjectured how more complicated visco-elastic responses could be introduced within a novel framework for incorporating material specific damping.

8.2.3 Conclusions

Having been introduced to the waveguide modelling method the question arises as to how this method compares to existing methods such as finite differences (FDS) and finite elements (FEM). In this thesis we extended the waveguide modelling technique and the next step would be to perform a detailed comparison analysis with the other methods. There are no directly comparable published studies but some points of discussion do come readily to hand.

The waveguide method in its basic form, such as the standard waveguide meshes or the waveguide models for dispersive media presented in this thesis, is entirely an alternative implementation of a centred FDS in terms of wave variables, and to that end a direct comparison is quite straightforward. A simple calculation of the computational requirements show that the waveguide formulation is certainly heavier. For example, if we consider the 2D triangular waveguide mesh of chapter 2 we find that calculation of velocity at a waveguide scattering junction will require some 12 additions and 1 multiplication. The corresponding calculation in the FDS domain requires merely 7 additions and 1 multiplication. Furthermore, the waveguide method will require 7 memory locations per node, while the FDS requires only 1. Such a calculation immediately casts doubt on the waveguide method as a modelling technique.

Originally the digital waveguide method was developed for use in 1D real time synthesis and its uses have been well documented, and this thesis in part sought to push the technique onwards towards 2D and 3D models and models which represent more complicated physical behaviour, for example, frequency dependent wave speed. In particular we wanted to apply the 2D and 3D mesh modelling techniques and examine their accuracy and suitability for acoustic simulation, especially when applied to complete musical instrument models. We sought to extend the complexity of the models in order to improve accuracy, in the case of the 2D membrane, and in order to model systems other than those representing ideal wave propagation. In the original 1D waveguide formulation, casting the FDS as a waveguide, that is, as a pair of bi-directional delay lines, meant that signal processing techniques such as digital filtering could be applied to simulate certain effects like dispersion or damping. We have seen in this thesis that some of these ideas can be used for accurate modelling in 2D waveguide meshes when we described an allpass filtered mesh with improved dispersion characteristics. In this case we have used the waveguide formulation of the FDS in order to apply signal

processing techniques and improve accuracy without increasing computational burden.

It is possible to argue in favour of the waveguide formulation over its FDS alternative. The first case in point refers to the level of intuition and understanding. When applying the waveguide method to simple wave propagation in 1D, 2D and 3D the use of scattering methods gives a uniquely physical approach. Implementation as waves travelling down certain routes and scattering at junctions according to a simple rule is certainly more intuitive to the lay-man than a numerical version of a mathematical equation. However this level of intuition degrades when we consider the dispersive models of chapters 5 and 6 where the method performs less accurately.

One may also argue that, when designing a model for a given system, ensuring numerical stability in a waveguide formulation will require only that each junction be passive. In this instance we merely require each waveguide impinging upon a scattering junction to have positive impedance.

In this thesis we also described how we may define an interface between a 2D and 3D waveguide mesh. By doing this we were able to model a drum where coupling occurs between the membrane and the surrounding air. In order to provide a similar interface using just FDSs we would have to define a constitutive set of equations for both membrane and the air within and without the drum with additional constraints at the interface. These constraints would ensure that the velocity of the membrane was the same as the velocity of air at the boundary of each air filled enclosure. Such a set of equations has been defined in [30]. Then finite differences would have to be applied to this set of equations. Thus the waveguide formulation has offered a simpler and more intuitive approach just by connecting models which represent the individual components of the drum.

It has been reported that it is also possible to interface waveguide meshes of different densities in the same dimension [8, 27]. This allows for a more careful application of the mesh near areas of interest, such as corners. Furthermore the use of *rimguides*, again an application of digital filters, allow more careful boundary shape resolution without requiring an adaptive or denser mesh structure near the boundary. This is possible using FDSs but it is not straightforward for 2D stationary grid methods. Here, the reformulation of the FDS as a waveguide mesh, has again allowed us to use a signal processing technique in order to improve the quality of the simulation, without resorting to a new FDS.

However, the issue of damping in waveguide models of musical instruments has not yet been adequately addressed. We have seen how simple losses can be introduced to the waveguide and discussed how more complicated linear viscoelastic behaviour could be included, but these issues would need to be resolved. In FDS models of stiff strings

and bars [11, 10], damping has been introduced by adding viscous terms to the PDEs in the form of mixed derivatives, and a centred FDS applied to this equation. It is unclear whether there exist equivalent waveguide formulations of these FDSs. This opens the question: if a waveguide model corresponds to a centred FDS, does a FDS have an equivalent waveguide formulation? The likely negative answer to this question introduces a limitation of the waveguide method, where the class of all FDSs is a much larger set that that of all the waveguide models. On the other hand, the filtered waveguide mesh discussed in chapter 2 will not be equivalent to a centred FDS and its advantages have been discussed.

We have seen that the digital waveguide method is an alternative implementation of centred FDS and as such certain advantages have been described. However we have also seen that these schemes suffer badly from phase error. Another modelling technique which is commonly used and which suffers less from phase errors is the Finite Element Method (FEM). A model for a drum had also been presented using a FEM [30]. The model was for a tympani drum and was achieved by defining a set of coupled equations as was described previously, and then applying finite elements. The model produces excellent results when compared to a real tympani drum. This model was compared to a waveguide model in [27]. The results show that the FEM is certainly more accurate, and does not suffer from dispersion error. Each model was analysed by comparing output from the tympani membrane. The FEM method offers excellent accuracy over the 12 modes, while the waveguide method shows a considerable mis-tuning of the first two modes, and while the next 10 modes are more accurately represented, it is clear that dispersion error is occurring. It should be noted however, that the waveguide model represents only the interaction of the membrane with the interior air of the drum, and that the air load from outwith the drum had not been modelled. This would cause a decrease in the fundamental modes of vibration [15], and thus the mistuned fundamental observed in the waveguide model could be corrected. Also, designing a FEM model is a much more involved process. The process of deriving the coupled equations and the element method would require good mathematical knowledge. On the other hand, the waveguide technique provides a modular representation of the drum, connecting simple structures (the membrane model of chapter 2 and the cylindrical air cavity of chapter 3) together, thus each element can be manipulated separately, for example, replacing the membrane with a stiff membrane model.

Also in the FEM paper they show output when applied just to the membrane. We have shown similar accuracy with our filtered mesh, although a comparison of computational requirements and speed has not been made and would require further study. An FEM has also been used to model a vibrating bar in [9], however in this case

the elements were three-dimensional, and the method was based on a 3D model of the material, and thus a comparison with our FDS model is not possible.

It has been remarked [45] that the benefit of finite element methods over FDS methods is that one can create a denser mesh structure where required, say at boundaries, and that they are more suitable when modelling coupled models, where various wave propagation media are connected. We have shown in this thesis that more accurate modelling of the boundary can be achieved with regular grids, and without increasing mesh density. Furthermore, by describing a simple drum model, we have shown that interfaces between different meshes is also possible. However the performance of the interface is compromised by the low order of interpolation. Furthermore, the interface method will need to be extended to cope with areas such as that near the circular boundary in the drum model.

In this thesis we have shown that it is possible to extend the standard digital waveguide methods to model wave propagation in dispersive media such as bars, stiff strings, plates and membranes. We have also shown that the method is accurate enough to demonstrate phenomena observed in real instruments. However, it is the view of the author that the method is still a little too simplistic to be used as an accurate modelling tool. For example, the results in chapters 5 and 6 show that errors can be quite large despite qualitative similarities between the behaviour of the model and the theoretical system. The underlying FDS is quite basic and suffers greatly from dispersion error. Errors for the 2D plate model show that dispersion error inherent in 2D waveguide mesh models for the standard wave equation are inherited in the 2D plate model. This is demonstrated by poor performance. Since the 2D plate model involves two coupled interleaved waveguide meshes, it is unclear whether this dispersion error could be corrected by the use of digital filters. Again, the use of an implicit FDS or FEM could give improved performance, although an explicit FDS employed at a lower resolution can produce quite good results [11], and thus we could similarly employ a waveguide implementation.

We have extended the waveguide modelling technique to perform more than had been done before. We sought to use the method as a modelling tool rather than as a synthesis method. We designed and described extensions to the method to cope with more complicated systems and concluded that the technique offers an alternative perspective of the FDS method and showed that by using waveguides we could approach modelling in a different manner. However, the underlying FDSs are quite simple.

Waveguides have been extended in this thesis beyond their original use for modelling ideal wave propagation to models for dispersive media. It is also been shown how they can be used to design complete instrument models. They offer an alternative and

valid perspective on centred FDSs. They utilise signal processing techniques implied by their digital travelling wave implementation, such as was shown in the method of rimguides, the allpass filtered mesh and the interface technique. However various limitations have been encountered which have indicated that the method could not be used for highly accurate musical instrument models. For example, the order of interpolation in the interface method is zero order, with a resultant loss of accuracy, the underlying centred FDSs suffer greatly from phase error, and thus high sample rates are required (particularly in 2D and 3D), and the inclusion of damping has not yet been satisfactorily addressed. In the absence of a definitive comparison, it seems that, while methods such as FEM would yield the most accurate models, the waveguide method could be used to design simple prototype models which highlight certain phenomena, while remaining more amenable to direct manipulation.

Appendix A

The Physics Of Musical Instruments

In this appendix we include mathematical details of the physical systems described throughout the thesis. All of the dynamical systems described here are also detailed in such texts as [15, 20, 21, 33, 38].

A.1 The Ideal Wave Equation in 1D, 2D and 3D

A.1.1 Derivation and solution of the 1D Wave Equation

Consider a small element of a string which is held under tension F as shown in Figure A-1. In the following derivation we assume the only restoring forces are due to tension, that there is no external force and no friction. The resultant equation of motion in the vertical direction is thus

$$F\sin(\theta_{x+dx}) - F\sin\theta_x = \rho ds\frac{\partial^2 u}{\partial t^2},$$

where ρ represents the density per unit length. By assuming small deflections, we may write $ds \approx dx$. The same assumption allows us to write $\theta \approx \sin\theta$ for small θ and $\theta \approx \frac{\partial u}{\partial x}$. Hence the equation of motion may be approximated as

$$\begin{aligned} F\left(\theta_{x+dx} - \theta_x\right) &= \rho dx\frac{\partial^2 u}{\partial t^2} \\ \Rightarrow F\frac{\partial\theta}{\partial x} &= \rho\frac{\partial^2 u}{\partial t^2} \\ \Rightarrow F\frac{\partial^2 u}{\partial x^2} &= \rho\frac{\partial^2 u}{\partial t^2}. \end{aligned}$$

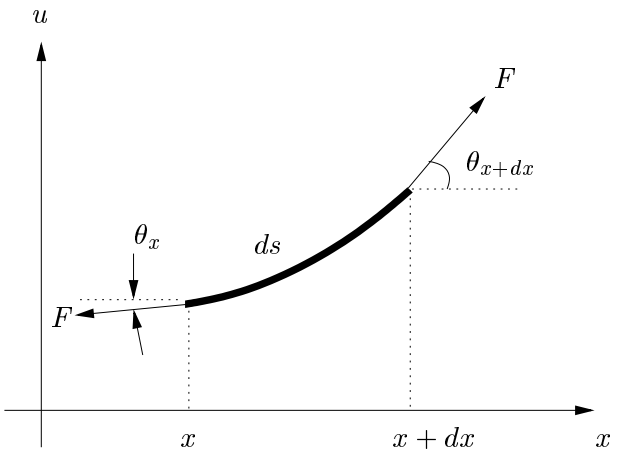

Figure A-1: *Segment of a string held under tension F*

Writing $c^2 = \frac{F}{\rho}$ gives us the standard form for the 1D wave equation representing transverse displacement on an ideal string.

$$\frac{\partial^2 u}{\partial t^2} = c^2 \frac{\partial^2 u}{\partial x^2}.$$

A.1.2 Solving the 2D Wave Equation for a Circular Membrane

The 2D wave equation describes transverse wave propagation on an ideal membrane and may be written as

$$\frac{\partial^2 u}{\partial t^2} = c^2 \left(\frac{\partial^2 u}{\partial x^2} + \frac{\partial^2 u}{\partial y^2} \right),$$

where $u(t, x, y)$ represents vertical displacement, $c = \sqrt{\frac{F}{\rho}}$, F is tension per unit length of the membrane and ρ its superficial density.

For a circular membrane, we consider solving the above equation in polar coordinates. By writing $x = r\cos\phi$ and $y = r\sin\phi$ we have

$$\frac{d^2 u}{dt^2} = c^2 \left(\frac{d^2 u}{dr^2} + \frac{1}{r}\frac{du}{dr} + \frac{1}{r^2}\frac{d^2 u}{d\phi^2} \right).$$

Writing the solution in the form $u(r, \phi, t) = R(r)\Phi(\phi)e^{iwt}$ gives the simultaneous equa-

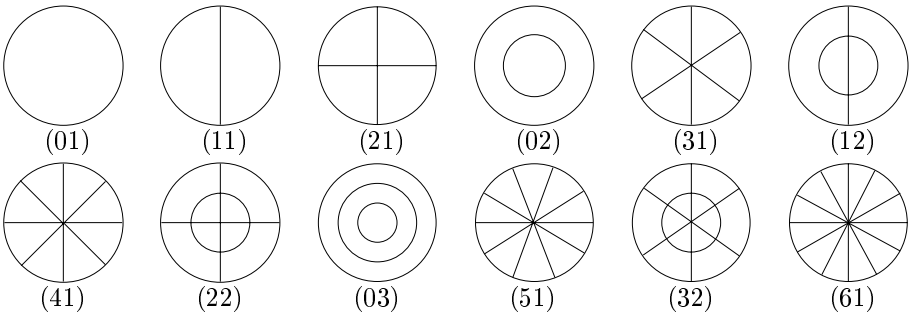

Figure A-2: *First 12 modes of the ideal circular membrane.*

tions,

$$\frac{d^2R}{dr^2} + \frac{1}{r}\frac{dR}{dr} + \left(\frac{w^2}{c^2} - \frac{m^2}{r^2}\right)R = 0$$
$$\frac{d^2\Phi}{d\phi^2} + m^2\Phi = 0.$$

The solution of second equation is $\Phi(\phi) = Ae^{\pm im\phi}$. The first equation is a form of Bessel's Equation

$$\frac{d^2y}{dx^2} + \frac{1}{x}\frac{dy}{dx} + \left(1 - \frac{m^2}{x^2}\right)y = 0,$$

with $y = R$ and $x = kr$. The solutions are Bessel Functions of order m. Each of these functions $J_0(x), J_1(x), ..., J_m(x)$ has several zeros and it is these zeros which characterise the allowed frequencies. Writing the nth zero of $J_m(x)$ as j_{mn} then we have $k_{mn} = j_{mn}/r$ and using the relationship $k = w/c$ we may write the allowed frequencies as

$$f_{mn} = j_{mn}\frac{c}{2\pi r}$$

for $m, n \in \mathbb{N}$. The frequency of the (m, n) mode is characterised by m nodal diameters and n nodal circles (including one at the boundary) and these are shown in Figure A-2. Mode frequencies can be calculated using tables of Bessel Functions like those given in [57].

Membrane Impedance

The concept of wave impedance for a string was discussed in chapter 1. For a membrane it is not possible to define an analogous quantity since a finite force applied to an interior point of the membrane will produce an infinite deflection [33]. To show this we consider the static deflection of a circular membrane subjected to a transverse force P,

distributed evenly over a circular area of radius s at the centre of the membrane. The equation for the static deflection u is

$$\frac{d^2u}{dr^2} + \frac{1}{r}\frac{du}{dr} + \frac{1}{r^2}\frac{d^2u}{d\phi^2} = \begin{cases} -\frac{P}{\pi s^2 F} & 0 \leq r < s \\ 0 & s < r \leq R \end{cases}$$

Solving this gives for the deflection u gives

$$u = \begin{cases} \frac{P}{2\pi F}\left[\ln\frac{R}{s} + \frac{1}{2s^2}(s^2 - r^2)\right] & 0 \leq r < s \\ \frac{P}{2\pi F}\ln\frac{R}{r} & s < r \leq R \end{cases}$$

Thus the displacement of the region of application of the force goes to infinity as $s \to 0$, as we approach a point driving force, and this will happen no matter how small the driving force P is compared to the tension F, since the deflection can be made as large as we wish by concentrating it on a smaller area.

A.1.3 The Wave Equation in 3D

Three dimensional wave propagation may be characterised by the following equation of motion

$$\frac{\partial^2 P}{\partial t^2} = c^2\nabla^2 P, \tag{A.1}$$

where c is the speed of sound through the medium in question, while the pressure P depends upon position and time.

Finding Resonant Modes of a Rectangular Room

In Cartesian coordinates equation A.1 is written as

$$\frac{\partial^2 P}{\partial t^2} = c^2\left(\frac{\partial^2 P}{\partial x^2} + \frac{\partial^2 P}{\partial y^2} + \frac{\partial^2 P}{\partial z^2}\right). \tag{A.2}$$

If the boundary surface is perfectly rigid, then the boundary conditions are that $\frac{\partial P}{\partial x} = 0$ at $x = 0$ and $x = L_x$, $\frac{\partial P}{\partial y} = 0$ at $y = 0$ and $y = L_y$ and $\frac{\partial P}{\partial z} = 0$ at $z = 0$ and $z = L_z$.

We separate variables by considering a solution of the form $P(x, y, z, t) = X(x)Y(y)Z(z)T(t)$ in a rectangular room of length L_x, width L_y and height L_z. Inserting this solution into equation A.2 yields

$$\frac{1}{T}\frac{\partial^2 T}{\partial t^2} = c^2\left(\frac{1}{X}\frac{\partial^2 X}{\partial x^2} + \frac{1}{Y}\frac{\partial^2 Y}{\partial y^2} + \frac{1}{Z}\frac{\partial^2 Z}{\partial z^2}\right).$$

Now for this equation to hold both sides must be equal to a constant which we set to $-w^2$ to give

$$\begin{aligned}\frac{\partial^2 T}{\partial t^2} + w^2 T &= 0 \\ \frac{1}{X}\frac{\partial^2 X}{\partial x^2} + \frac{w^2}{c^2} &= -\frac{1}{Y}\frac{\partial^2 Y}{\partial y^2} - \frac{1}{Z}\frac{\partial^2 Z}{\partial z^2}.\end{aligned}$$

The first of these has the solution $T(t) = A_t \sin(wt) + B_t \cos(wt)$, while, as before, in the second equation both sides must be equal to a constant, k_1^2. This gives two more equations to deal with. Firstly we have

$$\frac{\partial^2 X}{\partial x^2} + \left(\frac{w^2}{c^2} - k_1^2\right) X = 0,$$

resulting in a solution, $X(x) = A_x \sin\sqrt{\frac{w^2}{c^2} - k_1^2}x + B_x \cos\sqrt{\frac{w^2}{c^2} - k_1^2}x$. Secondly we have

$$\frac{1}{Y}\frac{\partial^2 Y}{\partial y^2} + k_1^2 = -\frac{1}{Z}\frac{\partial^2 Z}{\partial z^2}.$$

Once more, this must be a constant, which we set as $-k_2^2$ to yield

$$\begin{aligned}\frac{\partial^2 Y}{\partial y^2} + (k_1^2 - k_2^2)Y &= 0 \\ \frac{\partial^2 Z}{\partial z^2} + k_2^2 Z &= 0.\end{aligned}$$

The first of these equations has the solution $Y(y) = A_y \sin\sqrt{k_1^2 - k_2^2}y + B_y \cos\sqrt{k_1^2 - k_2^2}y$ and the second has solution $Z(z) = A_z \sin(k_2 z) + B_z \cos(k_2 z)$.

We may determine the allowed frequencies by introducing the boundary conditions. Firstly $\frac{dX}{dx}(0) = 0$ gives $A_x = 0$, then

$$\frac{dX}{dx}(L_x) = -B_x \sin\sqrt{\frac{w^2}{c^2} - k_1^2}L_x = 0,$$

gives us $\sqrt{\frac{w^2}{c^2} - k_1^2} = \frac{l\pi}{L_x}$, where $l \in \mathbb{Z}$, so that $X(x) = B_x \cos\frac{l\pi x}{L_x}$.

Next, $\frac{dY}{dy}(0) = 0$ gives $A_y = 0$ and

$$\frac{dY}{dy}(L_y) = -B_y \sin\sqrt{k_1^2 - k_2^2}L_y = 0.$$

This means that $\sqrt{k_1^2 - k_2^2} = \frac{m\pi}{L_y}$, with $m \in \mathbb{Z}$ and $Y(y) = B_y \cos\frac{m\pi y}{L_y}$.

Finally the condition $\frac{dZ}{dz}(0) = 0$ gives $A_z = 0$ and $\frac{dZ}{dz}(L_z) = 0$ gives

$$\frac{dZ}{dz}(L_z) = -B_z \sin(k_2 L_z) = 0$$

and hence $k_2 = \frac{n\pi}{L_z}$, for $l \in \mathbb{Z}$ and $Z(z) = B_z \cos \frac{n\pi z}{L_z}$.

The gives a general solution which is a superposition of solutions of the form

$$P_{lmn}(x, y, z, t) = \cos \frac{l\pi x}{L_x} \cos \frac{m\pi y}{L_y} \cos \frac{n\pi z}{L_z} (A \sin(wt) + B \cos(wt)).$$

The allowed frequencies may be calculated by examining the expressions derived above for k_1 and k_2 giving

$$\begin{aligned} w_{lmn} &= c\pi \left(\frac{l^2}{L_x^2} + \frac{m^2}{L_y^2} + \frac{n^2}{L_z^2} \right)^{\frac{1}{2}} \\ f_{lmn} &= \frac{w_{lmn}}{2\pi}. \end{aligned} \tag{A.3}$$

Finding Resonant Modes of a Cylindrical Air Cavity

For a cylindrical column of air closed at both ends we consider re-writing equation A.1 in cylindrical coordinates. Putting $x = r\cos\phi$, $y = r\sin\phi$ and leaving z results in the following form for the 3D wave equation.

$$\frac{1}{r}\frac{\partial}{\partial r}\left(r\frac{\partial P}{\partial r}\right) + \frac{1}{r^2}\frac{\partial^2 P}{\partial \phi^2} + \frac{\partial^2 P}{\partial z^2} = \frac{1}{c^2}\frac{\partial^2 P}{\partial t^2}. \tag{A.4}$$

As usual we consider separation of variables by writing the solution as $P(r, \phi, z, t) = R(r)\Phi(\phi)Z(z)e^{-iwt}$. Substitution in A.4 gives

$$\begin{aligned} \frac{1}{r}\left(\frac{\partial R}{\partial r} + r\frac{\partial^2 R}{\partial r^2}\right)\Phi Z + \frac{1}{r^2}RZ\frac{\partial^2 \Phi}{\partial \phi^2} + R\Phi\frac{\partial^2 Z}{\partial z^2} + \frac{w^2}{c^2}R\Phi Z = 0. \\ \frac{r^2}{R}\left(\frac{1}{r}\frac{\partial R}{\partial r} + \frac{\partial^2 R}{\partial r^2}\right) + \frac{1}{\Phi}\frac{\partial^2 \Phi}{\partial \phi^2} + \frac{r^2}{Z}\frac{\partial^2 Z}{\partial z^2} + \frac{w^2}{c^2}r^2 = 0 \\ \frac{1}{\Phi}\frac{\partial^2 \Phi}{\partial \phi^2} + \frac{r^2}{Z}\frac{\partial^2 Z}{\partial z^2} = -\frac{r^2}{R}\left(\frac{1}{r}\frac{\partial R}{\partial r} + \frac{\partial^2 R}{\partial r^2}\right) - \frac{w^2}{c^2}r^2. \end{aligned}$$

Now proceeding in a similar manner as before, we may assume that both sides of this equation are equal to a constant, $-k_1^2$, giving

$$\frac{1}{\Phi}\frac{\partial^2 \Phi}{\partial \phi^2} + \frac{r^2}{Z}\frac{\partial^2 Z}{\partial z^2} = -k_1^2,$$

which can in turn be written as

$$\frac{1}{\Phi}\frac{\partial^2\Phi}{\partial\phi^2} = -\frac{r^2}{Z}\frac{\partial^2 Z}{\partial z^2} - k_1^2 = -k_2^2, \tag{A.5}$$

where k_2^2 is a constant. Now, since Φ has to have the same value at $\phi = 0$ and $\phi = 2\pi$, we must have k_2 as an integer, m, say, so that

$$\frac{\partial^2\Phi}{\partial\phi^2} + m^2\Phi = 0. \tag{A.6}$$

Equation A.5 also gives us the following differential equation for Z

$$\begin{aligned} \frac{\partial^2 Z}{\partial z^2} + \frac{(k_1^2 - m^2)}{r^2}Z &= 0 \\ \Rightarrow \frac{\partial^2 Z}{\partial z^2} + k_z^2 Z &= 0 \end{aligned} \tag{A.7}$$

Returning to the separated equation we also have

$$\begin{aligned} \frac{1}{r}\frac{\partial R}{\partial r} + \frac{\partial^2 R}{\partial r^2} + \left(\frac{w^2}{c^2} - \frac{k_1^2}{r^2}\right)R &= 0 \\ \Rightarrow \frac{1}{r}\frac{\partial R}{\partial r} + \frac{\partial^2 R}{\partial r^2} + \left(k_w^2 - \frac{m^2}{r^2}\right)R &= 0, \end{aligned} \tag{A.8}$$

where $k_w^2 = k^2 - k_z^2$, with $k = \frac{w}{c}$.

Now, equation A.6 has solutions $\Phi(\phi) = \cos(m\phi)$ or $\Phi(\phi) = \sin(m\phi)$, while equation A.7 has solutions of the form $Z(z) = A_z \sin k_z z + B_z \cos k_z z$. Equation A.8 is a form of Bessel's Equation, whose solutions are Bessel functions of order m, namely $J_0(k_w r), \ldots, J_m(k_w r)$.

We are now able to calculate the allowed frequencies for the complete solution. Given a cylinder height h, the boundary condition $\frac{dZ}{dz}(0) = \frac{dZ}{dz}(h) = 0$ implies that $k_z = \frac{l\pi}{h}$ with $l \in \mathbb{Z}$ and $Z(z) = B_z \cos k_z z$. Now proceeding in a similar manner to that of the circular membrane we must solve $\frac{dR}{dr}(a) = 0$, where a is the radius of the cylinder. Thus, the allowed values of k_w are $\frac{\alpha_{mn}}{a}$, where α_{mn} is the nth zero of the derivative of the mth Bessel function, J'_m. Consequently the allowed values of k are

$$k_{mnl} = \sqrt{\left(\frac{\alpha_{mn}}{a}\right)^2 + \left(\frac{l\pi}{h}\right)^2},$$

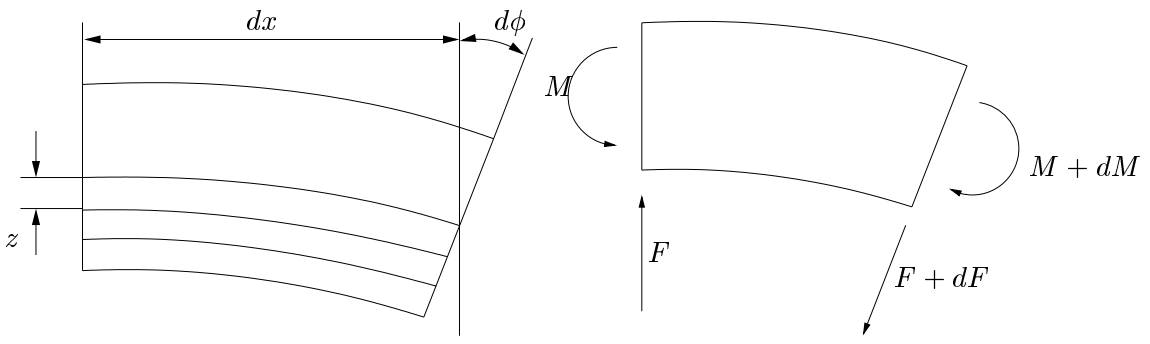

Figure A-3: *Forces acting on an ideal bar*

since $k^2 = k_w^2 + k_z^2$. Consequently the allowed frequencies are

$$w_{mnl} = c\sqrt{\left(\frac{\alpha_{mn}}{a}\right)^2 + \left(\frac{l\pi}{h}\right)^2}$$

$$\Rightarrow f_{mnl} = \frac{c}{2\pi}\sqrt{\left(\frac{\alpha_{mn}}{a}\right)^2 + \left(\frac{l\pi}{h}\right)^2}.$$

Finally the general solution can be formed as a superposition of functions of the form

$$P_{m,n,l}(r,\phi,z,t) = A \begin{matrix}\cos(m\phi)\\ \sin(m\phi)\end{matrix} J_m\left(\frac{\alpha_{mn}}{a}r\right)\cos\left(\frac{l\pi}{n}z\right)\cos(wt).$$

A.2 Bending Stiffness in Bars and Stiff Strings

A.2.1 Deriving the Euler-Bernoulli beam equation

An ideal bar differs from a string in the sense that it may vibrate freely under zero tension, with the restoring forces being supplied by elastic forces within the bar. To derive the equation of motion for the bar, consider a small segment of the bar of length dx. When the bar is bent, the outer part is stretched and the inner part is compressed, with a neutral axis whose length remains unchanged somewhere in between as shown in Figure A-3.

A filament located at a distance z below the neutral axis is compressed by an amount $z\frac{d\phi}{dx}$ and the total amount of force required to produce the strain (using Hooke's Law) is

$$Ez\frac{d\phi}{dx}dS,$$

where dS is the cross-sectional area of the filament and E is Young's Modulus. Hence

the total moment of this force about the central line is

$$dM = \left(Ez \frac{d\phi}{dx} dS \right) z,$$

giving the total moment to compress all the filaments as

$$M = \int dM = E \frac{d\phi}{dx} \int z^2 dS.$$

Now we may approximate $d\phi$ as the difference in the slope of the neutral axis at each end of the element so that

$$d\phi = -\left(\frac{\partial u}{\partial x} \right)_{x+dx} + \left(\frac{\partial u}{\partial x} \right)_x = -dx \left(\frac{\partial^2 u}{\partial x^2} \right),$$

where $u(x,t)$ is the transverse displacement of the bar. Then writing *moment of inertia* as $I = \sum z^2 dS$ we have a relationship between the total moment and the curvature

$$M = -EI \frac{\partial^2 u}{\partial x^2}.$$

The bending moment is not the same at every part of the bar, since it is proportional to curvature, so to keep the bar in equilibrium, the difference in the moments at each end of an element must be balanced by a shearing force whose moment is Fdx as shown in the right hand side of Figure A-3. Thus we have

$$\begin{aligned} Fdx &= (M + dM) - M = dM \\ \Rightarrow F &= \frac{\partial M}{\partial x} = -EI \frac{\partial^3 u}{\partial x^3}. \end{aligned}$$

The net force acting on the element dF, perpendicular to the bar's axis, can be written in terms of the forces acting at either ends of the element as

$$\begin{aligned} dF &= F_{x+dx} - F_x \\ &= dx \frac{F_{x+dx} - F_x}{dx} \\ &= dx \frac{\partial F}{\partial x}. \end{aligned} \tag{A.9}$$

So finally, the equation of motion, using Newtons second law, is

$$\begin{aligned} dx\frac{\partial F}{\partial x} &= \rho A\frac{\partial^2 u}{\partial t^2} \\ \Rightarrow \frac{\partial^2 M}{\partial x^2} &= \rho A\frac{\partial^2 u}{\partial t^2} \\ \Rightarrow \frac{\partial^2 u}{\partial t^2} &= -\frac{EI}{\rho A}\frac{\partial^4 u}{\partial x^4}. \end{aligned}$$

A.2.2 Bars with Fixed, Free, and Simply Supported Ends

We showed that the governing equation for a bar was

$$\frac{\partial^2 u}{\partial t^2} = -\frac{EI}{\rho A}\frac{\partial^4 u}{\partial x^4}.$$

We consider the existence of travelling wave solutions by trying harmonic solutions of the form $u = Ae^{i(kx-wt)}$, where w is the frequency of the harmonic wave which travels at speed $c = w/k$. Substitution in the governing equation gives the following relationship between k and w,

$$\begin{aligned} w &= \sqrt{\frac{EI}{\rho A}}k^2, \\ k &= \left(\frac{\rho A}{EI}\right)^{\frac{1}{4}}\sqrt{w}. \end{aligned}$$

Then, by either writing $y = Ae^{i\frac{w}{c}(x-ct)}$, or using $c = w/k$ e may write down a relationship between speed c and frequency w as

$$c(w) = \frac{w}{k} = \left(\frac{EI}{\rho A}\right)^{\frac{1}{4}}\sqrt{w}.$$

Thus we see that in a bar, the presence of bending stiffness introduces a frequency dependent speed of wave propagation which is proportional to $\sqrt{w}$.

To determine whether or not the bar may vibrate with simple harmonic motion (SHM), we consider solutions of the form $u = U(x)e^{-iwt}$. Doing this means we do away with the time derivative in the stiff wave equation which becomes

$$\begin{aligned} \frac{\partial^4 U}{\partial x^4} &= \frac{\rho A}{EI}w^2 U \\ &= k^4 U, \end{aligned}$$

where $k^4 = \frac{\rho A}{EI} w^2$.

The general solution of this equation is

$$\begin{aligned} U(x) &= c_1 e^{kx} + c_2 e^{-kx} + c_3 e^{ikx} + c_4 e^{-ikx} \\ &= a\cosh(kx) + b\sinh(kx) + c\cos(kx) + d\sin(kx), \end{aligned}$$

where $\cosh(\omega) = \cos(i\omega)$ and $\sinh(\omega) = -i\sin(i\omega)$. Thus the complete general solution for the stiff bar is

$$u(x,t) = \cos(wt + \Phi)\left(a\cosh(kx) + b\sinh(kx) + c\cos(kx) + d\sin(kx)\right).$$

The range of allowed frequencies will now be determined by the boundary conditions.

Supported at $x = 0$ and $x = L$

For a simply supported (or pinned) boundary we have displacement and curvature set to zero at the boundaries, that is

$$u(0,t) = \frac{\partial^2 u}{\partial x^2}(0,t) = u(L,t) = \frac{\partial^2 u}{\partial x^2}(L,t) = 0.$$

The boundary condition at $x = 0$ imposes that $a = c = 0$ and hence

$$\begin{aligned} U &= b\sinh(kx) + d\sin(kx) \\ \frac{\partial^2 U}{\partial x^2} &= k^2\left[b\sinh(kx) - d\sin(kx)\right]. \end{aligned}$$

Then the boundary conditions at $x = L$ now impose that

$$\begin{aligned} \sinh(kL) = \sin(kL) &= 0 \\ \Longrightarrow kL &= n\pi \\ \Longrightarrow k_n &= \frac{n\pi}{L}, \end{aligned}$$

which is the same requirement for k_n as for the ideal string. This time however, the allowed frequencies are

$$f_n = \frac{w_n}{2\pi} = \frac{\pi}{2L^2}\sqrt{\frac{EI}{\rho A}}n^2. \tag{A.10}$$

Clamped at $x = 0$ and $x = L$

For clamped edges we require both displacement and slope to be zero at the boundary, that is

$$u(0,t) = \frac{\partial u}{\partial x}(0,t) = u(L,t) = \frac{\partial u}{\partial x}(L,t) = 0.$$

The condition at $x = 0$ gives $c = -a$ and $d = -b$ so that now

$$\begin{aligned} U &= a\left[\cosh(kx) - \cos(kx)\right] + b\left[\sinh(kx) - \sin(kx)\right] \\ \frac{\partial U}{\partial x} &= ak\left[\sinh(kx) + \sin(kx)\right] + bk\left[\cosh(kx) - \cos(kx)\right]. \end{aligned}$$

Now for the boundary at $x = L$, $U(L) = 0$ gives

$$b = -a\left(\frac{\cos(kL) - \cosh(kL)}{\sin(kL) - \sinh(kL)}\right),$$

while $\frac{\partial U}{\partial x}(L) = 0$ gives

$$b = a\left(\frac{\sin(kL) + \sinh(kL)}{\cos(kL) - \cosh(kL)}\right).$$

Setting these two equal gives

$$\cos(kL)\cosh(kL) = 1,$$

which occurs for values $k_n L = \beta_n \pi$ (i.e. $K_n = \beta_n \pi / L$). the allowed frequencies are

$$\begin{aligned} f_n = \frac{w_n}{2\pi} &= \frac{1}{2\pi}\sqrt{\frac{EI}{\rho A}}k_n^2 \\ &= \frac{\pi}{2L}\sqrt{\frac{EI}{\rho A}}\beta_n^2, \end{aligned}$$

where $\beta_1 = 1.5056$, $\beta_2 = 2.4997$ and $\beta_n \approx n + \frac{1}{2}$ for $n > 2$.

Free at $x = 0$ and $x = L$

When the bar is free at both ends the constraints are as follows.

$$\frac{\partial^2 u}{\partial x^2}(0,t) = \frac{\partial^3 u}{\partial x^3}(0,t) = \frac{\partial^2 u}{\partial x^2}(L,t) = \frac{\partial^3 u}{\partial x^3}(L,t) = 0.$$

The condition at $x = 0$ gives $c = a$ and $d = b$ so that now

$$\begin{aligned}\frac{\partial^2 U}{\partial x^2} &= ak^2\left[\cosh(kx) - \cos(kx)\right] + b^2\left[\sinh(kx) - \sin(kx)\right] \\ \frac{\partial^3 U}{\partial x^3} &= ak^3\left[\sinh(kx) + \sin(kx)\right] + bk^3\left[\cosh(kx) - \cos(kx)\right].\end{aligned}$$

This clearly gives the same allowed frequencies as the clamped case, although the mode shapes will be very different.

A.2.3 Stiff Strings

Now stiffness is not only important for travelling waves in vibrating bars but also bending stiffness can be found in strings. We modify the wave equation for an ideal string by including a bar like term to give

$$\rho A\frac{\partial^2 u}{\partial t^2} = F\frac{\partial^2 u}{\partial x^2} - EI\frac{\partial^4 y}{\partial x^4}$$

where the only new parameter is the tension F. This representation of a stiff string has been used in [10]. Substitution of a plane wave of the form $u = Ae^{i(kx-wt)}$ gives the following quadratic in k^2,

$$k^4 + \frac{F}{EI}k^2 - \frac{\rho A}{EI}w^2 = 0,$$

which gives

$$k^2 = -\frac{F}{2EI} \pm \sqrt{\left(\frac{F}{2EI}\right)^2 + \frac{\rho A}{EI}w^2}.$$

Again, we may also derive a relationship for the frequency dependent wave speed $c(w)$

$$c(w)^2 = \frac{F}{2\rho A} \pm \sqrt{\left(\frac{F}{2\rho A}\right)^2 + \frac{EI}{\rho A}w^2}. \tag{A.11}$$

Note that for low frequency, the equations for k and c may be shown to approximate that of the string, but for high frequency they approximate the equations for a bar under no tension.

Boundary Conditions

Consider a stiff string of length L clamped at its boundaries. Thus the required boundary conditions are

$$u(0,t) = \frac{\partial u}{\partial x}(0,t) = u(L,t) = \frac{\partial u}{\partial x}(L,t) = 0.$$

We consider the time-reduced equation by setting $u = U(x)e^{-iwt}$ giving

$$\frac{\partial^4 U}{\partial x^4} = \beta^2 \frac{\partial^2 U}{\partial x^2} - \gamma^4 U = 0,$$

where $\beta^2 = \frac{F}{EI}$ and $\gamma^2 = w\sqrt{\frac{\rho A}{EI}}$. To solve the time-reduced equation we set $U(x) = Ae^{kx}$ so that

$$k^4 - k^2\beta^2 - \gamma^4 = 0.$$

this quadratic has two solutions,

$$k_1^2 = \sqrt{\frac{\beta^4}{4} + \gamma^4} + \frac{\beta^2}{2}$$
$$k_2^2 = \sqrt{\frac{\beta^4}{4} + \gamma^4} - \frac{\beta^2}{2},$$

each of which has two further solutions, giving a total of 4, $k = \pm k_1$, $k = \pm ik_2$. Note also that $k_1^2 - k_2^2 = \beta^2$ and that $k_1 k_2 = \gamma^2$. Thus the general solution to the reduced-time equation is

$$\begin{aligned} U(x) &= ae^{k_1 x} + be^{-k_1 x} + ce^{ik_2 x} + de^{-ik_2 x} \\ &= A\cosh(k_1 x) + B\sinh(k_1 x) + C\cos(k_2 x) + D\sin(k_2 x). \end{aligned}$$

Now, putting the origin at the centre of the string, evaluating $U(L/2) = U(-L/2) = 0$ and canceling terms involving sin and sinh gives

$$A\cosh(\frac{k_1 L}{2}) = -C\cos(\frac{k_2 L}{2}),$$

while $\frac{\partial U}{\partial x}(\frac{L}{2}) = \frac{\partial U}{\partial x}(-\frac{L}{2}) = 0$ gives

$$k_1 A\sinh(\frac{k_1 L}{2}) = k_2 C\sin(\frac{k_2 L}{2}),$$

when terms involving cos and cosh are cancelled. Dividing the second of these equation by the first, and recalling that $k_1^2 = \beta^2 + k_2^2$ yields

$$\tan(\frac{k_2 L}{2}) = -\sqrt{1 + \frac{\beta^2}{k_2^2}} \tanh(\frac{L}{2}\sqrt{\beta^2 + k_2^2}).$$

The solutions to this equation will result in a sequence $w_1, w_3, w_5, \ldots$ of allowed frequencies. Meanwhile we may generate an alternate sequence $w_2, w_4, w_6, \ldots$ of allowed frequencies by changing the cancelling above to give

$$\begin{aligned} B\sinh(\frac{k_1 L}{2}) &= -D\sin(\frac{k_2 L}{2}) \\ k_1 B\cosh(\frac{k_1 L}{2}) &= -k_2 D\cos(\frac{k_2 L}{2}), \end{aligned}$$

and hence,

$$\sqrt{1 + \frac{\beta^2}{k_2^2}} \tan(\frac{k_2 L}{2}) = \tanh(\frac{L}{2}\sqrt{\beta^2 + k_2^2}).$$

Then the allowed frequencies, which depend upon the allowed values of k_2 can be calculated using

$$\begin{aligned} w &= \sqrt{\frac{EI}{\rho A}}\gamma^2 \\ &= \sqrt{\frac{EI}{\rho A}} k_1 k_2 \\ &= k_2\sqrt{\frac{EI}{\rho A}\left(\beta^2 + k_2^2\right)}. \end{aligned}$$

Special Cases

Suppose $\beta = 0$, i.e. there is no tension, then the two equations for k_2 above become

$$\tan(\frac{k_2 L}{2}) = -\tanh(\frac{k_2 L}{2}),$$

and the allowed frequencies are $w = k_2^2\sqrt{\frac{EI}{\rho A}}$. This results in the following sequence of resonant modes in Hz which is the same as a stiff bar in the absence of tension,

$$\begin{aligned} f_1 &= \frac{3.5608}{L^2}\sqrt{\frac{EI}{\rho A}} \\ f_2 &= 2.7565 f_1 \\ f_2 &= 5.4039 f_1 \\ f_2 &= 8.9330 f_1. \end{aligned}$$

Similarly when $\beta \to \infty$, that is , the stiffness goes to zero and tension dominates, then $w = k_2\sqrt{\frac{F}{\rho A}}$ and the two equations above for k_2 reduce to

$$\tan(\frac{k_2 L}{2}) \to \infty,$$

which occurs when $k_2 = \frac{n\pi}{L}$, and hence

$$f_n = \frac{n}{2L}\sqrt{\frac{F}{\rho A}}$$

and the system has reduces that of an ideal string.

Finally we give an approximate formula for the resonant modes in a stiff string as

$$f_n = \frac{n}{2L}\sqrt{\frac{F}{\rho A}}\left[1 + \frac{2}{L}\sqrt{\frac{EI}{F}} + \left(4 + \frac{n^2\pi^2}{2}\right)\frac{EI}{LF^2}\right], \tag{A.12}$$

which is valid only when $n^2 < \frac{L^2 F}{\pi^2 EI}$.

A.3 The String on a Viscoelastic Foundation

A.3.1 The String on an Elastic Foundation

Beginning with an ideal string, characterised by the wave equation

$$F\frac{\partial^2 u}{\partial x^2} = \rho\frac{\partial^2 u}{\partial t^2},$$

where F is string tension and ρ is mass density per unit length, we include a purely elastic foundation as an external load $q(x,t) = -Gu(x,t)$ to give a new governing

equation,

$$\begin{aligned} F\frac{\partial^2 u}{\partial x^2} - Gu &= \rho\frac{\partial^2 u}{\partial t^2} \\ \Rightarrow \frac{\partial^2 u}{\partial x^2} - \frac{G}{F}u &= \frac{1}{c^2}\frac{\partial^2 u}{\partial t^2}, \end{aligned}$$

where $c = \sqrt{\frac{F}{\rho}}$. We have essentially added foundation stiffness in the form of a spring attached to each point on the string. The modified wave equation will not have a travelling wave solution of the form $f(x \pm ct)$, where undistorted pulse propagation occurs. It is logical, however, to expect some distortion in the pulse propagation [20].

Consider a harmonic solution of the form $u = Ae^{i(kx-wt)}$. Substitution in the governing equation gives

$$\left(-k^2 - \frac{G}{T} + \frac{w^2}{c^2}\right) Ae^{i(kx-wt)} = 0.$$

Solving this gives the following expressions for frequency w in term of the wavenumber k,

$$w^2 = c^2\left(k^2 + \frac{G}{F}\right). \tag{A.13}$$

Using the relationship $c = w/k$, we may also derive an expression for the frequency dependent wave speed (or phase velocity),

$$c(w) = \frac{cw}{\sqrt{w^2 - (G/T)c^2}}. \tag{A.14}$$

We may now make certain inferences about the behaviour of this system. We may predict the frequency content by examining equation A.13. Shown in Figure A-4 is a graph of frequency against wavenumber for a variety of values of spring stiffness G. From this and the equation it is clear that for large values of k, and relatively small values of the stiffness G, that the curve approaches a straight line. The upshot of this is that the lower resonant modes will tend to be bunched together, while the higher resonances will be harmonic. Of course when $G = 0$ these expression all reduce to the case of the ideal string. Shown in Figure A-4 is a graph of the frequency dependent wave speed plotted from equation A.14. Note the peculiar shape of the dispersion curves. By examining equation A.14 we see that $c(w)$ is both real and positive only for frequency values above the *cutoff* frequency $w_c = \sqrt{\frac{G}{F}}c$. For values below the cutoff frequency, the phase velocity is imaginary and has no physical significance. When $w < w_c$ we may

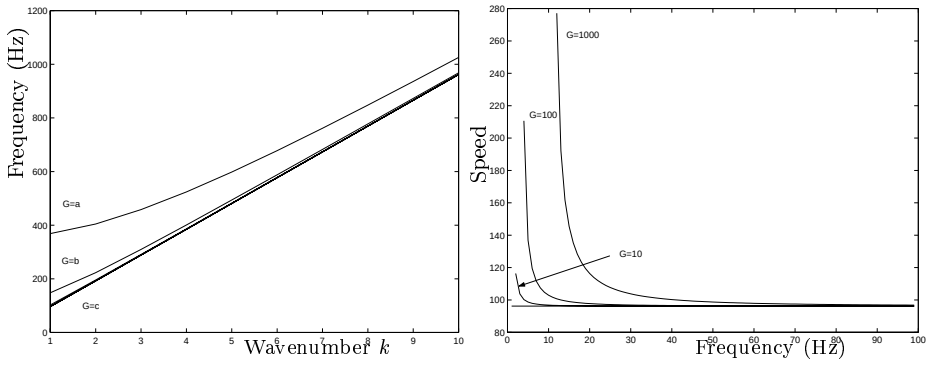

Figure A-4: *Plot of Frequency against Wavenumber and some Dispersion Curves for String on an elastic foundation.* $a = 10^6$, $b = 10^5$, $c = 0$.

rearrange equation A.13 in terms of k as

$$k = \pm i \left(\frac{G}{F} - \frac{w^2}{c_0^2} \right)^{\frac{1}{2}},$$

and the motion will be given by

$$u = Ae^{\hat{k}x} e^{-iwt},$$

where $\hat{k} = ik$. This corresponds to a spatially varying but non-propagating disturbance.

A.3.2 The string on a Viscous Foundation

Similarly to introducing dispersion on an ideal string by attaching an elastic foundation, it is also possible to introduce elementary losses by laying the string on a viscous foundation. We may consider this to be equivalent to laying the string on a bed of dash-pots [20, 38, 50]. We include a resistive force proportional the rate of change of displacement, $\frac{\partial u}{\partial t}$, to get the following governing equation,

$$F \frac{\partial^2 u}{\partial x^2} - \eta \frac{\partial u}{\partial t} = \rho \frac{\partial^2 u}{\partial t^2},$$

where η is the resistive constant of proportionality. Analysis shows that the free propagation of harmonic waves is not possible on a damped string, and that solutions have the form $u = Ae^{-\alpha x} e^{i(kx - wt)} = Ae^{i[(k+i\alpha)x - wt]}$. This is very similar to the elastic case but with a damping term. Placing this solution into the governing equation we may

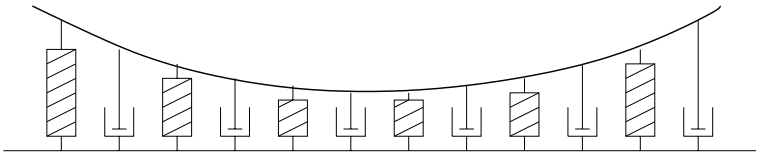

Figure A-5: *A string on a Viscoelastic Foundation.*

solve for $K = \pm(k + iw)$ where

$$k = M^{1/2}\cos(\phi/2),\ \alpha = M^{1/2}\sin(\phi/2),$$

and

$$\begin{aligned} M &= \frac{w}{T}\left(\eta^2 + \rho^2 w^2\right)^{1/2} \\ \phi &= \tan^{-1}\left(\frac{\eta}{\rho w}\right). \end{aligned}$$

Now, by examining the expression for k we see that the introduction of a viscous foundation results in some additional dispersion. We observe how k is dependent upon both w and the viscosity component η. We also note that the damping is not frequency dependent. A pictorial representation of a string placed on a viscoelastic foundation is shown in Figure A-5

A.4 Vibrations in Plates and Stiff Membranes

The equation of motion for the vibrating plate is as follows,

$$\frac{\partial^2 u}{\partial t^2} + \frac{Eh^2}{12\rho(1-\nu)}\nabla^4 u = 0,$$

where h is the plate thickness, ρ is the density, E is Young's Modulus, ν is Poisson's ratio and ∇^4 represents

$$\nabla^4 = \frac{\partial^4}{\partial x^4} + 2\frac{\partial^4}{\partial x^2 \partial y^4} + \frac{\partial^4}{\partial y^4}$$

in Cartesian coordinates.

Writing $u(x, y, t) = U(x, y)e^{iwt}$ yields the time reduced equation,

$$\begin{aligned} \nabla^4 U - \frac{12\rho(1-\nu)w^2}{Eh^2}U &= 0 \\ \Rightarrow \nabla^4 U - k^4 U &= 0 \\ \Rightarrow (\nabla^2 - k^2)(\nabla^2 + k^2)U &= 0, \end{aligned}$$

where $k^2 = \frac{\sqrt{12}w}{hc_L}$ with $c_L = \sqrt{\frac{E}{\rho(1-\nu^2)}}$. Notice that throughout we shall be dealing with the 2D frequency $w = (w_x, w_y)$. The frequency dependent speed of wave propagation may be calculated from $c = w/k$ and is

$$c(w) = \sqrt{\frac{hc_L|w|}{\sqrt{12}}}.$$

The boundary conditions for a plate are a little more complicated than their counterparts when discussing strings and bars since there exist bending moments in each of the two direction, plus twisting moments. For an edge simply supported at $x = a$ then

$$u = \frac{\partial^2 u}{\partial x^2} + \nu \frac{\partial^2 u}{\partial y^2} = 0.$$

A clamped edge at $x = a$ asserts that

$$u = \frac{\partial u}{\partial x} = 0.$$

The most complicated of edge boundaries arise in the case of a free edge. For such a boundary at $x = a$

$$\frac{\partial^2 u}{\partial x^2} + \nu \frac{\partial^2 u}{\partial y^2} = \frac{\partial^3 u}{\partial x^3} + (2-\nu)\frac{\partial^3 u}{\partial x \partial y^2}.$$

A.4.1 Circular Plates

For a circular plate we consider the reduced equation

$$(\nabla^2 - k^2)(\nabla^2 + k^2)U = 0,$$

in polar coordinates, r and θ where,

$$\nabla^2 = \frac{1}{r}\frac{\partial}{\partial r}\left(r\frac{\partial}{\partial r}\right) + \frac{1}{r^2}\frac{\partial^2}{\partial \theta^2}.$$

Thus U can be a solution of either $\nabla^2 U + k^2 U = 0$ or $\nabla^2 U - k^2 U = 0$. Solutions of the 1st equation are just the usual membrane solutions involving Bessel functions $J_m(kr)$ so that

$$U(r,\theta) = A\cos(m\theta + \alpha) J_m(kr).$$

Solutions of the 2nd equation involve the *hyperbolic Bessel functions* defined by $I_m(z) = i^{-m} J_m(iz)$. The solutions are

$$U(r,\theta) = B\cos(m\theta + \alpha) I_m(kr),$$

so that altogether the general solution is

$$U(r,\theta) = \cos(m\theta + \alpha)\left[A J_m(kr) + B I_m(kr)\right].$$

Of all the boundary conditions the easiest to handle is clamping the rim of the plate at $r = a$. That is

$$U(a,\theta) = \left(\frac{\partial Z}{\partial r}\right)_{r=a} = 0.$$

The 1st condition imposes that

$$\begin{aligned} A J_m(ka) + B I_m(ka) &= 0 \\ \Rightarrow B &= -\frac{A J_m(ka)}{I_m(ka)} \end{aligned} \tag{A.15}$$

and hence

$$U(r,\theta) = A\cos(m\theta + \alpha)\left[J_m(kr) - \frac{J_m(ka)}{I_m(ka)} I_m(kr)\right].$$

The second condition states

$$\begin{aligned} \left(\frac{\partial Z}{\partial r}\right)_{r=a} &= J_m'(ka) - \frac{J_m(ka)}{I_m(ka)} I_m'(ka) = 0 \\ \Leftrightarrow I_m(ka)\frac{\partial}{\partial r} J_m(ka) - J_m(ka)\frac{\partial}{\partial r} I_m(ka) &= 0. \end{aligned}$$

For each m there are many solutions to this equation, giving a sequence k_{mn} of allowed values for k, and hence m nodal diameters and n nodal circles. These values of k_{mn}

are

$$k_{01} = 3.189/a, k_{11} = 4.612/a, k_{21} = 5.904/a$$
$$k_{02} = 6.306/a, k_{12} = 7.801/a, k_{22} = 9.400/a$$
$$k_{03} = 9.425/a, k_{13} = 10.965/a, k_{23} = 12.566/a$$
$$k_{mn} \to (2n+m)\pi/2aasn \to \infty.$$

We are then able to calculate the allowed frequencies using

$$f_{mn} = \frac{1}{2\pi}\frac{hc_l}{\sqrt{12}}k_{mn}^2.$$

For tables of mode frequencies for circular plates with clamped, free and simply supported edges consult [15].

A.4.2 Rectangular Plates

Returning to Cartesian coordinates, setting $u(x,y,t) = X(x)Y(y)e^{iwt}$ in the stiff plate equation gives,

$$X''''Y + 2X''Y'' + XY'''' - \beta^4 XY = 0,$$

where $\beta^4 = \frac{12\rho(1-\nu^2)w^2}{Eh^2}$. Now, in order for the separation of variables to occur, we must have that

$$Y'' = -\gamma^2 Y, Y'''' = \gamma^4 Y$$

or

$$X'' = -\alpha^2 X, X'''' = \alpha^4 X,$$

or both. In the 2nd case, for example, we would have

$$\alpha^4 Y - 2\alpha^2 Y'' + Y'''' - \beta^4 Y = 0.$$

If the 2nd case does indeed hold then we have $X = \sin(\alpha x)$ or $X = \cos(\alpha x)$ and we may consider the various possibilities for the boundary conditions.

If the edge is simply supported at $x = 0$ and $x = a$,

$$u(0) = X(0)Y(y) = 0$$

and

$$\left(\frac{\partial^2 u}{\partial x^2} + \nu \frac{\partial^2 u}{\partial y^2}\right)_{x=0} = X(0)(-\alpha^2 Y(y) + \nu Y^{''}(y) = 0,$$

hence $X(0) = 0$, since $\frac{\partial^2 u}{\partial x^2} + \nu \frac{\partial^2 u}{\partial y^2} = X^{''}Y + \nu XY^{''} = -\alpha^2 XY + \nu XY^{''}$. Similarly we may show that we require $X(a) = 0$, and hence

$$X_n(x) = \sin(\alpha_n x),$$

where $\alpha_n = \frac{n\pi}{a}$.

Now, for a clamped edge, we would require $u(0) = \frac{\partial u}{\partial x}(0) = 0$. This would mean that

$$\begin{aligned} X(0)Y(y) = X^{'}(0)Y(y) = 0 \\ \Rightarrow X(0) = X^{'}(0) = 0, \end{aligned}$$

which is clearly not possible if $X = \sin(\alpha x), \cos(\alpha x)$. Finally, for a free edge we would require

$$\begin{aligned} X(0)\left[-\alpha^2 Y(y) + \nu Y^{''}(y)\right] = 0 \\ X^{'}(0)\left[-\alpha^2 Y(y) + (2-\nu)Y^{''}(y)\right] = 0, \end{aligned}$$

which would again require $X(0) = X^{'}(0) = 0$.

Thus we conclude that in order to separate variables, we require that at least two opposite edges are simply supported (meaning 6 combinations). Now suppose that the y-edge is simply supported at $y = 0$ and $y = b$. We find that this gives

$$Y_m(x) = \sin(\gamma_m y),$$

where $\gamma_m = \frac{m\pi}{b}$. Placing X_n and Y_m into the time reduced equation yields

$$\begin{aligned} (\alpha_n^4 + 2\alpha_n^2\gamma_m^2 + \gamma_m^4 - \beta^4)X_n Y_m = 0 \\ \Rightarrow \left[(\alpha_n^2 + \gamma_n^2)^2 - \beta^4\right] X_n Y_m = 0. \end{aligned}$$

Recalling that $\beta^4 = \frac{12\rho(1-\nu^2)}{Eh^2}w^2$ we may now calculate the allowed frequencies for a

simply supported rectangular plate,

$$\begin{aligned}
\beta^4 &= (\alpha_n^2 + \gamma_n^2)^2 \\
\Rightarrow w_{mn}^2 &= \frac{Eh^2}{12\rho(1-\nu^2)}(\alpha_n^2 + \gamma_n^2)^2 \\
\Rightarrow w_{mn} &= \sqrt{\frac{Eh^2}{12\rho(1-\nu^2)}}(\alpha_n^2 + \gamma_n^2) \\
\Rightarrow w_{mn} &= \pi^2\sqrt{\frac{Eh^2}{12\rho(1-\nu^2)}}\left[\left(\frac{n}{a}\right)^2 + \left(\frac{m}{b}\right)^2\right].
\end{aligned}$$

The case of all four edges being simply supported is just one of six combinations where at least two opposite edges are simply supported. For the remaining cases consult [20].

A.4.3 Bending Stiffness in a Membrane

Just as in the case with a stiff string, we add a plate like term to the ideal membrane equation to give

$$\frac{\partial^2 u}{\partial t^2} = \frac{F}{\rho}\nabla^2 u - \frac{Eh^2}{12\rho(1-\nu)}\nabla^4 u,$$

where the new parameter is the tension F. Assuming a solution $z = AJ_m(kr)\cos(m\theta)\cos(wt)$ leads to the following quadratic in k^2,

$$k^4 + \frac{c^2}{S^4}k^2 - \beta^4 = 0,$$

where $S^4 = \frac{Eh^2}{12\rho(1-\nu^2)}$, $c^2 = \frac{F}{\rho}$ and β is defined as before. For a clamped boundary condition, this gives rise to the following allowed frequencies,

$$f_{mn} = k_{mn}\frac{c}{2\pi}\sqrt{1 + \frac{S^4}{c^2}k_{mn}^2},$$

where the values k_{mn} are the same as those found for the circular membrane in the absence of stiffness. Note also that removing the stiffness reduces the equation for the allowed frequencies to that of the ideal membrane in the absence of stiffness, while removing the tension results in modal frequencies for a clamped circular plate.

Appendix B

Finite Difference Schemes

It is perhaps necessary to make a few comments and describe a few mathematical derivations behind some of the Finite Difference methods employed throughout this thesis. In this short appendix we quickly review the derivation of a finite difference approximation and resulting numerical schemes, then describe a frequency domain based analysis method which is used repeatedly during the course of this work. Finally we list the most relevant schemes used during the thesis for reference, and include a description of an interpolated scheme for completeness. There are many introductory texts on Finite Difference Schemes (FDS) for approximating PDEs such as [22, 47].

B.1 Deriving Finite Difference Approximations

Finite differences may be used to approximate partial derivatives in the following way. Consider approximating the spatial derivative $\frac{\partial y}{\partial x}$, which is of course the slope of the curve y, at the point $x = a$. By considering the value of the curve y at a point $x = a+\Delta$, we may approximate the gradient at $x = a$ by

$$\frac{\partial y}{\partial x}\Big|_{x=a} \approx \frac{y(a+\Delta) - y(a)}{\Delta},$$

as shown in Figure B-1. Similarly we may approximate a time derivative by considering the value of the function y at time instants $t = s$ and $t = s + T$, that is,

$$\frac{\partial y}{\partial t}\Big|_{t=s} \approx \frac{y(s+T) - y(s)}{T}.$$

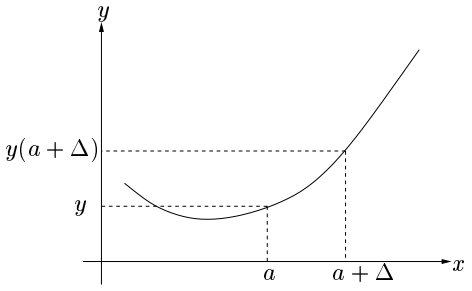

Figure B-1: *Deriving a first order difference.*

Now, by discretising the x axis into sections of length Δ, and by splitting time into intervals of duration T, we may represent the function $y(x,t)$ at discrete points by

$$Y_j(n) = y(j\Delta, nT),$$

where n and j are integers. Consequently the approximations above may be recast as

$$\left.\frac{\partial y}{\partial x}\right|_{x=j\Delta} \approx \frac{Y_{j+1}(n) - Y_j(n)}{\Delta},$$

and

$$\left.\frac{\partial y}{\partial x}\right|_{t=nT} \approx \frac{Y_j(n+1) - Y_j(n)}{T}.$$

We call Δ the *spatial step* and T the *time step.*

By simply re-applying the first order differences to themselves we may derive finite difference approximations to second order derivatives so that.

$$\begin{aligned}
\tfrac{\partial^2 y}{\partial x^2} &\approx \frac{Y_{j-1}(n) - 2Y_j(n) + Y_{j+1}(n)}{\Delta^2}, \\
\tfrac{\partial^2 y}{\partial t^2} &\approx \frac{Y_j(n-1) - 2Y_j(n) + Y_j(n+1)}{T^2},
\end{aligned}$$

We may derive finite differences for 2nd order 2D derivatives by defining a grid of points so that a function $u(x,y,t)$ is discretised by

$$U_{i,j}(n) = u(i\Delta, j\Delta, nT).$$

Some commonly used finite differences are listed below,

$$\begin{aligned}
\frac{\partial^2 u}{\partial x^2} &\approx \frac{U_{i-1,j}(n) - 2U_{i,j}(n) + U_{i+1,j}(n)}{\Delta^2}, \\
\frac{\partial^2 u}{\partial y^2} &\approx \frac{U_{i,j-1}(n) - 2U_{i,j}(n) + U_{i,j+1}(n)}{\Delta^2}, \\
\frac{\partial^2 u}{\partial t^2} &\approx \frac{U_{i,j}(n-1) - 2U_{i,j}(n) + U_{i,j}(n+1)}{T^2}.
\end{aligned}$$

Similar differences may derived in 3D and for higher order or crossed derivatives.

B.2 Difference Schemes for the Wave Equation

The digital waveguide can be thought of as a discretisation of the D'Alembert solution to the 1D wave equation, or as a structure which is equivalent to a FDS for the wave equation. For all the waveguide structures discussed in this thesis we may derive equivalences to centered FDSs for the appropriate PDE. In this section we describe simple FDSs for the wave equation in one, two and three dimensions which are referred to in the general body of the thesis.

The following difference scheme can be used for the 1D wave equation.

$$U_j(n+1) - 2U_j(n) + U_j(n-1) = c^2 \frac{T^2}{\Delta^2}\Big[U_{j+1}(n) - 2U_j(n) + U_{j-1}(n)\Big].$$

For a square grid straight-forward application of the finite differences described above to the 2D wave equation results in the scheme,

$$\begin{aligned}
U_{i,j}(n+1) - 2U_{i,j}(n) + U_{i,j}(n-1) = c^2 \frac{T^2}{\Delta^2}\Big[&U_{i+1,j}(n) - 2U_{i,j}(n) + U_{i-1,j}(n) \\
&+U_{i,j+1}(n) - 2U_{i,j}(n) + U_{i,j+1}(n)\Big].
\end{aligned}$$

We may also consider points arranged on a triangular grid, where the scheme becomes.

$$\begin{aligned}
U_{i,j}(n+1) - 2U_{i,j}(n) + U_{i,j}(n-1) = c^2 \frac{T^2}{\Delta^2}\frac{2}{3}\Big[&U_{i+1,j}(n) - 2U_{i,j}(n) + U_{i-1,j}(n) \\
&+ U_{i+\frac{1}{2},j+\frac{\sqrt{3}}{2}}(n) - 2U_{i,j}(n) + U_{i-\frac{1}{2},j-\frac{\sqrt{3}}{2}}(n) \\
&+ U_{i-\frac{1}{2},j+\frac{\sqrt{3}}{2}}(n) - 2U_{i,j}(n) + U_{i+\frac{1}{2},j-\frac{\sqrt{3}}{2}}(n)\Big].
\end{aligned}$$

Using a simple cubic grid we may extend the FDS method for the 3D wave equation. This time we have a point $u(x, y, z, t)$ discretised by $U_{i,j,k}(n) = u(i\Delta, j\Delta, k\Delta, nT)$ so

that the simplest explicit scheme becomes

$$\begin{aligned} U_{i,j,k}(n+1) - 2U_{i,j,k}(n) + U_{i,j,k}(n-1) = c^2\frac{T^2}{\Delta^2}\Big[&U_{i+1,j,k}(n) - 2U_{i,j,k}(n) + U_{i-1,j,k}(n) \\ &+ U_{i,j+1,k}(n) - 2U_{i,j,k}(n) + U_{i,j+1,k}(n) \\ &+ U_{i,j,k+1}(n) - 2U_{i,j,k}(n) + U_{i,j,k-1}(n)\Big]. \end{aligned} \tag{B.1}$$

Using the Dodecahedral Mesh described in chapter 3 gives the difference scheme

$$\begin{aligned} &U_{i,j,k}(n+1) - 2U_{i,j,k}(n) + U_{i,j,k}(n-1) = \\ &\quad c^2\frac{T^2}{\Delta^2}\frac{1}{2}\Big[U_{i+1,j,k}(n) - 2U_{i,j,k}(n) + U_{i-1,j,k}(n) \\ &\quad +U_{i+\frac{1}{2},j+\frac{\sqrt{3}}{2},k}(n) - 2U_{i,j,k}(n) + U_{i-\frac{1}{2},j+\frac{\sqrt{3}}{2},k}(n) \\ &\quad +U_{i-\frac{1}{2},j-\frac{\sqrt{3}}{2},k}(n) - 2U_{i,j,k}(n) + U_{i+\frac{1}{2},j-\frac{\sqrt{3}}{2},k}(n) \\ &\quad +U_{i,j+\frac{1}{\sqrt{3}},k+\sqrt{\frac{2}{3}}}(n) - 2U_{i,j,k}(n) + U_{i,j-\frac{1}{\sqrt{3}},k-\sqrt{\frac{2}{3}}}(n) \\ &\quad +U_{i-\frac{1}{2},j-\frac{1}{2\sqrt{3}},k+\sqrt{\frac{2}{3}}}(n) - 2U_{i,j,k}(n) + U_{i+\frac{1}{2},j+\frac{1}{2\sqrt{3}},k-\sqrt{\frac{2}{3}}}(n) \\ &\quad +U_{i+\frac{1}{2},j-\frac{1}{2\sqrt{3}},k+\sqrt{\frac{2}{3}}}(n) - 2U_{i,j,k}(n) + U_{i-\frac{1}{2},j+\frac{1}{2\sqrt{3}},k-\sqrt{\frac{2}{3}}}(n)\Big]. \end{aligned}$$

B.3 Von Neumann Analysis

Throughout this thesis we use the technique of Von Neumann analysis to examine the stability and phase information of various schemes [47]. Through the use of the Fourier transform the determination of stability of a scheme is reduced to a few simple algebraic considerations. To demonstrate the procedure we consider a general 1D multi-step scheme, which we may write as

$$V_m(n+1) = \sum_{k=-K}^{K}\sum_{l=0}^{L} a_{k,n-l}V_{m+k}(n-l), \tag{B.2}$$

where the $a_{k,n-l}$ are constant coefficients. We now take the Fourier transform of equation (B.2) recalling that if $\hat{V}_m^n(w)$ is the Fourier transform of $V_m(n)$ then

$$\hat{V}_{m+k}^n(w) = e^{ikw}\hat{V}_m^n(w)$$

is the Fourier transform of $V_{m+k}(n)$. Consequently the Fourier transform of equation (B.2) can be written as

$$\begin{aligned}\hat{V}_m^{n+1}(w) &= \sum_{k=-K}^{K}\sum_{l=0}^{L} a_{k,n-l}e^{ikw}\hat{V}_m^{n-l}(w) \\ &= \sum_{k=-K}^{K} e^{ikw}\sum_{l=0}^{L} a_{k,n-l}\hat{V}_m^{n-l}(w). \end{aligned} \tag{B.3}$$

Now in this form of analysis we search for an *spectral amplification factor* $g(w)$ which will tell us how the scheme changes in the frequency domain when the solution is advanced by one time step. Thus we look for solutions of the form $\hat{V}_m^n(w) = g(w)\hat{V}_m^{n-1}(w)$. If this identity held, then by induction we could write $\hat{V}_m^n(w) = g^n\hat{V}_m^0(w)$. The equation (B.3) can then be expressed as

$$g_{n+1}\hat{V}_m^0(w) = \sum_{k=-K}^{K} e^{ikw}\sum_{l=0}^{L} a_{k,n-l}g^{n-l}\hat{V}_m^0(w).$$

Dividing through by $\hat{V}_m^0(w)$ gives the *amplification polynomial* whose roots give the amplification factor,

$$g^{n+1} = \sum_{k=-K}^{K}\sum_{l=0}^{L} e^{ikw}a_{k,n-l}g^{n-l}.$$

Thus we have shown that advancing the scheme by one time step is equivalent to multiplying the Fourier transform of the solution by the amplification factor $g(w)$. This function is dependent on frequency, and we may consider its magnitude, which tells us about the stability of the scheme, and we may consider its phase, which will tell us the speed of wave propagation within the scheme. By regarding these two properties we may decide how well the scheme approximates the PDE in question. These techniques can be equally be applied in two or higher dimensions.

B.4 Interpolated Schemes

B.4.1 Interpolated Schemes in 2D

We may consider approximating a two-dimensional, second order spatial derivative at a point using centered differences, and using eight surrounding points, placed one spatial

step away from the desired point as follows.

$$\begin{aligned}\frac{\partial^2 v}{\partial x^2}+\frac{\partial^2 v}{\partial y^2} &\approx V_{i-1,j}(n)-2V_{i,j}(n)+V_{i+1,j}(n)\\ &+ V_{i,j-1}(n)-2V_{i,j}(n)+V_{i,j+1}(n)\\ &+ V_{i+\frac{1}{\sqrt{2}},j+\frac{1}{\sqrt{2}}}(n)-2V_{i,j}(n)+V_{i-\frac{1}{\sqrt{2}},j-\frac{1}{\sqrt{2}}}(n)\\ &+ V_{i-\frac{1}{\sqrt{2}},j+\frac{1}{\sqrt{2}}}(n)-2V_{i,j}(n)+V_{i+\frac{1}{\sqrt{2}},j-\frac{1}{\sqrt{2}}}(n).\end{aligned}$$

Consequently we are required to evaluate four points which do not fall on grid points of the square mesh. We thus consider approximating the values at these points using bilinear interpolation as follows,

$$\begin{aligned}V_{i+\frac{1}{\sqrt{2}},j+\frac{1}{\sqrt{2}}}(n) &\approx w_a V_{i+1,j}(n)+w_a V_{i,j+1}(n)+w_d V_{i+1,j+1}(n)+w_c V_{i,j}(n)\\ V_{i-\frac{1}{\sqrt{2}},j+\frac{1}{\sqrt{2}}}(n) &\approx w_a V_{i-1,j}(n)+w_a V_{i,j+1}(n)+w_d V_{i-1,j+1}(n)+w_c V_{i,j}(n)\\ V_{i-\frac{1}{\sqrt{2}},j-\frac{1}{\sqrt{2}}}(n) &\approx w_a V_{i-1,j}(n)+w_a V_{i,j-1}(n)+w_d V_{i-1,j-1}(n)+w_c V_{i,j}(n)\\ V_{i+\frac{1}{\sqrt{2}},j-\frac{1}{\sqrt{2}}}(n) &\approx w_a V_{i,j-1}(n)+w_a V_{i+1,j}(n)+w_d V_{i+1,j-1}(n)+w_c V_{i,j}(n),\end{aligned}$$

where $w_a = a(1-a)$, $w_d = a^2$, $w_c = (1-a)^2$, with $a = 1/\sqrt{2}$. Note that bilinear interpolation is the process by which we may approximate the velocity at a point between mesh nodes by considering the velocity at the four mesh nodes surrounding the point. It is termed bilinear as it produces a function which is linear along each edge of each square mesh region. For a general point, the interpolation coefficients can be calculated by regarding Figure B-2. This gives the interpolation coefficients as $w_x = a_x(1-a_x)$, $w_y = a_y(1-a_x)$, $w_d = a_x a_y$ and $w_c = (1-a_x)(1-a_y)$. Of course in the above interpolation, $a_x = a_y = a$. Using these approximations we may now write down a finite difference scheme for the 2D wave equation,

$$\begin{aligned}V_{i,j}(n+1)-2V_{i,j}(n)+V_{i,j}(n-1) = \mu^2 c^2 \Big\{ & w_d V_{i-1,j+1}(n)+(1+2w_a)V_{i,j+1}(n)+w_d V_{i+1,j+1}(n)\\ &+(1+2w_a)V_{i-1,j}(n)+(4w_c-8)V_{i,j}(n)+(1+2w_a)V_{i+1,j}(n)\\ &+w_d V_{i-1,j-1}(n)+(1+2w_a)V_{i,j-1}(n)+w_d V_{i+1,j-1}(n)\Big\},\end{aligned}$$

where $\mu = T/\Delta$.

We may define a digital waveguide mesh which corresponds to this scheme as follows [8]. Consider a square mesh of nine port junctions, where each junction is connected to its eight neighbours and includes a self loop of one unit of delay. The impedance of the waveguides in the axial directions are set to Y_a, the impedances in diagonal directions are Y_b, while the self loop has an impedance Y_c. Then the junction

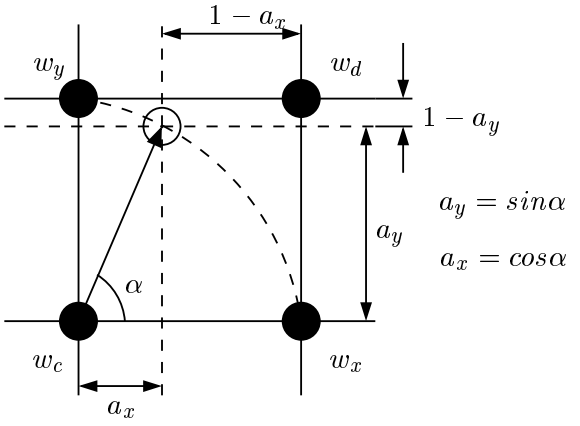

Figure B-2: *Calculating Bilinear Interpolation Coefficients.*

velocity can be written in terms of its input velocities as

$$V_{i,j}(n+1) = \frac{2}{Y_J}\sum_{i=1}^{9} Y_k V^+_{i,j,k}(n+1),$$

where $Y_k = Y_a, Y_b, Y_c$, and Y_J is the total junction impedance. Using the standard method of writing inputs to one junction as outputs of neighbouring junctions at the previous time step we have,

$$\begin{aligned} V_{i,j}(n+1) = \frac{2}{Y_J}\Big[& Y_b V_{i-1,j+1}(n) + Y_a V_{i,j+1}(n) + Y_b V_{i+1,j+1}(n) \\ & + Y_a V_{i-1,j}(n) + Y_c V_{i,j}(n) + Y_a V_{i+1,j}(n) \\ & + Y_b V_{i-1,j-1}(n) + Y_a V_{i,j-1}(n) + Y_b V_{i+1,j-1}(n)\Big] \\ & - V_{i,j}(n-1). \end{aligned}$$

Now setting $Y_b = w_d$, $Y_a = 1 + 2w_a$ and $Y_c = 4w_c$ gives us our equivalence to the interpolated finite difference scheme described previously. Using these values for the impedance we also find that $\frac{2}{Y_J} = \frac{1}{4}$, giving a final expression

$$\begin{aligned} V_{i,j}(n+1) - 2V_{i,j}(n) + V_{i,j}(n-1) = \frac{2}{Y_J}\Big\{ & w_d V_{i-1,j+1}(n) + (1+2w_a)V_{i,j+1}(n) + w_d V_{i+1,j+1}(n) \\ & + (1+2w_a)V_{i-1,j}(n) + (4w_c - 8)V_{i,j}(n) + (1+2w_a)V_{i+1,j}(n) \\ & + w_d V_{i-1,j-1}(n) + (1+2w_a)V_{i,j-1}(n) + w_d V_{i+1,j-1}(n)\Big\}. \end{aligned}$$

We may now calculate the dispersion for the interpolated waveguide mesh/FDS. Proceeding as usual we may calculate the spectral amplification factor g by solving the

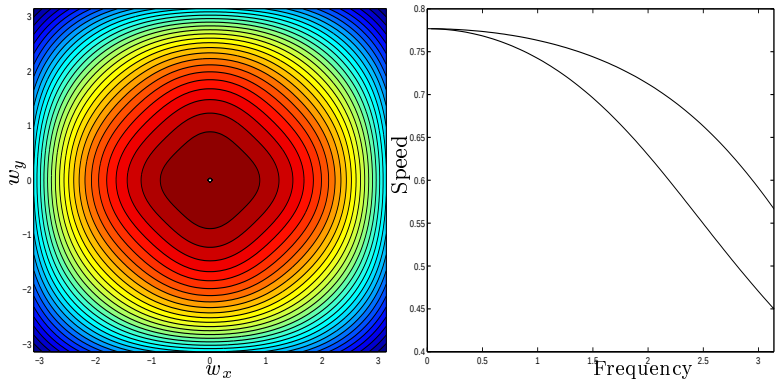

Figure B-3: *(a) Dispersion Plot for Interpolated Waveguide Mesh. (b) Max and Min Dispersions for Interpolated Waveguide Mesh*

quadratic equation $g^2 + Bg + 1 = 0$ where,

$$b = \frac{1}{2}\big[w_d \cos(w_x + w_y) + w_d \cos(w_x + w_y) \\ +(1 + 2w_a)\cos(w_x) + (1 + 2w_a)\cos(w_y) + 2w_c - 4\big],$$

where this time (w_x, w_y) is the two dimensional frequency vector. As usual we have that $b^2 - 4 < 0$, giving complex solutions for the amplification factor, and hence stability. Of course, stability is guaranteed due to the passivity of the waveguide mesh. The dispersion is then calculated as the normalised phase angle of the amplification factor and is shown as a grey scale plot in Figure B-3. Also shown are cross-sections indicating the extremes of dispersion through different angles. It shows that there is only a little angular dependence, and it certainly improves upon the standard square mesh, but the triangular mesh provides the most desirable characteristics.

In this section we introduced a method which altered a regular square mesh to give near direction independent dispersion error. It was first introduced in [42], and was then extended to correct dispersion error in [43]. The idea was originally described as being a bilinearly deinterpolated waveguide mesh. It was proposed that by extending the number of propagation directions, we would theoretically be able to produce a mesh exhibiting angularly independent dispersion error. The problem with the diagonal directions would be overcome by spreading their contributions to each of the four nodes surrounding the theoretical node using inverse bilinear interpolation called *deinterpolation*. However we found that attempting this using scattering waves, so that the output in a diagonal direction was deinterpolated onto the diagonal inputs of the four surrounding junctions, was not equivalent to the finite difference scheme defined in the literature. In fact, by deriving the process here, we have shown that no deinter-

polation actually takes place. The method may be best described as an interpolated finite difference scheme with an equivalent waveguide mesh implementation.

B.4.2 Interpolated Schemes in 3D

The 2D interpolated waveguide mesh/FDS described in the previous section was shown to produce near direction independent dispersion error, although we considered the triangular mesh to be the best 2D geometry. However, when we extend into three dimensions, it becomes harder to find desirable mesh structures (See chapter 3). We now describe an interpolated 3D scheme derived by interpolating a theoretical 26-dimensional mesh. A 3D second order spatial derivative may be approximated by a 26-directional difference with a unit spatial step size as

$$\begin{aligned}
\frac{\partial^2 v}{\partial x^2} + \frac{\partial^2 v}{\partial x^2} + \frac{\partial^2 v}{\partial x^2} \approx\ & V_{i+1,j,k}(n) - 2V_{i,j,k}(n) + V_{i-1,j,k}(n) \\
+\ & V_{i,j+1,k}(n) - 2V_{i,j,k}(n) + V_{i,j-1,k}(n) \\
+\ & V_{i,j,k+1}(n) - 2V_{i,j,k}(n) + V_{i,j,k-1}(n) \\
+\ & V_{i+b,j+b,k}(n) - 2V_{i,j,k}(n) + V_{i-b,j-b,k}(n) \\
+\ & V_{i-b,j+b,k}(n) - 2V_{i,j,k}(n) + V_{i+b,j-b,k}(n) \\
+\ & V_{i+b,j,k+b}(n) - 2V_{i,j,k}(n) + V_{i-b,j,k-b}(n) \\
+\ & V_{i-b,j,k+b}(n) - 2V_{i,j,k}(n) + V_{i+b,j,k-b}(n) \\
+\ & V_{i,j+b,k+b}(n) - 2V_{i,j,k}(n) + V_{i,j-b,k-b}(n) \\
+\ & V_{i,j-b,k+b}(n) - 2V_{i,j,k}(n) + V_{i,j+b,k-b}(n) \\
+\ & V_{i+a,j+a,k+a}(n) - 2V_{i,j,k}(n) + V_{i-a,j-a,k-a}(n) \\
+\ & V_{i-a,j+a,k+a}(n) - 2V_{i,j,k}(n) + V_{i+a,j-a,k-a}(n) \\
+\ & V_{i+a,j-a,k+a}(n) - 2V_{i,j,k}(n) + V_{i-a,j+a,k+a}(n) \\
+\ & V_{i-a,j-a,k+a}(n) - 2V_{i,j,k}(n) + V_{i+a,j+a,k-a}(n),
\end{aligned}$$

where $a = \frac{1}{\sqrt{3}}$ and $b = \frac{1}{\sqrt{2}}$. Proceeding in an analogous fashion to the 2D case we now approximate the diagonal contributions using interpolation. Interpolation in each plane is bilinear so that, for example,

$$V_{i+b,j+b,k}(n) \approx \alpha_a V_{i+1,j,k}(n) + \alpha_a V_{i,j+1,k}(n) + \alpha_d V_{i+1,j+1,k}(n) + \alpha_c V_{i,j,k}(n),$$

where $\alpha_a = b(1-b)$, $\alpha_c = (1-b)^2$ and $\alpha_d = b^2$. We also use tri-linear interpolation in the following way,

$$\begin{aligned} V_{i+a,j+a,k+a}(n) &\approx w_a \left(V_{i+1,j,k}(n) + V_{i,j+1,k}(n) + V_{i,j,k+1}(n)\right) \\ &+ w_b \left(V_{i+1,j+1,k}(n) + V_{i+!,j,k+1}(n) + V_{i,j+1,k+1}(n)\right) \\ &+ w_d V_{i+1,j+1,k+1}(n) + w_c V_{i,j,k}(n), \end{aligned}$$

where $w_a = a(1-a)^2$, $w_b = a^2(1-a)$, $w_d = a^3$ and $w_c = (1-a)^3$ are the interpolation coefficients. We are thus able to derive a FDS which approximates the 3D wave equation as follows,

$$V_{i,j,k}(n+1) - 2V_{i,j,k}(n) + V_{i,j,k}(n-1) = \mu c^2 \sum_{\substack{l,m,n \\ \in [-1,1]}} \left[h_{i+l,j+m,k+n} V_{i,j,k}(n)\right] - 2V_{i,j,k}(n),$$

where $\mu = T^2/\Delta^2$, and the coefficients $h_{i,j,k}$ are as follows,

$$h_{1,1,3} = h_{1,3,3} = h_{3,3,3} = h_{3,1,3} = h_{1,1,1} = h_{1,3,1} = h_{3,3,1} = h_{3,1,1} = w_d$$

$$\begin{aligned} h_{1,2,3} = h_{2,3,3} = h_{3,2,3} = h_{2,1,3} = h_{1,1,2} = h_{1,3,2} = h_{3,3,2} = h_{3,1,2} = h_{1,2,1} = h_{2,3,1} \\ = h_{3,2,1} = h_{2,1,1} = 2w_b + \alpha_d \end{aligned}$$

$$h_{2,2,3} = h_{2,2,1} = h_{1,2,2} = h_{2,3,2} = h_{3,2,2} = h_{2,1,2} = 4(w_a + \alpha_a) + 1$$

$$h_{2,2,1} = 8w_c + 12\alpha_c.$$

Again analogously to the 2D case, we may derive a waveguide mesh which is entirely equivalent to this FDS. We create a 3D square mesh of scattering junctions comprising 26 ports in the propagation directions, together with a self-loop. A small portion of the scattering junction is shown in Figure B-4. It shows the input impedances from the typical directions and we set the self-loop impedance to R_c. It can be shown that by setting the impedances to $R_a = 4(w_a + \alpha_a) + 1$, $R_b = 2w_b + \alpha_d$, $R_d = w_d$ and $R_c = 8w_c + 12\alpha_c$, the resulting FDS is equivalent to equation B.4 with $\mu^2 c = 1/13$.

Furthermore, we may also compute the dispersion of this scheme. Again by taking Fourier transforms we find the spectral amplification factor by solving the quadratic

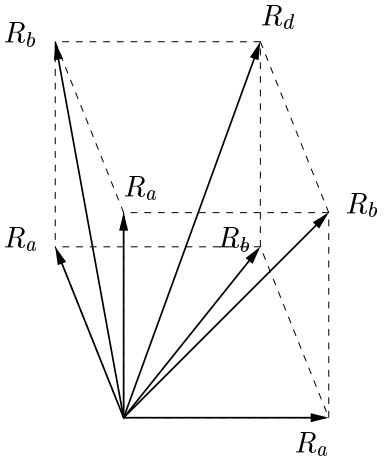

Figure B-4: *Scattering junction in the 3-d interpolated waveguide mesh.*

$g^2 + bg + 1 = 0$ where,

$$
\begin{aligned}
b = \frac{2}{13}\Big(& R_a[\cos(w_x) + \cos(w_y) + \cos(w_z)] \\
& + R_d[\cos(w_x + w_y + w_z) + \cos(w_x - w_y + w_z) \\
& \qquad + \cos(w_x + w_y - w_z) + \cos(w_x - w_y - w_z)] \\
& + R_b[\cos(w_x + w_y) + \cos(w_x - w_y) + \cos(w_x + w_z) \\
& \qquad + \cos(w_x - w_z) + \cos(w_y + w_z) + \cos(w_y - w_z)] \\
& + R_c/2\Big).
\end{aligned}
$$

Shown in Figure B-5 are grey scale plots of dispersion as viewed through a variety of cross-sections of the interpolated mesh. Firstly, they are almost identical, and secondly they produce near direction independent dispersion error. Such a scheme had been used in the finite difference domain to produce some elementary models of 3D acoustic spaces in [40].

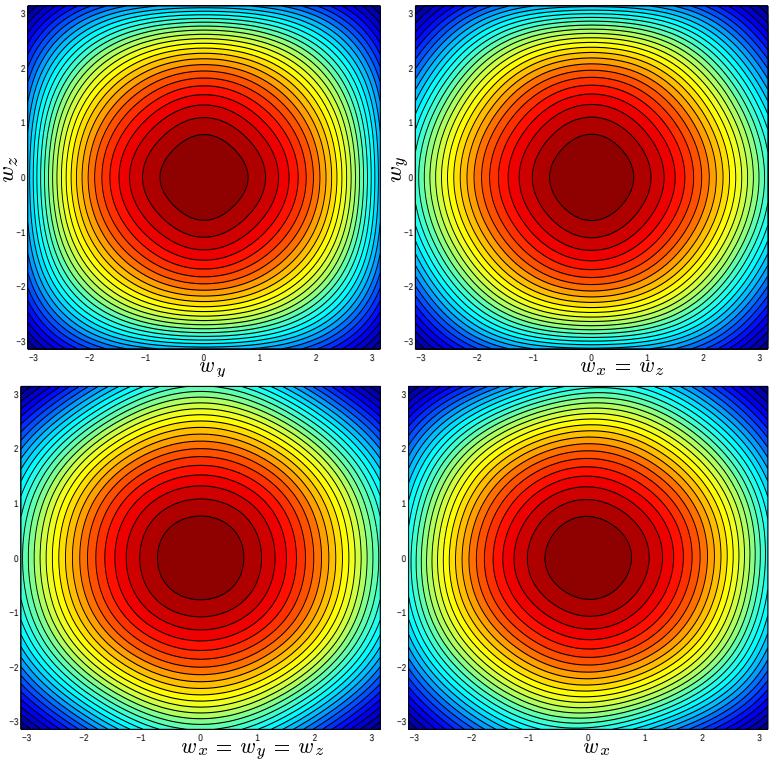

Figure B-5: *Dispersion error for various cross sections through interpolated waveguide mesh. (a)* $w_x = 0$, *(b)* $w_x = w_z$, *(c)* $w_x = w_y = w_z$, *(d)* $w_y = w_z = \frac{1}{\sqrt{3}} w_x$.

Appendix C

Digital Signal Processing

Throughout the course of this thesis we have made reference to many elements from the vast field of digital signal processing so we provide some basic definitions here. Digital waveguides have provided a link between numerical analysis and the theory of digital signals. In all the models described in the work, we have applied the Discrete Fourier Transform to extract frequency information. We have also considered the use of digital filters. For a complete introduction to DSP and its application to music sound synthesis, the reader is directed towards [32, 36].

C.1 Transforms

Given a signal $x(n)$ the *Z-transform* is computed as

$$X(z) = \sum_{n=-\infty}^{\infty} x(n)z^{-n}, \tag{C.1}$$

where z is a complex variable. There are some useful properties of the Z-transform when dealing with signals. Suppose $y(n) = x(n-k)$ then

$$Y(z) = z^{-k}X(z).$$

So that delaying a signal by k samples results in multiplying its Z-transform by z^{-k}. If $g(n) = x(n) * y(n)$ then

$$G(z) = X(z)Y(z).$$

It may also be interesting to note that the Z-transform is the discrete time equivalent of the Laplace Transform.

The *Discrete Fourier Transform* of a signal $x(n)$ is defined as

$$\hat{X}(w) = \sum_{n=-\infty}^{\infty} x(n)e^{-inw}. \tag{C.2}$$

Note that the discrete Fourier transform is a special case of the Z-transform for points on the unit circle in the complex plane, that is $z = e^{iw}$. By using this transform we represent the signal in terms of its frequency distribution. We use the Fourier transform to analyse the frequency content.

C.2 Digital Filters

A digital filter may be broadly described as an algorithm which processes a digital signal. That is, the filter produces an output signal $y(n)$ by manipulating values from an input signal $x(n)$. In this thesis we shall deal with linear, causal filters which can be represented by the *digital filter equation*

$$y(n) = \sum_{i=0}^{M} a_i x(n-i) - \sum_{i=0}^{N} b_i y(n-i), \tag{C.3}$$

where the a_i and b_i are constant coefficients. By feeding an impulse (one whose first value is one, and all subsequent values are zero) in to the filter, the output is known as the *impulse response* of the filter. If this response is denoted by $h(n)$ then the output of the filter can be written as

$$y(n) = h(n) * x(n),$$

where $*$ denotes convolution. When each $b_i = 0$ in equation (C.3) then the output depends only on previous inputs, so that the impulse response must eventually die away. Such a filter is known as a *finite impulse response* (FIR) filter. When some of the b_i are non-zero, then the impulse response will never die away completely, and such a filter is called an *infinite impulse response* (IIR) filter.

A good way to describe and analyse a filter is to consider its form in the Z-domain. By taking the Z-transform of equation (C.3) we have

$$Y(z) = \sum_{i=0}^{M} a_i z^{-i} X(z) - \sum_{i=0}^{N} b_i z^{-i} Y(z),$$

which may be rearranged to give

$$Y(z) = H(z)X(z),$$

where

$$H(z) = \frac{a_0 + a_1 z^{-1} + \cdots + a_M z^{-M}}{1 + b_1 z^{-1} + \cdots + b_N z^{-N}}.$$

We call $H(z)$ the *transfer function* of the filter, and note that it is the Z-transform of the impulse response $h(n)$. We could also derive this result by recalling that convolution in the digital domain becomes multiplication in the Z-domain.

Given the transfer function $H(z)$ we may examine the effect of the filter on certain frequencies on the input signal by evaluating the transfer function at $z = e^{iw}$. Thus the *frequency response* $H(e^{iw})$ of the filter relates the Fourier Transforms of the input and output signals by

$$Y(e^{iw}) = H(e^{iw})X(e^{iw}).$$

Thus the magnitudes and phases of the Fourier Transforms are related by

$$\begin{aligned} |Y(e^{iw})| &= |H(e^{iw})||X(e^{iw})| \\ \arg\{Y(e^{iw})\} &= \arg\{H(e^{iw})\} + \arg\{X(e^{iw})\}. \end{aligned}$$

We call $|Y(e^{iw})|$ the *magnitude response* or *gain* of the filter. It tells us the way in which frequencies are enhanced or suppressed by the filter. The quantity $\arg\{Y(e^{iw})\}$ is called the *phase response* and relates to the positions of the frequencies along the frequency axis. Finally we may define the *phase delay* as a quantity in samples

$$G(w) = -\frac{\arg\{Y(e^{iw})\}}{w}.$$

C.2.1 Allpass Filters

An allpass filter is one in which the gain is unity for all frequencies. That is, the filter lets all frequencies pass through. Such a filter will, however, possess a non-linear phase response. A first order allpass filter has transfer function

$$A(z) = \frac{a + z^{-1}}{1 + az^{-1}}.$$

It is easy to check that this filter has unit magnitude

$$\begin{aligned} |H(e^{iw})|^2 &= H(e^{iw})H(e^{-iw}) \\ &= \frac{a+e^{iw}}{1+ae^{iw}}\frac{a+e^{-iw}}{1+ae^{-iw}} \\ &= \frac{1+a^2}{1+a^2} \\ &= 1. \end{aligned}$$

The phase response may be expressed as

$$\arg\{H(e^{iw})\} = -w + 2\tan^{-1}\left(\frac{a\sin(w)}{1+a\cos(w)}\right).$$

Note that a single unit of delay, expressed as $H(z) = z^{-1}$ will have a phase response $\arg\{H(e^{iw})\} = -w$ so that the allpass filter represents one unit of delay plus some amount which is some non-linear function of frequency.

C.2.2 Fractional Delay Approximation

It is often useful to be able to measure the value of a signal between sample values and consequently we find the need to delay a signal by less than one unit. This is often termed *interpolation*. Ideally we should seek a filter with the required fractional phase delay and with unit magnitude. However this is unfortunately not possible. Nonetheless, there exist filters which approximate fractional delay, but with some trade-offs. The filters presented here are described well and analysed in depth in [24] and [51].

Using FIR Filters

Firstly we consider some FIR interpolators. These can be shown to provide good fractional delay, but exhibit a low-pass nature in the magnitude response. The simplest of these filters is the 1st order Lagrange Interpolator described by the transfer function

$$H(z) = 1 - d + dz^{-1},$$

where d is the value of the fractional delay required. Shown in Figure C-1 are the magnitude response and phase delay of the filter. They clearly show that the required delay is well represented over low frequencies, but the lowpass nature of the magnitude response is quite clear. The results can be improved by using higher order filters and the interested reader is pointed towards [24] and [51].

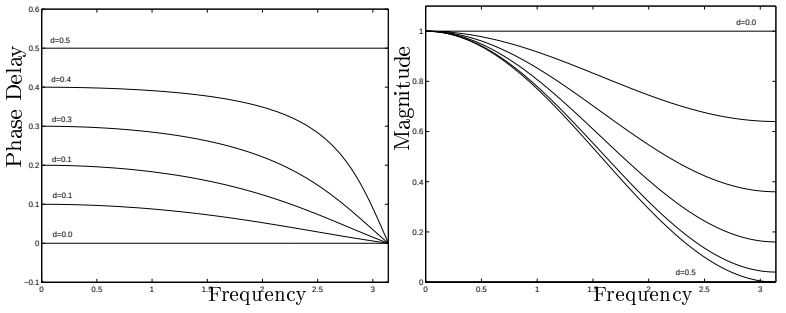

Figure C-1: *Magnitude Response and Phase Delay of 1st Order Lagrange Interpolator.*

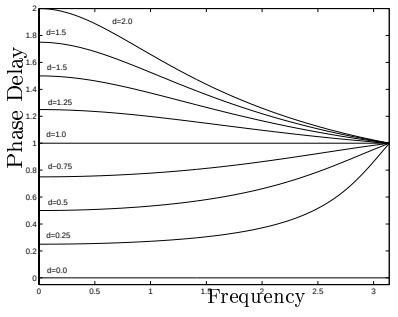

Figure C-2: *Phase Delay of 1st Order Thiran Allpass Filter.*

Using Allpass Filters

In order to achieve fractional delay, with a flat magnitude response, it is suggested to use allpass filters. The 1st order Thiran allpass filter has a filter coefficient set to

$$a = \frac{1-d}{1+d},$$

where d is the desired fractional delay. The phase delay of such a filter is shown in Figure C-2 for various values of d. We note that the delay is exactly as required at zero frequency, and that the filter is most accurate at other frequencies for values of delay close to $d = 1$. In fact it has been shown in [51] that ideal useful range of this filter is for delays in the region $d \in [0.5, 1.5]$. Better performance is achieved using higher order allpass filters, and again the interested reader is pointed towards [24] and [51].

Appendix D

Additional Proofs

D.1 Equivalence Between Waveguide Stiff String Model and a FDS

In this section we show how to compute the equivalence between the waveguide stiff string model described in section 5.3 and a FDS for the stiff string equation. Referring

to Figure 5-9 we begin with the scattering junction equation for a velocity junction.

$$
\begin{aligned}
V_j(n+1) &= \frac{2}{Y_J}\Big[Y_E V^+_{j,0}(n+1) + Y_E V^+_{j,1}(n+1) + Y_E V^+_{j,2}(n+1) + Y_E V^+_{j,3}(n+1) \\
&\qquad + Y_F V^+_{j,4}(n+1) + Y_F V^+_{j,5}(n+1)\Big] \\
&= \frac{2}{Y_J}\Big[Y_E \tilde{V}^-_{j-1,1}(n+\tfrac{1}{2}) + Y_E \tilde{V}^-_{j+1,0}(n+\tfrac{1}{2}) - Y_E \tilde{V}^-_{j,2}(n+\tfrac{1}{2}) - Y_E \tilde{V}^-_{j,3}(n+\tfrac{1}{2}) \\
&\qquad + Y_F V^-_{j-1,5}(n) + Y_F V^-_{j+1,4}(n)\Big] \\
&= \frac{2}{Y_J}\Big[-M^-_{j-1,1}(n+\tfrac{1}{2}) - M^-_{j+1,0}(n+\tfrac{1}{2}) + M^-_{j,2}(n+\tfrac{1}{2}) + M^-_{j,3}(n+\tfrac{1}{2})\Big] \\
&\qquad + \frac{2Y_F}{Y_J}\Big[V_{j-1}(n) + V_{j+1}(n)\Big] - \frac{2Y_F}{Y_J}\Big[V^+_{j-1,5}(n) + V^+_{j+1,4}(n)\Big] \\
&= \frac{2}{Y_J}\Big[-M_{j-1}(n+\tfrac{1}{2}) - M_{j+1}(n+\tfrac{1}{2}) + 2M_j(n+\tfrac{1}{2})\Big] \\
&\quad -\frac{2}{Y_J}\Big[-M^+_{j-1,1}(n+\tfrac{1}{2}) - M^+_{j+1,0}(n+\tfrac{1}{2}) + M^+_{j,2}(n+\tfrac{1}{2}) + M^+_{j,3}(n+\tfrac{1}{2})\Big] \\
&\qquad + \frac{2Y_F}{Y_J}\Big[V_{j-1}(n) + V_{j+1}(n)\Big] - \frac{2Y_F}{Y_J}\Big[V^-_{j,4}(n-1) + V^-_{j,5}(n-1)\Big] \\
&= \frac{2}{Y_J}\Big[-M_{j-1}(n+\tfrac{1}{2}) - M_{j+1}(n+\tfrac{1}{2}) + 2M_j(n+\tfrac{1}{2})\Big] \\
&\quad -\frac{2}{Y_J}\Big[-Y_E \tilde{V}^+_{j-1,1}(n+\tfrac{1}{2}) - Y_E \tilde{V}^+_{j+1,0}(n+\tfrac{1}{2}) + Y_E \tilde{V}^+_{j,2}(n+\tfrac{1}{2}) + Y_E \tilde{V}^+_{j,3}(n+\tfrac{1}{2})\Big] \\
&\qquad + \frac{2Y_F}{Y_J}\Big[V_{j-1}(n) + V_{j+1}(n)\Big] - \frac{2Y_F}{Y_J}\Big[V^-_{j,4}(n-1) + V^-_{j,5}(n-1)\Big] \\
&= \frac{2}{Y_J}\Big[-M_{j-1}(n+\tfrac{1}{2}) - M_{j+1}(n+\tfrac{1}{2}) + 2M_j(n+\tfrac{1}{2})\Big] \\
&\quad -\frac{2}{Y_J}\Big[-Y_E V^-_{j,0}(n) - Y_E V^-_{j,1}(n) - Y_E V^-_{j,2}(n) + Y_E V^-_{j,3}(n)\Big] \\
&\qquad + \frac{2Y_F}{Y_J}\Big[V_{j-1}(n) + V_{j+1}(n)\Big] - \frac{2Y_F}{Y_J}\Big[V^-_{j,4}(n-1) + V^-_{j,5}(n-1)\Big] \qquad \text{(D.1)}
\end{aligned}
$$

Now we may write

$$
\begin{aligned}
\frac{2Y_E}{Y_J}\Big[V^-_{j,0}(n) + V^-_{j,1}(n) + V^-_{j,2}(n) + V^-_{j,3}(n)\Big] &= \frac{2Y_E}{Y_J}\big[4V_j(n)\big] \\
&\quad - \frac{2Y_E}{Y_J}\Big[V^+_{j,0}(n) + V^+_{j,1}(n) + V^+_{j,2}(n) + V^+_{j,3}(n)\Big]
\end{aligned}
$$

and we may also say that

$$\begin{aligned}
&\frac{2Y_E}{Y_J}\Big[V^+_{j,0}(n+1)+V^+_{j,1}(n+1)+V^+_{j,2}(n+1)+V^+_{j,3}(n+1)\Big]\\
&\quad=\frac{2}{Y_J}\Big[-M_{j-1}(n+\frac{1}{2})-M_{j+1}(n+\frac{1}{2})+2M_j(n+\frac{1}{2})\Big]\\
&\quad+\frac{2Y_E}{Y_J}\Big[V^-_{j,0}(n)+V^-_{j,1}(n)+V^-_{j,2}(n)+V^-_{j,3}(n)\Big]
\end{aligned}$$

so that

$$\begin{aligned}
&\frac{2Y_E}{Y_J}\Big[V^+_{j,0}(n)+V^+_{j,1}(n)+V^+_{j,2}(n)+V^+_{j,3}(n)\Big]\\
&\quad=\frac{2}{Y_J}\Big[-M_{j-1}(n-\frac{1}{2})-M_{j+1}(n-\frac{1}{2})+2M_j(n-\frac{1}{2})\Big]\\
&\quad+\frac{2Y_E}{Y_J}\Big[V^-_{j,0}(n-1)+V^-_{j,1}(n-1)+V^-_{j,2}(n-1)+V^-_{j,3}(n-1)\Big].
\end{aligned}$$

Consequently equation (D.1) can be rewritten as

$$\begin{aligned}
V_j(n+1)&=\frac{2}{Y_J}\Big[-M_{j-1}(n+\frac{1}{2})-M_{j+1}(n+\frac{1}{2})+2M_j(n+\frac{1}{2})\Big]\\
&\qquad+\frac{2Y_E}{Y_J}\big[4V_j(n)\big]-\frac{2Y_E}{Y_J}\Big[V^+_{j,0}(n)+V^+_{j,1}(n)+V^+_{j,2}(n)+V^+_{j,3}(n)\Big]\\
&\qquad+\frac{2Y_F}{Y_J}\Big[V_{j-1}(n)+V_{j+1}(n)\Big]-\frac{2Y_F}{Y_J}\Big[V^-_{j,4}(n-1)+V^-_{j,5}(n-1)\Big]\\
&=\frac{2}{Y_J}\Big[-M_{j-1}(n+\frac{1}{2})-M_{j+1}(n+\frac{1}{2})+2M_j(n+\frac{1}{2})\Big]+\frac{2Y_E}{Y_J}\big[4V_j(n)\big]\\
&\qquad-\frac{2}{Y_J}\Big[-M_{j-1}(n-\frac{1}{2})-M_{j+1}(n-\frac{1}{2})+2M_j(n-\frac{1}{2})\Big]\\
&\qquad-\frac{2Y_E}{Y_J}\Big[V^-_{j,0}(n-1)+V^-_{j,1}(n-1)+V^-_{j,2}(n-1)+V^-_{j,3}(n-1)\Big]\\
&\qquad+\frac{2Y_F}{Y_J}\Big[V_{j-1}(n)+V_{j+1}(n)\Big]-\frac{2Y_F}{Y_J}\Big[V^-_{j,4}(n-1)+V^-_{j,5}(n-1)\Big]\\
&=-\frac{2}{Y_J}\Big[M_{j-1}(n+\frac{1}{2})-2M_j(n+\frac{1}{2})+M_{j+1}(n+\frac{1}{2})\Big]\\
&\qquad+\frac{2}{Y_J}\Big[M_{j-1}(n-\frac{1}{2})-2M_j(n-\frac{1}{2})+M_{j+1}(n-\frac{1}{2})\Big]\\
&\qquad+\frac{2Y_E}{Y_J}\big[4V_j(n)\big]+\frac{2Y_F}{Y_J}\Big[V_{j-1}(n)+V_{j+1}(n)\Big]-V_j(n-1).
\end{aligned}\tag{D.2}$$

Now from equation (5.13) we know that

$$M_j(n+\frac{1}{2}) - M_j(n-\frac{1}{2}) = \frac{1}{2Z}\Big[V_{i+1}(n) - 2V_i(n) + V_{i-1}(n)\Big],$$

so that

$$M_{j-1}(n+\frac{1}{2}) - M_{j-1}(n-\frac{1}{2}) = \frac{1}{2Z}\Big[V_i(n) - 2V_{i-1}(n) + V_{i-2}(n)\Big]$$
$$M_{j+1}(n+\frac{1}{2}) - M_{j+1}(n-\frac{1}{2}) = \frac{1}{2Z}\Big[V_{i+2}(n) - 2V_{i+1}(n) + V_i(n)\Big].$$

Hence equation (D.2) can be rearranged as

$$V_j(n+1) + V_j(n-1) = -\frac{1}{2Z}\frac{2}{Y_J}\Big[V_{j+2}(n) - 4V_{j+1}(n) + V_j(n) - 4V_{j-1}(n) + V_{j-2}(n)\Big] + \frac{2Y_E}{Y_J}\big[4V_j(n)\big] + \frac{2Y_F}{Y_J}\Big[V_{j-1}(n) + V_{j+1}(n)\Big].$$

Now subtracting $2V_J(n)$ from either side gives

$$\begin{aligned} V_j(n+1) - 2V_j(n) + V_j(n-1) = \\ -\frac{1}{2Z}\frac{2}{Y_J}\Big[V_{j+2}(n) - 4V_{j+1}(n) + V_j(n) - 4V_{j-1}(n) + V_{j-2}(n)\Big] \\ + \frac{2Y_E}{Y_J}\Big[4V_j(n)\Big] + \frac{2Y_F}{Y_J}\Big[V_{j-1}(n) + V_{j+1}(n)\Big] - \frac{2}{Y_J}(4Y_E + 2Y_F)V_j(n). \end{aligned}$$

Now rearranging yields the following FDS.

$$\begin{aligned} V_j(n+1) - 2V_j(n) + V_j(n-1) = \\ -\frac{Y_E}{Y_J}\Big[V_{j+2}(n) - 4V_{j+1}(n) + V_j(n) - 4V_{j-1}(n) + V_{j-2}(n)\Big] \\ + \frac{2Y_F}{Y_J}\Big[V_{j-1}(n) - 2V_j(n) + V_{j+1}(n)\Big]. \end{aligned}$$

This scheme is of the form of the required FDS for the stiff string equation and impedance parameters are matched using the relationships described in section 5.3.2.

D.2 Equivalence Between Waveguide Stiff Membrane Model and a FDS

In a similar procedure to the one of the previous section we now derive the equivalence between the waveguide stiff membrane model of section 6.2 and a corresponding FDS for the stiff membrane equation (6.14). The calculation proceeds in a similar manner to that of equation (6.8) where this time each velocity junction has ports connecting waveguides of either plate impedance Y_E or membrane impedance Y_F. Beginning with a velocity junction.

$$
\begin{aligned}
V_{i,j}(n+1) &= \frac{2}{Y_J}\Big[\sum_{k=0}^{7} Y_E V^+_{i,j,k}(n+1) + \sum_{k=8}^{11} Y_F V^+_{i,j,k}(n+1)\Big] \\
&= \frac{2}{Y_J}\Big[Y_E \tilde{V}^-_{i+1,j,2}(n+\tfrac{1}{2}) + Y_E \tilde{V}^-_{i,j+1,3}(n+\tfrac{1}{2}) + Y_E \tilde{V}^-_{i-1,j,0}(n+\tfrac{1}{2}) + Y_E \tilde{V}^-_{i,j-1,1}(n+\tfrac{1}{2}) \\
&\quad - \sum_{k=4}^{7} Y_E \tilde{V}^-_{i,j,k}(n+\tfrac{1}{2}) + Y_F V^-_{i+1,j,10}(n) + Y_F V^-_{i,j+1,11}(n) + Y_F V^-_{i-1,j,8}(n) + Y_F V^-_{i,j-1,9}(n)\Big] \\
&= \frac{2}{Y_J}\Big[- M^-_{i+1,j,2}(n+\tfrac{1}{2}) - M^-_{i,j+1,3}(n+\tfrac{1}{2}) - M^-_{i-1,j,0}(n+\tfrac{1}{2}) - M^-_{i,j-1,2}(n+\tfrac{1}{2}) \\
&\quad + \sum_{k=4}^{7} M^-_{i,j,k}(n+\tfrac{1}{2})\Big] + \frac{2Y_F}{Y_J}\Big[V_{i+1,j}(n) + V_{i,j+1}(n) + V_{i-1,j}(n) + V_{i,j-1}(n)\Big] \\
&\quad - \frac{2Y_F}{Y_J}\Big[V^+_{i+1,j,10}(n) + V^+_{i,j+1,11}(n) + V^+_{i-1,j,8}(n) + V^+_{i,j-1,9}(n)\Big] \\
&= \frac{2}{Y_J}\Big[- M_{i+1,j}(n+\tfrac{1}{2}) - M_{i,j+1}(n+\tfrac{1}{2}) - M_{i-1,j}(n+\tfrac{1}{2}) - M_{i,j-1}(n+\tfrac{1}{2}) + 4M_{i,j}(n+\tfrac{1}{2})\Big] \\
&\quad - \frac{2}{Y_J}\Big[- M^+_{i+1,j,2}(n+\tfrac{1}{2}) - M^+_{i,j+1,3}(n+\tfrac{1}{2}) - M^+_{i-1,j,0}(n+\tfrac{1}{2}) - M^+_{i,j-1,2}(n+\tfrac{1}{2}) \\
&\quad + \sum_{k=4}^{7} M^+_{i,j,k}(n+\tfrac{1}{2})\Big] + \frac{2Y_F}{Y_J}\Big[V_{i+1,j}(n) + V_{i,j+1}(n) + V_{i-1,j}(n) + V_{i,j-1}(n)\Big] \\
&\quad - \frac{2Y_F}{Y_J}\Big[V^-_{i,j,8}(n-1) + V^-_{i,j,9}(n-1) + V^-_{i,j,10}(n-1) + V^-_{i,j,11}(n-1)\Big] \\
&= \frac{2}{Y_J}\Big[- M_{i+1,j}(n+\tfrac{1}{2}) - M_{i,j+1}(n+\tfrac{1}{2}) - M_{i-1,j}(n+\tfrac{1}{2}) - M_{i,j-1}(n+\tfrac{1}{2}) + 4M_{i,j}(n+\tfrac{1}{2})\Big] \\
&\quad - \frac{2}{Y_J}\Big[- \sum_{k=0}^{7} Y_E V^-_{i,j,k}(n)\Big] + \frac{2Y_F}{Y_J}\Big[V_{i+1,j}(n) + V_{i,j+1}(n) + V_{i-1,j}(n) + V_{i,j-1}(n)\Big] \\
&\quad - \frac{2}{Y_J}\Big[\sum_{k=8}^{11} Y_F V^-_{i,j,k}(n-1)\Big].
\end{aligned}
\tag{D.3}
$$

Now, similarly to the 1D case we note the standard fact that

$$\frac{2Y_E}{Y_J}\left[\sum_{k=0}^{7} V^-_{i,j,k}(n)\right] = \frac{2Y_E}{Y_J}\left[8V_{i,j}(n)\right] - \frac{2Y_E}{Y_J}\left[\sum_{k=0}^{7} V^+_{i,j,k}(n)\right],$$

and that

$$\begin{aligned}
&\frac{2Y_E}{Y_J}\left[\sum_{k=0}^{7} V^+_{i,j,k}(n)\right] \\
&= -\frac{2}{Y_J}\left[M_{i+1,j}(n-\frac{1}{2}) + M_{i,j+1}(n-\frac{1}{2}) + M_{i-1,j}(n-\frac{1}{2}) + M_{i,j-1}(n-\frac{1}{2}) - 4M_{i,j}(n-\frac{1}{2})\right] \\
&\quad + \frac{2Y_E}{Y_J}\left[\sum_{k=0}^{7} V^-_{i,j,k}(n-1)\right].
\end{aligned}$$

Now these two identities help us re-write the last line of equation (D.3) to give

$$\begin{aligned}
&V_{i,j}(n+1) = \\
&\quad -\frac{2}{Y_J}\left[M_{i+1,j}(n+\frac{1}{2}) + M_{i,j+1}(n+\frac{1}{2}) + M_{i-1,j}(n+\frac{1}{2}) + M_{i,j-1}(n+\frac{1}{2}) - 4M_{i,j}(n+\frac{1}{2})\right] \\
&\quad + \frac{2}{Y_J}\left[M_{i+1,j}(n-\frac{1}{2}) + M_{i,j+1}(n-\frac{1}{2}) + M_{i-1,j}(n-\frac{1}{2}) + M_{i,j-1}(n-\frac{1}{2}) - 4M_{i,j}(n-\frac{1}{2})\right] \\
&\quad - \frac{2Y_E}{Y_J}\left[\sum_{k=0}^{7} V^-_{i,j,k}(n-1)\right] - \frac{2Y_E}{Y_J}\left[\sum_{k=8}^{11} V^-_{i,j,k}(n-1)\right] + \frac{2Y_E}{Y_J}\left[8V_{i,j}(n)\right] \\
&\quad + \frac{2Y_F}{Y_J}\left[V_{i+1,j}(n) + V_{i,j+1}(n) + V_{i-1,j}(n) + V_{i,j-1}(n)\right] \\
&= \frac{2}{Y_J}\left[-M_{i+1,j}(n+\frac{1}{2}) - M_{i,j+1}(n+\frac{1}{2}) - M_{i-1,j}(n+\frac{1}{2}) - M_{i,j-1}(n+\frac{1}{2}) + 4M_{i,j}(n+\frac{1}{2})\right] \\
&\quad + \frac{2}{Y_J}\left[M_{i+1,j}(n-\frac{1}{2}) + M_{i,j+1}(n-\frac{1}{2}) + M_{i-1,j}(n-\frac{1}{2}) + M_{i,j-1}(n-\frac{1}{2}) - 4M_{i,j}(n-\frac{1}{2})\right] \\
&\quad + \frac{2Y_E}{Y_J}\left[8V_{i,j}(n)\right] + \frac{2Y_F}{Y_J}\left[V_{i+1,j}(n) + V_{i,j+1}(n) + V_{i-1,j}(n) + V_{i,j-1}(n)\right] - V_{i,j}(n). \qquad \text{(D.4)}
\end{aligned}$$

Now in analogy to the 1D case, we may use equation (6.10) which asserts information about the force junctions on the waveguide plate model, to give

$$
\begin{aligned}
M_{i,j}(n+\frac{1}{2}) - M_{i,j}(n-\frac{1}{2}) &= \frac{2}{Z_J}\Big[V_{i+1,j}(n) + V_{i,j+1}(n) + V_{i-1,j}(n) + V_{i,j-1}(n) + 4V_{i,j}(n)\Big] \\
M_{i+1,j}(n+\frac{1}{2}) - M_{i+1,j}(n-\frac{1}{2}) &= \frac{2}{Z_J}\Big[V_{i+2,j}(n) + V_{i+1,j+1}(n) + V_{i,j}(n) + V_{i+1,j-1}(n) + 4V_{i+1,j}(n)\Big] \\
M_{i,j-1}(n+\frac{1}{2}) - M_{i,j-1}(n-\frac{1}{2}) &= \frac{2}{Z_J}\Big[V_{i+1,j+1}(n) + V_{i,j+2}(n) + V_{i-1,j+1}(n) + V_{i,j}(n) + 4V_{i,j+1}(n)\Big] \\
M_{i-1,j}(n+\frac{1}{2}) - M_{i-1,j}(n-\frac{1}{2}) &= \frac{2}{Z_J}\Big[V_{i,j}(n) + V_{i-1,j+1}(n) + V_{i-2,j}(n) + V_{i-1,j-1}(n) + 4V_{i-1,j}(n)\Big] \\
M_{i,j-1}(n+\frac{1}{2}) - M_{i,j-1}(n-\frac{1}{2}) &= \frac{2}{Z_J}\Big[V_{i+1,j-1}(n) + V_{i,j}(n) + V_{i-1,j-1}(n) + V_{i,j-2}(n) + 4V_{i,j-1}(n)\Big].
\end{aligned}
$$

Using these identities we may rewrite equation (D.4) as

$$
\begin{aligned}
V_{i,j}(n+1) = -\frac{2}{Y_J}\frac{2}{Z_J}\Big[&V_{i+2,j}(n) + V_{i,j+2}(n) + V_{i-2,j}(n) + V_{i,j-2}(n) \\
&-8V_{i+1,j}(n) - 8V_{i,j+1}(n) - 8V_{i-1,j}(n) - 8V_{i,j-1}(n) \\
&+2V_{i+1,j+1}(n) + 2V_{i-1,j+1}(n) + 2V_{i-1,j-1}(n) + 2V_{i+1,j-1}(n) + 20V_{i,j}(n)\Big] \\
&+\frac{2Y_E}{Y_J}\big[8V_{i,j}(n)\big] + \frac{2Y_F}{Y_J}\Big[V_{i+1,j}(n) + V_{i,j+1}(n) + V_{i-1,j}(n) + V_{i,j-1}(n)\Big] - V_{i,j}(n).
\end{aligned}
$$

Now, subtracting $2V_{i,j}(n)$ from either side leaves us with the required FDS and writing $Z_J = \frac{8}{Y_E}$

$$
\begin{aligned}
V_{i,j}(n+1) - 2V_{i,j}(n) + V_{i,j}(n-1) = -\frac{Y_E}{2Y_J}\Big[&V_{i+2,j}(n) + V_{i,j+2}(n) + V_{i-2,j}(n) + V_{i,j-2}(n) \\
&- 8V_{i+1,j}(n) - 8V_{i,j+1}(n) - 8V_{i-1,j}(n) - 8V_{i,j-1}(n) \\
&+ 2V_{i+1,j+1}(n) + 2V_{i-1,j+1}(n) + 2V_{i-1,j-1}(n) + 2V_{i+1,j-1}(n) + 20V_{i,j}(n)\Big] \\
&+ \frac{2Y_F}{Y_J}\Big[V_{i+1,j}(n) - 2V_{i,j}(n) + V_{i-1,j}(n) + V_{i,j+1}(n) - 2V_{i,j}(n) + V_{i,j-1}(n)\Big].
\end{aligned}
$$

This scheme is equivalent to the FDS of equation (6.14) when applying the equivalence identities of section 6.2.2.

Bibliography

[1] M. Aird and J. Laird. Extending digital waveguides to include material modelling. In *Proc. of the COST G-6 Workshop on Digital Audio Effects (DAFX-01)*, pages 138–142. Univesity Of Limerick, Department of Computer Science and Information Systems, December 2001.

[2] M. Aird and J. Laird. Towards material modelling in physical models using digital waveguides. In *Proc. Music Without Walls? Music Without Instruments?* DeMontfort University, 2001. Published on CDRom.

[3] M. Aird, J. Laird, and J. Fitch. Modelling a drum by interfacing 2-d and 3-d waveguide meshes. In *Proc. International Computer Music Conference*, pages 82–85. ICMA, August 2000.

[4] Marc Aird. Correcting and manipulating the dispersion characteristics in a waveguide mesh towards physical models of musical instruments. Technical report, University of Bath, 2000. `http://www.cs.bath.ac.uk/~mapma/`.

[5] Marc Aird. Towards material modelling in physical models. Technical report, University of Bath, 2001. `http://www.cs.bath.ac.uk/~mapma/`.

[6] Balazs Bank. Physics-based sound synthesis of the piano. Master's thesis, Helsinki University of Technology, 2000. `http://www.acoustics.hut.fi/~bbank/`.

[7] Stefan Bilbao. Digital waveguide networks for inhomogeneous materials. In *Proc. of the COST G-6 Workshop on Digital Audio Effects (DAFX-00)*, pages 249–253. University of Verona, Dipartimento Scientifico e Tecnologico, December 2000.

[8] Stefan Bilbao. *Wave and Scattering Methods for the Numerical Integration of Partial Differential Equations.* PhD thesis, Stanford University, March 2001. `http://www-ccrma.stanford.edu/~bilbao/`.

[9] I. Bork, A. Chaigne, L-C. Trebuchet, M. Kosfelder, and D. Pillot. Comparison between modal analysis and finite element modeling of a marimba bar. *Acustica - Acta Acustica*, 85:258–266, 1999.

[10] Antoine Chaigne and Anders Askenfelt. Numerical simulations of piano strings. i. a physical model for a struck string using finite difference methods. *J. Acoust. Soc. Am.*, 95(2):1112–1118, 1994.

[11] Antoine Chaigne and Vincent Doutaut. Numerical simulations of xylophones. i. time-domain modeling of the vibrating bars. *J. Acoust. Soc. Am.*, 101(1):539–557, 1997.

[12] Christos Christopoulos. *The Transmission-Line Modeling Method TLM.* IEEE Press, 1995.

[13] Pirouz Djoharian. Material design in physical modeling sound synthesis. In *Proc. of the COST G-6 Workshop on Digital Audio Effects (DAFX-99)*, pages 131–134. Norwegian University of Science and Technology, Department of Telecommunication, December 1999.

[14] Pirouz Djoharian. Shape and material design in physical modeling sound synthesis. In *Proc. International Computer Music Conference.* ICMA, August 2000.

[15] N. H. Fletcher and T. D. Rossing. *The Physics Of Musical Instruments.* Springer-Verlag, New York, 1991.

[16] F. Fontana and D. Rocchesso. Physical modeling of membranes for percussion instruments. *Acustica – Acta Acustica*, 84:529–542, 1998.

[17] F. Fontana and D. Rocchesso. Online correction of dispersion error in 2d waveguide meshes. In *Proc. International Computer Music Conference*, pages 78–81. ICMA, August 2000.

[18] F. Fontana and D. Rocchesso. Using the waveguide mesh in modeling 3d resonators. In *Proc. of the COST G-6 Workshop on Digital Audio Effects (DAFX-00)*, pages 239–232. University of Verona, Dipartimento Scientifico e Tecnologico, December 2000.

[19] F. Fontana and D. Rocchesso. Signal-theoretic characterisation of waveguide mesh geometries for models of two-dimensional wave propogation in elastic media. *IEEE Trans. on Speech and Audio*, 9(1), Feb 2001.

[20] Karl F. Graff. *Wave Motion in Elastic Solids.* Clarendon Press, Oxford, 1975.

[21] D. E. Hall. *Basic Acoustics.* Harper and Row, New York, 1987.

[22] Francis B. Hildebrand. *Finite Difference Equations and Simulations.* Prentice-Hall, 1968.

[23] J. Jeans. *Science and Music.* Cambridge University Press, 1937.

[24] T.I. Laakso, V. Valamaki, M. Karjalainen, and U.K. Laine. Splitting the unit delay - tools for fractional delay filter design. *IEEE Signal Processing Magazine*, 13:30–58, January 1996.

[25] J. Laird, P. Masri, and N. Canagarajah. Efficient and accurate synthesis of circular membranes using digital waveguides. In *IEE Colloqium: Audio and Music Technology : The Challenge of Creative DSP*, Nov 1998.

[26] J. Laird, P. Masri, and N. Canagarajah. Modelling diffusion at the boundary of a digital waveguide mesh. In *Proc. International Computer Music Conference*, pages 492–495. ICMA, October 1999.

[27] Joel Laird. *The Physical Modelling of Musical Instruments Using Digital Waveguides (with emphasis on drum modelling).* PhD thesis, University of Bristol, October 2001.

[28] R.S. Lakes. *Viscoelastic Solids.* CRC Press, 1999.

[29] K.A. Legge and N.H. Fletcher. Nonlinear generation of missing modes on a vibrating string. *J. Acoust. Soc. Am*, 76(1):5–12, July 1984.

[30] Antoine Chaigne Leila Rhaouti and Patrick Joly. Time-domain modeling and numerical simulation of a kettledrum. *J. Acoust. Soc. Am.*, 105(6):3545–3562, 1999.

[31] R. Duncan Luce. *Sound and Hearing.* Lawrence Erlbaum Associates, Publishers, 1993.

[32] F.R. Moore. *Elements Of Computer Music.* Prentice-Hall, 1990.

[33] P.M. Morse and K.I. Ingard. *Theoretical Acoustics.* McGraw-Hill, 1968.

[34] K. W. Morton and D. F. Mayers. *Numerical Solution of Partial Differential Equations.* Cambridge University Press, 1994.

[35] Mark Newbold. Mark newbold's rhombic dodecahedron page. `http://dogfeathers.com/mark/rhdodec.html`.

[36] A.V. Oppenheim and R.W. Schafer. *Discrete-Time Signal Proceesing.* Prentice-Hall International, 1989.

[37] Andrea Paladin and Davide Rocchesso. A dispersive resonator in real time on mars workstation. In *Proc. International Computer Music Conference*, pages 146–149. ICMA, October 1992.

[38] H.F. Pollard. *Sound Waves in Solids.* Pion, 1977.

[39] Juan G. Roederer. *Introduction to the Physics and Psychophysics of Music.* Springer-Verlag New York, 1973.

[40] L. Savioja. Improving the three-dimensional digital waveguide mesh by interpolation. In *Proc. Nordic Acoustical Meeting (NAM 98)*, pages 265–268, Sept 1998.

[41] L. Savioja, T. Rinne, and T. Takala. Simulation of room acoustics with a 3-D finite difference mesh. In *Proc. International Computer Music Conference*, pages 463–466. ICMA, September 1994.

[42] L. Savioja and V. Valamaki. Improved discrete-time modeling of multi-dimensional wave propogation using the interpolated digital waveguide mesh. In *Proc. 1997 IEEE International Conference on Acoustics, Speech and Signal Processing (ICASSP'97)*, volume 1, pages 459–462, April 1997.

[43] L. Savioja and V. Valamaki. Reducing the dispersion error in the digital waveguide mesh using interpolation and frequency warping techniques. *IEEE Transactions on Speech and Audio Processing*, 8:184–194, March 1999.

[44] L. Savioja and V. Valamaki. Reduction of the dispersion error in the triangular waveguide mesh using frequency warping. *IEEE Signal Processing Letters*, 6(3):58–60, March 1999.

[45] Lauri Savioja. *Modeling Techniques For Virtual Acoustics.* PhD thesis, Helsinki University Of Technology, 1999.

[46] J. O. Smith. Physical modeling using digital waveguides. *Computer Music Journal*, 16(4):74–87, 1992.

[47] J.C. Strikwerda. *Finite Difference Schemes and Partial Differential Equations.* Wadsworth, 1989.

[48] Tero Tolonen. Model-based analysis and resynthesis of acoustic guitar tones. Master's thesis, Helsinki University of Technology, 1998. `http://www.acoustics.hut.fi/~ttolonen/research.html`.

[49] Tero Tolonen, Vesa Valamaki, and Matti Karjalainen. Modeling of tension modulation nonlinearity in plucked strings. *IEEE Transactions on Speech and Audio Processing*, 8(3):300–310, May 2000.

[50] Nicholas W. Tschoegl. *The Phenomenological Theory of Linear Viscoelastic Behaviour*. Springer-Verlag, 1989.

[51] V. Valamaki. *Discrete Time Modeling of Acoustic Tubes Using Fractional Delay Filters*. PhD thesis, Helsinki University Of Technology, 1995.

[52] S. A. Van Duyne and J. O. Smith. Physical modeling with the 2-d digital waveguide mesh. In *Proc. International Computer Music Conference*, pages 40–47. ICMA, 1993.

[53] S. A. Van Duyne and J. O. Smith. A simplified approach to modeling dispersion caused by stiffness in strings and plates. In *Proc. International Computer Music Conference*, pages 407–410. ICMA, September 1994.

[54] S. A. Van Duyne and J. O. Smith. Travelling wave implementation of a lossless mode-coupling filter and the wave digital hammer. In *Proc. International Computer Music Conference*, pages 411–418. ICMA, September 1994.

[55] S. A. Van Duyne and J. O. Smith. The tetrahedral digital waveguide mesh. In *Proc. IEEE Workshop on Applications of Signal Processing to Audio and Acoustics*, pages 1–4. IEEE Press, October 1995.

[56] S. A. Van Duyne and J. O. Smith. The 3-D tetrahedral digital waveguide mesh with musical applications. In *Proc. International Computer Music Conference*, pages 9–16. ICMA, August 1996.

[57] G.N. Watson. *Theory of Bessel Functions*. Cambridge University Press, 1952.